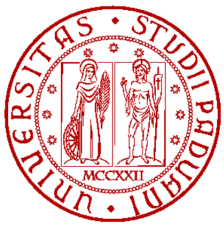

UNIVERSITÀ DEGLI STUDI DI PADOVA
Dipartimento di Fisica e Astronomia "Galileo Galilei"
Corso di Studi in Fisica

Tesi di Laurea Magistrale in Fisica

Characterization of a Silicon strip detector for radiotherapy use

Candidata: **Anna Selva**

Relatore Interno: **Prof. Silvia Monica Lenzi**
Relatore Esterno: **Prof. Maria Isabel Gallardo Fuentes**

Anno Accademico 2013/2014

A Davide,
passato, presente e futuro.
E a mamma e papà,
che hanno reso possibile
l'arrivare fin qui.

Acknowledgements

This work would not have been possible without the many people who gave their time, energies, and enthusiasm for helping me during these months. First of all, I wish to thank my supervisor during my internship in Seville, Prof. Maria Isabel Gallardo Fuentes, who spent much of her time to explain to me even the basics and whose helpfulness in discussing and resolving all doubts that came to light was invaluable. I surely own her the majority of the knowledge and skills acquired during this work.

I also wish to thank my supervisor at the University of Padova, Prof. Silvia Monica Lenzi, not only for giving me the opportunity to go to Seville, but also for her practical help and total availability during and after my stay there. She never failed to provide support in many matters, not only concerning this work.

Among the RADIA collaboration, a special thanks goes to Miguel Antonio Cortés-Giraldo, who gave lots of his time in teaching me GEANT4 and many features of C++, providing a basic application model on which I worked and answering all sorts of basic questions with great patience, until in the end I was able to put it all to use. Moreover, I would like to thank him for proof-reading a great part of this work.

A huge thank you goes also to Maria del Carmen Ovejero Mayoral, not only for helping me understand many working features of the experimental setup and data analysis software, but also for all the laughing, the chatting, the lunches and the trips, and for basically sharing with me all the goods and the bads concerning this project.

I would also like to thank all the members of the RADIA collaboration for their help and support, each one with their specific contribution and field of expertise. In particular, I would like to thank Rafael Arráns, for his availability and helpfulness during measurements and in answering questions on clinical procedures and equipment, and for providing the hospital quality assurance data for the validation of the system response; José Manuel Espino, for the supervision during measurements and helpful discussion; and Alfredo Pérez Vega-Leal for his kind explanations on the working principles of the electronic chain and the associated uncertainties. Moreover, I would like to thank José Manuel Quesada Molina, also a member of the RADIA collaboration, for his practical help with software installation and Spanish bureaucracy.

UNIVERSITY OF PADOVA
Course of Study in Physics

Tesi di Laurea Magistrale

Characterization of a Silicon strip detector for radiotherapy use

Presented by **Anna Selva**

Internal Supervisor: **Prof. Silvia Monica Lenzi**
External Supervisor: **Prof. Maria Isabel Gallardo Fuentes**

Abstract

The present work aims at the first characterization of a silicon strip detector to be used for quality assurance of intensity-modulated radiotherapy (IMRT) treatments. After a first feasibility study, a new prototype has been designed and built in the framework of a collaboration between the University of Seville, the National Accelerator Centre (CNA – Centro Nacional de Aceleradores, Seville, Spain), the Virgen Macarena University Hospital and the private company Micron Semiconductor Ltd. It is composed of two single-sided silicon strip detectors, mounted in a back-to-back configuration with the strips arranged along two orthogonal directions, and separated by a Kapton layer. This detecting unit can be housed in two different phantoms, a slab and a cylindrical one: in the former, the detector is placed orthogonally to the beam axis, in the latter, it is placed vertically, with the aim of obtaining on-line, measurement-based dose maps in the axial plane of a hypothetical patient.

This work discusses the first characterization of the new detecting unit, housed in the slab phantom and irradiated with a clinical linear accelerator in the 6 MV photon mode. Linearity, reproducibility, minimum dose threshold and leakage current have been analysed; a Geant4 simulation of the dosimetry system has also been carried out to gain further insight on the physical processes at play. The detector has then been calibrated and used to reproduce routine quality assurance hospital measurements; the comparison between the two shows remarkable agreement.

The work herein described has been carried out during an internship at the University of Seville, under the supervision of Prof. Maria Isabel Gallardo Fuentes, in the framework of the LLP – Erasmus Student Mobility for Placement programme.

Contents

1 Introduction **3**
- 1.1 Cancer and its treatment . . . 3
  - 1.1.1 Radiotherapy techniques . . . 4
  - 1.1.2 Structure of a clinical linac . . . 5
  - 1.1.3 Treatment planning and verification methods . . . 7
- 1.2 Aims of this work . . . 8

2 Dosimetry: principles and techniques **11**
- 2.1 Dose deposition . . . 11
  - 2.1.1 Interaction of radiation with matter . . . 12
  - 2.1.2 Dosimetric magnitudes . . . 12
  - 2.1.3 KERMA, dose and electronic equilibrium . . . 14
- 2.2 Dose measurement: cavity theory . . . 16
  - 2.2.1 Small cavities: Bragg-Gray and Spencer-Attix cavity theory . . . 17
  - 2.2.2 Big cavities: CPE cavity theory . . . 18
  - 2.2.3 Intermediate cavities: Burlin cavity theory . . . 19
- 2.3 Dose measurement: dosimeters . . . 20
  - 2.3.1 Ionization chambers . . . 20
  - 2.3.2 Semiconductor detectors . . . 21
  - 2.3.3 Film dosimetry . . . 23
  - 2.3.4 Luminescence dosimeters . . . 23
  - 2.3.5 Other kinds of dosimeters . . . 24
- 2.4 Treatment verification detectors . . . 25
  - 2.4.1 Commercial 2D arrays . . . 26
  - 2.4.2 Silicon monolithic detectors . . . 27
  - 2.4.3 Detectors with cylindrical geometry . . . 28

3 Materials and methods **30**
- 3.1 Detection system . . . 30
  - 3.1.1 The detector . . . 31
  - 3.1.2 The phantoms . . . 32
  - 3.1.3 Electronics and Data Acquisition System . . . 33
  - 3.1.4 Measurements . . . 34
- 3.2 Monte Carlo simulations . . . 35
  - 3.2.1 Characteristics of the simulated setup . . . 36

3.2.2 Analysis for different configurations 36

4 Results **39**
4.1 Characterization of the response 39
4.1.1 Linearity 41
4.1.2 Reproducibility 44
4.1.3 Minimum dose threshold 44
4.1.4 Leakage current 47
4.1.5 Noise 49
4.1.6 Uncertainty estimation 50
4.2 GEANT4 analysis 52
4.2.1 Dose deposition in two central "cavities" 53
4.2.2 Dose deposition in each strip 55
4.3 Calibration 55
4.3.1 Calibration in uniformity conditions 57
4.3.2 Calibration in standard conditions 59
4.4 Comparison with clinical measurements 61
4.4.1 Percent depth dose curve 61
4.4.2 Penumbra 63
4.4.3 Output Factor measurements 66

5 Conclusions and future perspectives **68**

Chapter 1

Introduction

In this introductory chapter a brief discussion on cancer and its treatment modalities is presented, focusing particularly on the various radiotherapy techniques that have been developed to achieve higher dose conformity, better tumour control and increased sparing of normal tissue. The working principles on which a medical linear accelerator is based are also explained. Then, the aims of the RADIA project are described, detailing the ones that are relevant for the present work.

The main references for this chapter are oncology textbooks such as [1] and [2], and review articles on the topic, especially [3].

1.1 Cancer and its treatment

Cancer is characterized by an abnormal growth of cells in the body, which reduces the functionality of the affected tissue and, in the worst case, may lead to the death of the patient. It is better defined by four characteristics which set cancerous tissue apart from normal one: clonality, autonomy, anaplasia and metastasis [1]. Clonality refers to the fact that cancer originates from a single mutating cell, which produces clones through replication of its altered DNA, increasing the tumorous mass. Autonomy alludes to the fact that these cells are not regulated by normal biophysical and biochemical control mechanisms of the body, and are often able to proliferate even in unfavourable conditions. Anaplasia means that they lose their differentiation and specific functionality. Finally, metastasis refers to their ability to leave their original fixed position in the tissue, invade blood vessels and spread to other parts of the organism, which may be quite far from their originating site.

Cancer is one of the leading causes of death in developed countries along with cardiovascular diseases. According to the International Agency for Research on Cancer [4], 14.1 millions of new cancer cases were diagnosed in 2012 and 8.2 million people died for cancer in the same year. The most common types are prostate cancer for men and breast cancer for women, followed by lung, colon and rectum, and stomach ones. The survival rate depends strongly on the type of cancer, being higher for breast and prostate and lower for lung and liver ones.

The techniques for treating cancer follow three basic approaches: surgery, chemotherapy and radiotherapy [1]. Surgery permits the physical removal of the tumour mass, and is therefore the most effective treatment for solid tumours (i.e., located in bone or muscle

tissue) when they are accessible and localized. Chemotherapy consists in the systemic administration of drugs that interfere with the proliferation mechanisms of the tumorous cells, and is often chosen for widespread cancers and for the treatment of metastases. Radiotherapy is performed by irradiating the tumour area with ionizing radiation (i.e., radiation which is able to extract electrons from the atomic shells, causing alterations in the chemical properties of the medium), and is often used for non-accessible or deep-seated tumours. The choice of the kind of treatment depends on the size, location and stage of development of the tumour; for nearly all cancer types, a combination of different treatment modalities is employed in order to ensure better tumour control [1].

For what concerns radiotherapy, the biological damage arises from the breaking of molecular bonds caused by ejection of valence electrons, producing free radicals which then undergo other chemical reactions that can be destructive for basic cell constituents, particularly the DNA. A complete treatment usually employs a total dose of 50 to 70 Gy [2], divided into fractions of 1.5 to 2 Gy each. Since the sensitivity of tumorous cells to radiation changes according to the different cell cycle phases, fractionation of the treatment permits to irradiate a higher number of cells in their most radio-sensitive phase, as well as allowing partial recovery from radiation damage to the healthy tissue [1].

1.1.1 Radiotherapy techniques

In current clinical practice, radiotherapy is mainly delivered using high-energy photon or electron beams. The use of heavier charged particles, such as protons, α-particles, lithium and carbon ions, has also been long recognized as a very effective way to produce cell damage [5], and clinical trials at various centres are demonstrating its potential both for tumour control and normal tissue sparing [6, 7, 8]. However, a discussion on this topic is beyond the purposes of the present work.

Photon radiotherapy can be delivered internally or externally. Internal radiotherapy is performed either by placing in the tumour small catheters containing a crystal of radioactive material (*brachytherapy*), or by administering a radio-pharmaceutical which has a high affinity to a specific cancerous tissue (*radiometabolic therapy*). External radiotherapy employs linear accelerator (often shortened in *linac*), which can rotate around a horizontal axis in order to irradiate the target from various angles. Moreover, the head of the accelerator can rotate along another axis which is orthogonal to the gantry rotation one. The intersection point of these two axes defines the *isocentre* of the machine, which should ideally correspond to the centre of the target volume.

Starting from early multiple-beam radiation therapy, a variety of delivery techniques has been developed in order to reach the dual goal of local tumour control and sparing of healthy tissue. This has been made possible by the advances in diagnostic imaging, especially with the invention of Computed Tomography (CT), which permits 3D visualization of the tumour volume for treatment planning, and by the progress in clinical accelerators capabilities. This led to the development of three-dimensional conformal radiotherapy (3DCRT), in which each of the chosen beams is shaped in order to adapt (*conform*) the contours of the dose distribution to the possibly complex shape of the target volume [2]. The shaping of individual fields was firstly achieved by using blocks of shielding material; today, complex field shapes are produced using Multi-Leaf Collimators (MLCs).

In order to treat cases in which the cancer surrounds a critical healthy structure, which would require a concave dose distribution, the beams can also be modulated in intensity to obtain a uniform dose inside the target which is conformed to the tumour shape. This technique is known as Intensity-Modulated Radiation Therapy (IMRT), and has gained widespread use because of the high level of conformation that can be achieved [3]. The entire treatment plan is composed of several irregularly-shaped sub-fields of different intensities, and high dose gradients are present between the target volume and neighbouring organs at risk (OAR).

An IMRT plan can make use of both fixed and variable gantry angles, and the various segments can be delivered individually or in a more complex way which involves movement of the collimator while the radiation field is on. In the first case, where the beam is switched on only when the collimator leaves are in fixed position, the treatment modality is defined *step-and-shoot* (or *segmental*) IMRT; in the second one, where the field shape changes during irradiation, it is known as *dynamic* IMRT. Both step-and-shoot and dynamic IMRT segments are delivered at fixed gantry angles. However, other techniques have been developed in which the gantry moves during irradiation. Examples are Intensity-Modulated Arc Therapy (IMAT), in which each intensity level used in the treatment is delivered in a single gantry rotation arc, and Volumetric Modulated Arc Therapy (VMAT), which introduces modulation of the dose rate as well [3].

Motion of the MLC leaves and of the gantry while the radiation field is on clearly allows better dose conformation through the use of a continuous set of different angles, and a considerable reduction of the time needed to deliver the treatment. However, such a treatment presents higher challenges during treatment delivery, and is more prone to errors due to inaccurate modelization of the leaves and gantry motion. Therefore, the delivery of a more complex treatment must be carefully evaluated in order to establish possible risks for the patient; thus, an accurate verification of the plan before delivery is mandatory [3].

1.1.2 Structure of a clinical linac

Fig. 1.1 shows the main components of a clinical linac: the photon beam is produced by bremsstrahlung, in the collision of electrons on a high-Z target. These electrons are generated by thermionic effect in the so-called *electron gun*, which is basically a simple electrostatic accelerator: a pulsed voltage is applied between a heated filament which acts as cathode and a grounded anode with a central hole that allows the passage of the electrons. The bunches of electrons are then accelerated in a radio-frequency (RF) cavity by means of an oscillating electric field, provided by a microwave generator. A vacuum pump ensures that no obstacle is present along their path, while various quadrupole magnets keep the beam focused in the transversal direction. A cooling system prevents an excessive heating of the active parts of the accelerator, which are also heavily shielded to avoid leakage of radiation. All these components are located in the arm of the linac or, for higher-energy linacs which require longer accelerating waveguides, in a nearby room.

Since the RF cavity is normally arranged horizontally in the gantry structure, bending magnets are used to deflect the electron beam towards the accelerator head, where the final photon field is produced and conformed. These magnets also focus and define the energy of the electron beam before its collision with the target, so that the energy spectrum of

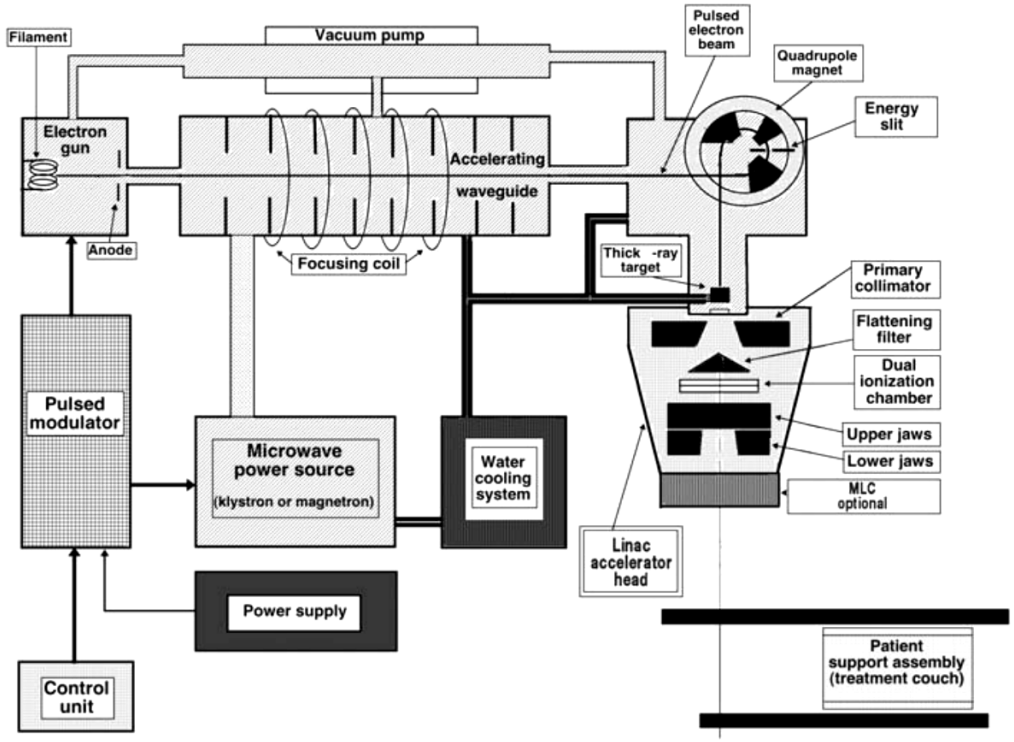

Figure 1.1: Scheme of a medical linear accelerator. Modified from [9].

the bremsstrahlung photons is controlled as well. The photon beam is collimated by the primary collimator, which defines a maximum circular field; in its interior the flattening filter is located, which is normally composed by a cone of stainless steel and designed to produce a radiation field which is flat under some well-defined conditions, usually defined as *uniformity configuration* (further described in Sect. 3.1.4).

The photon beam is then collimated by the secondary collimator which is composed by two independent jaws that define the width of the field along the y (inplane) direction, from a minimum of a few millimeters to a maximum of 40 cm. If neither the accelerator head nor the gantry have been rotated, this direction corresponds to the longitudinal axis of the treatment couch. The final shape of the field is produced by the Multi-Leaf Collimator (MLC), which is composed by 20 to 80 pairs of individually motorized leaves that can move independently along the x (crossplane) direction, which corresponds to the transversal axis of the treatment couch. The collimators are made of a high-Z material, usually tungsten. Between the primary and the secondary collimator the so-called monitor chamber is placed: it is composed by two independent parallel-plate ionization chambers, which are sealed to avoid response variations due to pressure and temperature changes. It is used to monitor the beam during treatment delivery, stop the irradiation when the predefined fluence is reached and check symmetry and flatness of the beam. The accelerator head is also equipped with devices that help to correctly position the patient, such as a field-defining light which illuminates an area of the same shape and size of the radiation field, and three orthogonal lasers which define the isocentre of the gantry.

Most of the medical accelerators now available are dual-energy machines, i.e., they can provide photon beams of two different well-defined maximum energies, usually in the range $4 - 25\,\mathrm{MeV}$. Moreover, some are also designed for electron radiotherapy, which is used to treat various superficial or subcutaneous diseases. If a linac has to provide electron beams as well, the X-ray target and flattening filter are positioned on retractable trays so that they can be removed, and retractable copper or lead scattering foils are inserted in their place to shape the electron beam according to treatment needs.

1.1.3 Treatment planning and verification methods

An IMRT treatment plan is intrinsically more complex than traditional conformal therapy, not only because of the higher number of beams and variable intensity of each one of them, but also because of the higher target dose with respect to traditional treatments and steep dose gradients between the target and organs at risk, which make setup inaccuracies much more dangerous [3]. Therefore, tools for positioning check are of vital importance for IMRT: this has lead to the development of the so-called Image-Guided Radiation Therapy (IGRT), where extensive use of localization and imaging tools is made not only for diagnostic purposes but also at the time of treatment. In this way, the accuracy in dose delivery is greatly increased and margins that account for setup error or internal target motions can be further reduced.

Some additional issues can arise from a more complex treatment planning strategy that can be employed for IMRT, called *inverse planning*, whose approach to the problem of calculating the best dose distribution is reversed with respect to the traditional technique, known as *forward planning*. In the latter, after a 3D image of the tumour is obtained by means of CT scans or magnetic resonance, the individual beams are shaped to match the target borders on each plane, and then the total delivered dose is computed as the final objective. With the former, the desired target dose is established first, along with the maximum dose that can be delivered to nearby OARs, and then the individual beam directions, shapes and intensities are calculated in order to produce the prescribed dose map. This is concretely carried out by using mathematical optimization algorithms defined in a software called Treatment Planning System (TPS), which handles the huge number of parameters that can be varied in each plan.

Due to the intrinsic complexity of this strategy, several trials are normally needed before an acceptable plan is produced. Constraint on the maximum acceptable dose must be defined in all regions near the treatment area, in order to avoid unexpected high-dose regions outside the target which would result in normal tissue complications. Other issues which require consideration are the accurate modelization of the margins of each radiation field (*penumbra region*, defined in Sect. 3.1.4) and of the depth dose profile, particularly in the surface region (*build-up* region, see Sect. 2.1.3); possible transmission through the collimator leaves must be taken into account as well.

After the treatment plan has been defined, an accurate verification of the resulting dose map is mandatory in order to detect possible miscalculations by the TPS, which may be not suited to handle the complexity of an IMRT plan. The consistency of the 3D representation of the target volume must be checked, both by means of TAC slices acquired in

the axial planes and from images obtained in the coronal and sagittal ones[1]. Some checks on the composite dose distribution resulting from the combination of individual beams can be performed by means of independent verification algorithms of the TPS, but these do not avoid errors in treatment delivery, which can be prevented only by frequent and accurate quality assurance (QA) tests of the accelerator performance. A comprehensive pre-treatment verification method, based on in-phantom measurements in multiple orthogonal planes, is a good and relatively simple solution to identify possible inaccuracies both in treatment planning and delivery at the same time.

1.2 Aims of this work

The work herein described is part of a wider project called RADIA, which aims at developing a novel detection system that will constitute a user-friendly tool to perform in-phantom verification of complex IMRT treatments in a simple and comprehensive way. The RADIA project started in 2008 in Seville, as a collaboration between various research centres of the city: the Department of Atomic, Molecular and Nuclear Physics (FAMN) and the School of Engineering of the University, the Fundamental Nuclear Physics (FNB) unit at the Centro Nacional de Aceleradores (CNA), the 'Virgen Macarena' University Hospital, and the private company Instalaciones Inabensa S.A.. In particular, the goal of the project is to develop a device which is able to provide online, measurement-based dose maps in the axial planes of a cylindrical phantom. This is motivated by the fact that, even if in this planes the comparison with CT scans of the patient anatomy are more meaningful and straightforward, very few devices exist that can actually measure 2D axial dose maps. The most used are of course radiochromic films (Sect. 2.3.3), but they require much time for development and calibration and are not suited for online measurements. Digital devices (Sect. 2.4.1) are normally arranged in the coronal plane, and rely on complex reconstruction algorithms in order to obtain information on the axial dose.

The measuring device is based on silicon detector technology, since it can provide a spatial resolution comparable to that of films together with a fast readout by means of discrete electronics [10]. This kind of technology was developed in the field of high-energy physics, where high-resolution tracking detectors were needed for the analysis of the products of particle decay: in order to obtain positional information, the detectors were segmented into strips [11] and then into pixel [12], each one with its own electronic chain. Strip detectors can be segmented on one side, or on both sides along two perpendicular directions: they are called single-sided in the first case, and double sided in the second.

The RADIA collaboration performed a first feasibility study [13] with a commercial single-sided silicon strip detector, manufactured by Micron Semiconductors Ltd. It was firstly housed in a slab phantom and placed orthogonally to the beam axis (i.e., in the coronal plane of a hypothetical patient); its dosimetric response was analysed and compared with routine QA hospital measurements. A cylindrical rotating phantom was then designed to house the detector with its active area parallel to the beam axis: its angular response was studied at different relative angles between the directions of the strips and the gantry,

[1] The *axial* planes are the ones orthogonal to the longitudinal axis of the body. The *coronal* planes are orthogonal to the direction of motion of the body, while the *sagittal* ones are parallel to the body symmetry plane.

and compared with TPS calculation to test consistency in the measured data. As a final benchmark for this novel technique, the detector was irradiated with a simple treatment plan. The dose map in the axial plane was reconstructed using an algorithm based on the Radon transform [14], starting from measurements at different detector angles, and compared with the TPS plan: remarkable agreement was found between the two. The work carried out with this first prototype resulted in a patent submitted in September 2011 to the Spanish Patent and Trademark Office (OEMP – Oficina Española de Patentes y Marcas, Spanish Minister of Industry, Tourism and Trade) [14].

In order to improve the performance of the first prototype, a second detection system has been carefully designed and built, again in collaboration with Micron Semiconductor Ltd [15]. It is made of two single-sided detectors mounted in a back-to-back configuration, with the strips of each detector perpendicular to those of the other: it has therefore been called Dual Single-Sided Silicon Strip Detector (DSSSSD). Most of the elements that surround the active layers have been made of Kapton in order to reduce the perturbation introduced by the detector. As for the previous prototype, two phantoms have been designed to house it: a slab one, to be used for dosimetric characterization, an a cylindrical rotating one, to perform dose measurements in the axial plane.

This work presents the first characterization of the DSSSSD placed in the slab phantom, orthogonally to the beam axis. In particular, it focuses on studying linearity and reproducibility of the detector response, performing the calibration in the coronal plane, and making a comparison of the results with routine hospital measurements under different irradiation conditions. This is the first preliminary step to be taken to ensure that the response of the DSSSSD is reliable, and to understand the underlying physical processes and possible sources of uncertainty in axial plane measurements.

This work also discusses Monte Carlo simulations that have been carried out in order to obtain a theoretical estimation of the relevant magnitudes. During the first feasibility study, accurate simulations [16, 17] of the experimental setup were performed in order to estimate the sensitivity of the detector both in the slab and the cylindrical phantom, using the GEANT4 simulation toolkit. GEANT4 [18, 19] is a general-purpose, C++-based Monte Carlo code to simulate radiation transport through matter. It was originally developed for high-energy physics, but physical models for lower-energy interactions have been implemented over the years. At present, it has been validated for energies between 250 eV and 10 TeV, depending on the type of particles involved and the physical models that are considered [20, 21, 22, 23]. In recent years, the collaboration GEANT4-DNA [24] aims at extending the validity range to the 1 eV scale, including diffusion of chemical radicals in water [25].

GEANT4 is based on the principles of Object-Oriented Programming (OOP), which guarantee high flexibility due to the modular structure of the code. It includes classes for the detailed simulation of geometrical elements and materials, and the definition of all particles included in the Particle Data Group database. Other tools permit to define the experimental setup (particle sources, detecting volumes...), the physical models that describe the interactions, and the output magnitudes to be calculated in the simulation [26]. Due to its high versatility, it has been applied in a wide variety of fields, ranging from high-energy particle physics and astrophysics to medical physics, electronics and aerospace engineering.

In the framework of the RADIA project, GEANT4 has been used both to study the viability of the axial setup and as an additional validation tool in the study of the response of the detector. Given the very good results obtained for the first prototype, it was decided to continue the simulation work also for the new detection system, in the belief that comparison between simulation and experiment provides valuable insight on the physical processes at play.

After this introductory chapter, this work is divided into four parts. Chapter 2 discusses the fundamentals of dosimetry, in particular the dose deposition process, dosimetric magnitudes and the theory of dose measurement. The most common types of dosimeters used in clinical practice and various detectors developed for treatment verification are also presented. Chapter 3 describes in detail the experimental setup, the measurements and the GEANT4 simulations that have been carried out to characterize and validate the response of the system. The results of both experimental measurements and GEANT4 simulations are presented in Chapter 4, along with the calibration of the DSSSSD and a comparison with hospital measurements. Finally, Chapter 5 draws the conclusions of the present work, and discusses the further aims of the RADIA project.

Chapter 2

Dosimetry: principles and techniques

The fundamental principle of radiotherapy is using the energy deposited by ionizing radiation to destroy tumorous cells without affecting vital organs. Biological damage is a direct consequence of chemical changes induced by the breaking of molecular bonds caused by ionization; in clinical practice, it is usually estimated from the absorbed dose, i.e. the energy per unit mass released by incident radiation in the tumour volume. The aim of dosimetry is therefore the quantitative measurement of the energy per unit mass deposited in a given volume, in order to estimate the biological damage.

This chapter is divided into four parts. In the first one, the basic mechanisms by which γ-rays deposit their energy in a medium are discussed, along with the basic dosimetric magnitudes and one of the fundamental concepts of dosimetry, the so-called *electronic equilibrium*. The second one presents a discussion of cavity theory, which relates the dose measured by a dosimeter to the one that would be deposited in the medium if the dosimeter was not present. In the third one, the most common types of dosimeters used in clinical practice are discussed; while the fourth presents the detectors that have been specifically developed for the verification of complex treatments, with their advantages and disadvantages.

The main references on which this chapter is based are [27], [28], [9], and [29], this last one especially for cavity theory.

2.1 Dose deposition

When a beam of ionizing radiation strikes a medium, it loses part of its initial energy to it through a variety of physical processes. The probability of an interaction of a given type to occur depends strongly on the type, energy and charge state of the incident particle, as well as from the density and scattering properties of the medium. In all cases, however, the energy deposition is a stochastic process: all the dosimetric magnitudes described in the following are defined as average values, and are meaningful only if a large number of primary particles hits the target. The volume on which they are defined has to be small if compared to macroscopic ones, but big enough for a statistically significant number of interactions to take place in it.

2.1.1 Interaction of radiation with matter

Since photons are neutral particles, they do not deposit their energy directly by ionization, as charged particles do. The energy deposition is a two-step process: in the first, photons give their energy to atomic electrons; in the second, electrons transfer their energy to the surrounding medium, by ionization or bremsstrahlung. Depending on the energy of the incident photons, the first step can be achieved via photoelectric effect, Compton effect, or pair production. The relative probability for these processes to occur is shown in Fig. 2.1: it can be seen that at radiotherapy energies Compton effect is highly dominant.

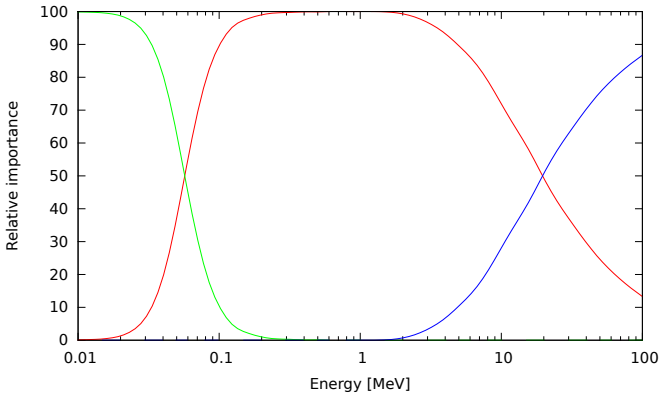

Figure 2.1: Relative importance, in terms of percent contribution in the transferred energy, of photoelectric absorption (green), Compton scattering (red) and pair production (blue), as a function of the energy of the incident beam in water. The plotted data are taken from [27].

When a Compton scatter takes place, the photon transfers part of its energy to an atomic electron, which is freed from the atomic shell and set in motion. The transferred energy E_{tr} is defined as

$$E_{\mathrm{tr}} \simeq E_{\mathrm{inc}} - E_{\mathrm{C}}$$

where E_{inc} and E_{C} are the energies of the incident and Compton photons, respectively. The ionization energy is not considered, since it is usually negligible if compared to the other energies that come into play.

This transferred energy acquired by the electron is then lost to the surrounding medium, by direct ionization or by production of bremsstrahlung photons. Therefore

$$E_{\mathrm{tr}} = E_{\mathrm{ion}} + E_{\mathrm{rad}} \tag{2.1}$$

Since radiative processes take energy far from the region of interest, the absorbed dose is directly related to the energy lost by ionization. As shown in Table 2.1, bremsstrahlung becomes important if the beam energy is higher than 10 MeV, so it can generally be neglected in the energy range of interest for radiotherapy.

2.1.2 Dosimetric magnitudes

In order to understand quantitatively the processes above described, the following quantities are introduced, which can be defined both for ionizing and non-ionizing particles:

$\mathbf{E}_\gamma$	$\mathbf{E}_{\mathrm{tr}}$	$\mathbf{E}_{\mathrm{ion}}$	$\mathbf{E}_{\mathrm{rad}}$
0.01	0.00925	0.00925	0
0.1	0.0148	0.0148	0
1	0.440	0.0440	0
10	7.33	7.07	0.26
100	95.8	71.3	24.5

Table 2.1: Mean value [MeV] of transferred, ionization and bremsstrahlung energy for various energy of the incident beam in water. This table is taken from [27].

- **Fluence:** total number of particles that cross the element of area $\mathrm{d}a$, orthogonal to the direction of the beam
$$\Phi = \frac{\mathrm{d}N}{\mathrm{d}a}$$
- **Fluence rate (or flux):** number of particle that cross the element of area $\mathrm{d}a$ (orthogonal to the direction of the beam) in a time $\mathrm{d}t$
$$\dot{\Phi} = \frac{\mathrm{d}N}{\mathrm{d}a\,\mathrm{d}t}$$
- **Energy fluence:** total energy that crosses the element of area $\mathrm{d}a$
$$\Psi(E) = \frac{\mathrm{d}E}{\mathrm{d}a}(E) = \frac{E\ \mathrm{d}N(E)}{\mathrm{d}a} = E\,\Phi(E)$$

For non-ionizing particle, such as photons, the attenuation coefficient, which is the fraction of particles that are lost from the beam in the length $\mathrm{d}x$ due to interactions with atomic electrons, can be expressed as

$$\mu = -\frac{\mathrm{d}N/N}{\mathrm{d}x}$$

The integration of this equation gives the exponential attenuation of photons in matter: $N(x) = N_0\, e^{-\mu x}$. The mass attenuation coefficient, μ/ρ, can also be defined.

In order to obtain the energy lost in the medium per unit mass, an infinitesimal volume $\mathrm{d}v$ is considered, with thickness $\mathrm{d}x$ and surface area $\mathrm{d}a$, which is crossed by N incoming photons of the same energy E_γ. Therefore the lost energy $\mathrm{d}E$ is

$$\mathrm{d}E = \mathrm{d}N E_\gamma = \mu N\,\mathrm{d}x E_\gamma$$

and the lost energy per unit mass is

$$\frac{\mathrm{d}E}{\mathrm{d}m} = \frac{\mu N\,\mathrm{d}x}{\rho\,\mathrm{d}v} E_\gamma = \left(\frac{\mu}{\rho}\right) E_\gamma \frac{N}{\mathrm{d}a} = \left(\frac{\mu}{\rho}\right) E_\gamma \Phi = \left(\frac{\mu}{\rho}\right) \Psi \tag{2.2}$$

In an analogous way, the mass transfer coefficient $(\mu/\rho)_{\mathrm{tr}}$ and the mass absorption coefficient $(\mu/\rho)_{\mathrm{abs}}$ are defined as

$$\left(\frac{\mu}{\rho}\right)_{\mathrm{tr}} = \frac{\mu}{\rho}\,\frac{E_{\mathrm{tr}}}{E_\gamma} \qquad\qquad \left(\frac{\mu}{\rho}\right)_{\mathrm{abs}} = \frac{\mu}{\rho}\,\frac{E_{\mathrm{abs}}}{E_\gamma}$$

Using these expressions, the following ones can be obtained:

$$\frac{\mathrm{d}E_{\mathrm{tr,abs}}}{\mathrm{d}m} = \frac{\mu}{\rho} E_{\mathrm{tr,abs}} \Phi = \left(\frac{\mu}{\rho}\right)_{\mathrm{tr,abs}} E_\gamma \Phi = \left(\frac{\mu}{\rho}\right)_{\mathrm{tr,abs}} \Psi \tag{2.3}$$

This is valid if the beam has a defined energy. In the case of a continuous energy distribution, the attenuation coefficient needs to be averaged on the energy distribution, obtaining

$$\frac{\mathrm{d}E}{\mathrm{d}m} = \frac{\overline{\mu}}{\rho} \Psi_{\mathrm{tot}} \tag{2.4}$$

For directly ionizing particles, such as electrons, the stopping power is defined as the energy that each particle loses per unit length:

$$S = -\frac{\mathrm{d}E}{\mathrm{d}x}$$

As for the attenuation coefficient, the mass stopping power S/ρ can be defined. Another important quantity is the range of the particle, i.e. the distance it travels before it stops:

$$R = \int_{E_0}^{0} -\frac{1}{S}\,\mathrm{d}E$$

Considering again N particles entering an infinitesimal volume $\mathrm{d}v$, of surface area $\mathrm{d}a$ and thickness $\mathrm{d}x$, the energy deposited in it can be expressed as $\mathrm{d}E = NS\,\mathrm{d}x$, and the energy deposited per unit mass is

$$\frac{\mathrm{d}E}{\mathrm{d}m} = \frac{S}{\rho}\frac{N}{\mathrm{d}a} = \frac{S}{\rho}\Phi \tag{2.5}$$

Again, in the case of a continuous energy distribution, the average of the stopping power has to be considered:

$$\frac{\mathrm{d}E}{\mathrm{d}m} = \frac{\overline{S}}{\rho}\Phi_{\mathrm{tot}} \tag{2.6}$$

2.1.3 KERMA, dose and electronic equilibrium

KERMA (Kinetic Energy Released per unit MAss) is defined as the energy that is transferred by incident photons to charged particles in the infinitesimal volume $\mathrm{d}v$. According to Eq. (2.3), it can be calculated as

$$K = \frac{\mathrm{d}E_{\mathrm{tr}}}{\mathrm{d}m} = \left(\frac{\mu}{\rho}\right)_{\mathrm{tr}} \Psi \tag{2.7}$$

The total KERMA is obviously the sum of a term due to ionization (collisional KERMA, K_{col}), and one due to the production of bremsstrahlung photons (radiative KERMA,

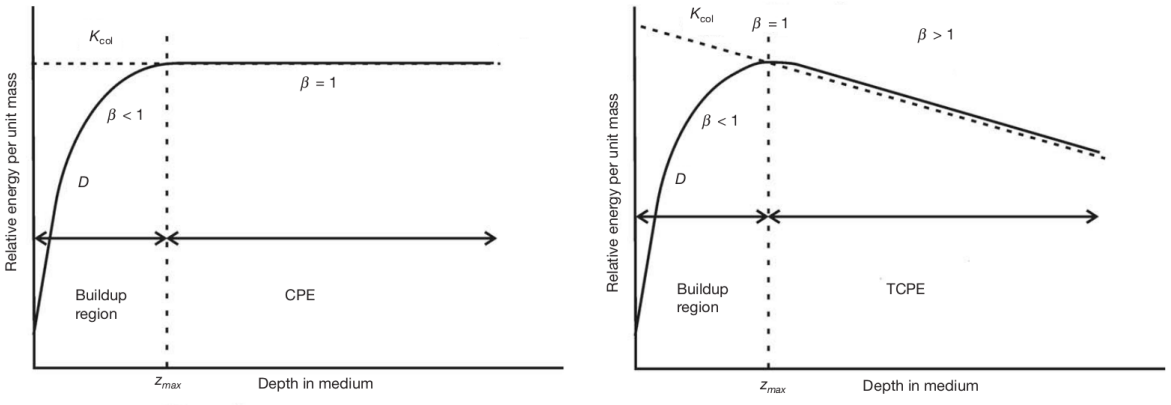

(a) CPE **(b)** TCPE

Figure 2.2: Relation between KERMA, dose and electronic equilibrium, in the hypothetical case in which the photon beam is not attenuated (a), and in the realistic one in which attenuation occurs (b). From Ref. [9].

K_{rad}). Since only non-radiative processes contribute to the collisional KERMA, according to Eq. (2.1) and 2.3 it can be written as

$$K_{\mathrm{col}} = \frac{\mathrm{d}E_{\mathrm{abs}}}{\mathrm{d}m} = \frac{(E_{\gamma}^{\mathrm{in}} - E_{\gamma}^{\mathrm{out}})}{\mathrm{d}m} = \left(\frac{\mu}{\rho}\right)_{\mathrm{abs}} \Psi \tag{2.8}$$

where $E_{\gamma}^{\mathrm{out}}$ includes the contribution of all the photons leaving the volume of interest: not only Compton-scattered photons, but bremsstrahlung ones as well.

As said in the Introduction, the dose is defined as the energy per unit mass absorbed by a volume $\mathrm{d}v$ of the medium. The absorbed energy is obviously the difference between the energy entering the volume $\mathrm{d}v$ and the one leaving it, and separating the contribution of radiation and charged particles

$$\mathrm{d}E = (E_{\gamma}^{\mathrm{in}} - E_{\gamma}^{\mathrm{out}}) + (E_{\mathrm{e}^-}^{\mathrm{in}} - E_{\mathrm{e}^-}^{\mathrm{out}})$$

that is to say

$$D = \frac{\mathrm{d}E}{\mathrm{d}m} = \frac{(E_{\gamma}^{\mathrm{in}} - E_{\gamma}^{\mathrm{out}})}{\mathrm{d}m} + \frac{(E_{\mathrm{e}^-}^{\mathrm{in}} - E_{\mathrm{e}^-}^{\mathrm{out}})}{\mathrm{d}m} = K_{\mathrm{col}} + \frac{(E_{\mathrm{e}^-}^{\mathrm{in}} - E_{\mathrm{e}^-}^{\mathrm{out}})}{\mathrm{d}m} \tag{2.9}$$

The condition in which $(E_{\mathrm{e}^-}^{\mathrm{in}} = E_{\mathrm{e}^-}^{\mathrm{out}})$ is called electronic equilibrium: for every particle of a given kind that enters the volume $\mathrm{d}v$ there is another of the same kind and energy that leaves it. If this is the case, $D = K_{\mathrm{col}}$.

Fig. 2.2 shows in a very clear way the connection between KERMA, dose and electronic equilibrium. In the hypothetical case in which the photon beam is not attenuated (Fig. 2.2a), KERMA does not depend on the depth in the medium, since the probability for a Compton scatter to occur remains constant. The same cannot be said for the absorbed dose: in the surface region there is no electronic equilibrium, since electrons start to be

produced, and the number of particles leaving a given volume is greater than that of the entering ones. This is called the *build-up* region. The dose keeps increasing until a depth d of the same order of the range R of the electrons is reached: at this point, the charged particle fluence becomes constant and electronic equilibrium is achieved.

In a real situation, however, the photon beam is attenuated, and complete charge equilibrium cannot be achieved (Fig. 2.2b). The probability for a Compton scatter to occur decreases alongside with the decrease of the number of photons, and so does KERMA. This decrease is linear because $\frac{\mathrm{d}N}{\mathrm{d}x} \propto N(x)$, as follows by the exponential attenuation of photons. The absorbed dose increases for a depth $d \lesssim R$, reaches a maximum, and then decreases alongside with the decrease of KERMA. We notice that for a given depth the KERMA is always a bit smaller than the dose. This is again due to the attenuation of photons, since KERMA depends on the number $N(d)$ of photons at the depth d we are considering, while the dose depends on the number of photons at a depth $d' < d$, due to the non-zero range of the electrons.

Near the maximum, the so-called Transient Charged Particle Equilibrium (TCPE) is achieved. As it will be discussed in the next section, this is the ideal condition to measure the dose, as it depends less on the depth at which the dosimeter is put.

2.2 Dose measurement: cavity theory

In order to measure the dose, a radiation sensitive device, called dosimeter, has to be put in the medium. This device generally introduces a perturbation, and the dose it measures does not correspond to the energy that would be absorbed in the same portion of medium in the absence of the dosimeter. The correspondence between the dose absorbed by the dosimeter and the dose in the medium if it was not present is given by cavity theory. The name 'cavity' to define a dosimeter is due to the fact that, historically, the first dosimeters were gas-filled chambers.

Because of the two-step nature of dose deposition, the relevant physical processes taking place in the dosimeter will be different according to whether only secondary electrons need to be considered or some properties of the photon field influence the dose measurement as well. The boundary between these situations is set by the range R of secondary electrons, compared with the typical dimension d of the cavity. Three different situations, illustrated in Fig. 2.3, can be distinguished:

- $d \ll R$: the interactions taking place in the cavity are almost entirely due to secondary electrons produced outside it (Bragg-Gray conditions);
- $d \gg R$: the absorbed dose is mainly due to electrons produced inside the cavity (CPE conditions);
- $d \simeq R$: intermediate situation in which electrons produced both inside and outside the cavity contribute to the absorbed dose (Burlin cavity theory).

Two important approximations are common to all cavity theories: first, both the material of which the cavity is made and the one in which it is immersed are supposed to be homogeneous; second, the primary particle field must be uniform in both the cavity and

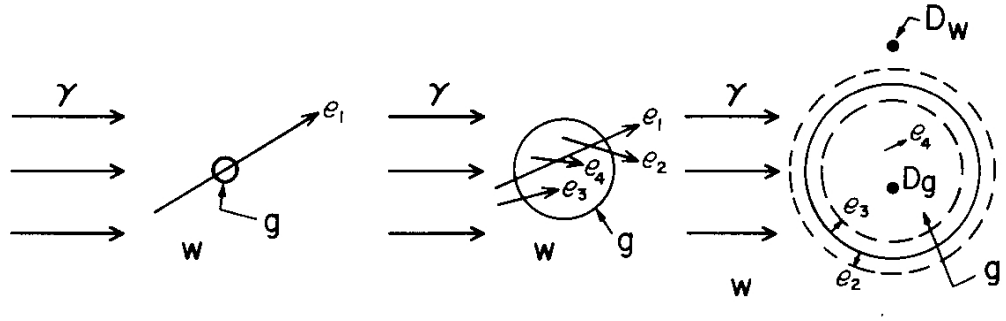

Figure 2.3: Illustration of the transition from small to intermediate to big cavities, when compared with the secondary electron range. Taken from [29].

the surrounding medium. If photon attenuation has to be taken into account, a correction factor is needed.

2.2.1 Small cavities: Bragg-Gray and Spencer-Attix cavity theory

Bragg-Gray cavity theory is based on the two following hypotheses:

a) The cavity size has to be small enough so that its presence does not perturb the charged particle field or its energetic distribution.[1] This means that the charged particle fluence is the same inside and outside the cavity. In particular, if the cavity is made of a material which is very different in density from that of the surrounding medium, backscattering at the interface has to be negligible.

b) The dose deposited in the cavity is only due to charged particles crossing it, i.e., no electrons are produced or stop in the cavity. This means that in the cavity charged particle equilibrium is achieved, and that inside it photon interactions do not take place. Moreover, no processes that take energy far from the region of interest occur: bremsstrahlung photons and δ-electrons are not produced. The energy release in the cavity must therefore be a continuous process, made of many small steps: this is called the continuous slowing-down approximation (CSDA).

If these hypotheses are valid, the dose in both the medium and the cavity is obtained from Eq. (2.5):

$$D_{m,c} = K^{\mathrm{col}}_{m,c} = \left(\frac{S(E)}{\rho}\right)_{m,c} \Phi(E)\Big|_{E=E_{\mathrm{e}-}}$$

where Φ is the charged particle fluence and S/ρ is the mass stopping power, both calculated at an energy E equal to that of the incoming electrons. Normally, these electrons are not mono-energetic, and therefore this expression has to be integrated on the energy spectrum

[1] Taking this hypothesis to its furthest extent would mean that no dose at all is deposited in the cavity. It is of course an approximation, grounded on the fact that the cavity is small and therefore only a negligible fraction of energy is lost inside it.

$\sigma(E)$:

$$D_{m,c} = \int_{\sigma(E)} \Phi(E) \left(\frac{S(E)}{\rho}\right)_{m,c} \mathrm{d}E \;=\; \Phi_{\mathrm{tot}} \overline{\left(\frac{S}{\rho}\right)}_{m,c}$$

where $\Phi_{\mathrm{tot}} = \int_{\sigma(E)} \Phi(E)\,\mathrm{d}E$ is the total fluence and $\overline{S}/\rho$ is the average mass collisional stopping power.

Since the charged particle fluence is the same in the medium and in the cavity, the ratio of the dose in the medium and in the cavity is the ratio of the respective stopping power:

$$\frac{D_m}{D_c} = \frac{(\overline{S}/\rho)_m}{(\overline{S}/\rho)_c} \equiv \overline{\left(\frac{S}{\rho}\right)}_c^m \tag{2.10}$$

Spencer-Attix cavity theory is a correction to the Bragg-Gray one when the production of high-energetic δ-electrons, both inside and outside the cavity, is taken into account. They are included in the equilibrium spectrum Φ, along with the Compton-generated secondary electrons. Since the two Bragg-Gray approximations still hold, the charged particle spectrum has to be the same both in the cavity and in the medium.

An arbitrary energy threshold Δ is introduced, which is related to the minimum energy needed to cross the cavity. Electrons with energy higher than Δ ('fast' electrons) are assumed to transfer it to a range at least as large as the cavity, while the ones with lower energy ('slow' electrons) are assumed to deposit the it in the place of production (zero-range approximation). The electron fluence is therefore limited to particles with energy higher than Δ: the particles whose energy falls below this threshold are assumed to stop on the spot and do not contribute to the fluence.

The dose in the medium and in the cavity can be written as

$$D_{m,c} = \int_{\sigma(E>\Delta)} \Phi_\Delta(E) \left(\frac{L_\Delta(E)}{\rho}\right)_{m,c} \mathrm{d}E + TE_{m,c}(\Delta) \tag{2.11}$$

where $\Phi_\Delta(E)$ is the fluence of particles with energy higher than Δ, $L_\Delta(E)/\rho$ is the restricted stopping power with energy threshold Δ, and $TE_{m,c}(\Delta)$ is called the *track-end* term, which takes into account the energy lost when the energy of the particle falls below Δ. It can be estimated as

$$TE_{m,c}(\Delta) = \int_0^\Delta \Phi_\Delta(E) \left(\frac{L_\Delta(E)}{\rho}\right) \mathrm{d}E \;\simeq\; \Phi_\Delta(\Delta) \left(\frac{L_\Delta(\Delta)}{\rho}\right) \Delta \tag{2.12}$$

by assuming the integrand to be constant in the range $[0, \Delta]$. This is justified by the CSD approximation combined with the zero-range one.

The ratio of the dose deposited in the medium and in the cavity can therefore be estimated.

2.2.2 Big cavities: CPE cavity theory

If the cavity is much larger than the secondary electrons range, the absorbed dose will be mostly due to particles generated by primary photons inside it. The presence of a wall, or of

any interface with the outside medium, can be neglected. CPE cavity theory assumes that electrons entering the cavity from the outside medium are such a small fraction that their contribution to the absorbed dose is not significant, and that inside the cavity charged particle equilibrium is achieved. The deposited dose is therefore due to the collisional KERMA released by primary photons, and according to Eq. (2.8)

$$\frac{D_m}{D_c} = \frac{K_{\text{col}}^m}{K_{\text{col}}^c} = \frac{(\overline{\mu_{\text{abs}}}/\rho)_m}{(\overline{\mu_{\text{abs}}}/\rho)_c} \equiv \overline{\left(\frac{\mu_{\text{abs}}}{\rho}\right)}_c^m \tag{2.13}$$

under the assumptions that the photon field is the same in both the cavity and the medium and that bremsstrahlung can be neglected.

2.2.3 Intermediate cavities: Burlin cavity theory

The Burlin cavity theory comes as a generalization of both the Bragg-Gray and CPE ones, in order to effectively describe the transition between the two as the cavity size grows. It makes several approximations, many of which are needed in order to link the different hypotheses on which the Bragg-Gray and CPE theories are based:

1) The medium of the cavity and the surrounding one are both supposed to be homogeneous;

2) A uniform photon field exist in both the cavity and the surrounding medium, which does not change at the interface between the two;

3) Charged-particle equilibrium is achieved in the cavity and in the surrounding medium (except possibly within the maximum electron range from the cavity interface);

4) The secondary electron spectrum $\Phi^{\text{eq}}(E)$ is the same in the cavity and in the medium;

5) The electron fluence entering the cavity from the outside medium is attenuated exponentially with distance, without changing its energy distribution;

6) The electron fluence originating in the cavity grows exponentially with distance until it reaches its equilibrium value, with the same energy distribution that it would have in the medium.

If all these hypotheses hold, the ratio of the dose in the medium and in the cavity can be written as

$$\frac{D_m}{D_c} = d \cdot \overline{\left(\frac{S}{\rho}\right)}_c^m + (1-d)\overline{\left(\frac{\mu_{\text{abs}}}{\rho}\right)}_c^m \tag{2.14}$$

where $\overline{(S/\rho)}_c^m$ and $\overline{(\mu_{\text{abs}}/\rho)}_c^m$ are the ratios of stopping powers and absorption coefficients defined above and d is a parameter related to the size of the cavity. It approaches 1 for small cavities (Bragg-Gray limit) and 0 for big ones (CPE limit).

Considering the hypotheses 4) and 5), the parameter d can be estimated as

$$d = \frac{\overline{\Phi_{\text{out}}(l)}}{\Phi^{\text{eq}}} = \frac{\frac{1}{L}\int_0^L \Phi^{\text{eq}} e^{-\beta l}\,\mathrm{d}l}{\Phi^{\text{eq}}} = \frac{1-e^{-\beta L}}{\beta L} \tag{2.15}$$

where $\overline{\Phi_{\text{out}}(l)}$ is the fluence of electrons originated outside the cavity at depth l inside it, averaged over the mean chord L, and β is the attenuation coefficient. Repeating the calculation with an exponential growth of electrons generated inside the cavity brings to an estimation of $1 - d$ which is consistent to the one just obtained.

Burlin cavity theory is discussed in further detail in Ref. [29]

The application of cavity theory to real dosimeters is not straightforward: many correction factors are needed in order to take into account the various non-idealities. The most common are the following:

- **fluence factor**: corrects for the attenuation of the photon field with increasing depth in the medium
- **dose gradient factor**: takes into account the possible non-homogeneous distribution of dose inside the cavity
- **wall correction factor**: accounts for the effect of the wall of the cavity and for the scattering at the interface between different media
- **temperature and density corrections**: if the cavity is filled with gas (as is most common), changes in temperature and pressure have to be taken into account.

2.3 Dose measurement: dosimeters

A dosimeter is any device that gives a reading r that is linear with the dose absorbed by its sensitive volume in a well-defined range. However, the quantity of interest is not the dose absorbed by the dosimeter itself, but the dose that would be absorbed by the same portion of the surrounding medium if the dosimeter was not present.

Dosimeters must therefore be calibrated, i.e., the proportionality factor that links the reading r with the absorbed dose D_m has to be found. If the response is linear, this factor is of course unique. Since direct application of cavity theory is infeasible, calibration is usually done by measuring the dose at a reference point, in which the dose is known by other means.

Dosimeters differ firstly in the dose-dependent magnitude, which can be charge, light, heat, or a change in the optical or chemical properties of the material. Each type has different advantages and disadvantages in terms of spatial resolution, linearity, reproducibility, energy and angular dependence, and change in sensitivity due to repeated irradiation. Some are reusable and their readout is immediate, others need further post-irradiation processing and have to be disposed of after use.

In the following sections, the most common types of dosimeters are presented, along with some of their advantages and disadvantages.

2.3.1 Ionization chambers

Ionization chambers have been the first dose-measuring devices and are still widely used both for calibration of other types of dosimeters and for single-point dose verification when

high dose gradients are not present. In their basic form, they consist of two electrodes separated by an insulating gas, to which a polarizing voltage is applied. When radiation strikes the chamber, the gas is ionized and the flow of positive and negative particles produces a current that can be measured. The applied voltage has to be high enough to prevent recombination and ensure complete charge collection, but low enough to avoid further ionization by secondary electrons.

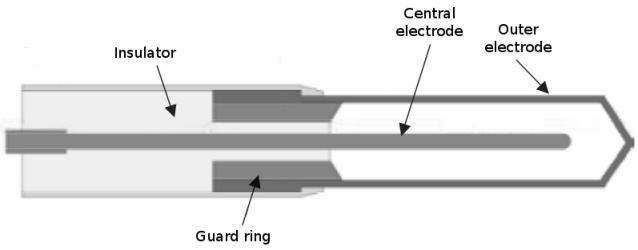

Figure 2.4: Schematic diagram of a cylindrical (Farmer-type) ionization chamber. Adapted from [9].

The dose absorbed by the cavity can be obtained as $D_c = \frac{Q}{m}\frac{W}{e}$ where Q is the total charge *of one sign* generated by the incoming radiation, $m = \rho v$ is the mass of the gas in the cavity and W/e is the ionization potential per unit charge. Dose is therefore directly proportional to the total charge produced. Cavity theory and all the necessary correction factors could then be applied to obtain a theoretical estimation of the dose in the surrounding medium if the chamber was not present.

In practice, two types of ionization chambers exist: the cylindrical ones, with two concentric electrodes, and the parallel plate ones. The typical volume is $0.6\,\mathrm{cm}^3$. Both types are connected to an electrometer that integrates the generated current to obtain the total charge produced by incoming radiation (Fig. 2.5). Usually a guard ring or grid is present, in order to prevent an eventual leakage current from reaching the electrodes and improve field uniformity in the sensitive volume. The wall of the chamber is usually made of a low-Z material, in order to minimize backscattering at the interface with the external tissue-equivalent medium.

2.3.2 Semiconductor detectors

A semiconductor dosimeter can be considered a solid-state ionization chamber: the incident ionizing radiation creates electron-hole pairs in the body of the detector, which are collected by two electrodes and produce a measurable current. Due to the much higher density of the solid and the lower ionization potential of the semiconductor, these detectors have a much higher sensitivity and a better spatial resolution than ionization chambers.

Normally these detectors consist of p- or n-doped silicon substrate to which an opposite doped surface layer is implanted, thus creating a p-n junction. Due to their different densities in the p- and n-side, majority carriers diffuse through the junction, producing an electric field that opposes further diffusion, until an equilibrium situation is reached. A layer in which majority carriers are not present, called depletion layer, is thus created. When radiation strikes the semiconductor, electron-hole pairs are produced, which can be

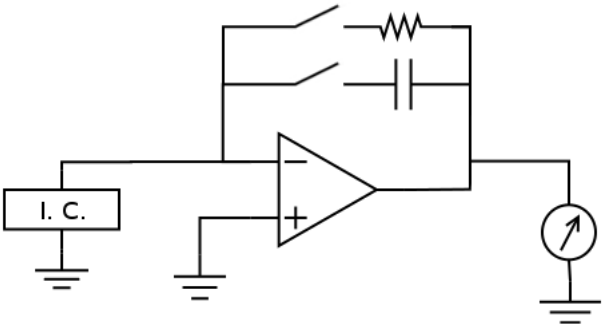

Figure 2.5: Circuital diagram of an electometer in its basic configuration. It can be operated in rate mode in order to measure dose rate (feedback through the resistor), or as an integrator in order to measure dose (feedback through the capacitor). Modified from [9].

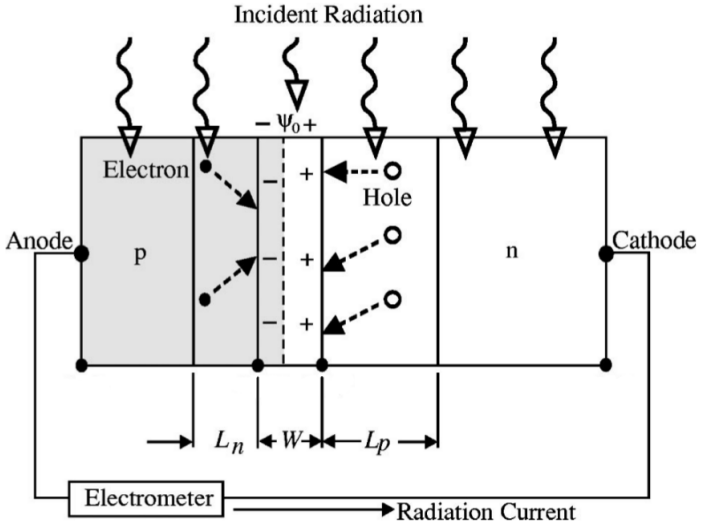

Figure 2.6: Schematic diagram of a silicon diode used as a dosimeter, in null bias mode: if the minority carriers generated by incident radiation are within diffusion length from the depletion zone, they can drift to it and be accelerated by the potential Ψ_0. L_n and L_p are the diffusion lengths for electrons and holes, respectively; W is the width of the depletion zone. Modified from [30].

accelerated by the electric field in the depletion layer towards the electrode of the opposite sign.

Silicon diodes can be operated in passive mode, i.e., without applying an external potential to the junction, or in reverse bias mode. The first is done in order to reduce leakage current due to minority carriers, but reduces as well charge collection in the dosimeter: in the absence of an electric field, the pairs that are produced outside the depletion layer must drift to it in order to be collected, and the probability of recombination is highly increased. If a reverse bias voltage is applied to the diode, however, the depletion layer is extended, and charge can be collected efficiently in a bigger volume, but the effect of increased leakage current has to be taken into account.

Diodes are especially useful when high dose gradients are present, because of their small size and good spatial resolution. However, they cannot be used for absolute measurements, since their sensitive volume depends heavily on the width of the depletion layer and is therefore very difficult to define. Their calibration needs repeated cross-checks, due to the change in sensitivity with repeated use. A temperature dependence of the response is also present. For dosimetric purposes, p-type diodes are normally chosen, since they have a much smaller leakage current and suffer less from radiation damage.

Another useful semiconductor detector, particularly because of its smaller size and better stability if compared to diodes, is the MOSFET transistor. The absorbed dose is obtained from the change in the threshold voltage due to positive ions produced in the silicon oxide by incident radiation, which are displaced towards the interface with the n-type substrate, easing the formation of the conducting channel.

2.3.3 Film dosimetry

Together with ionization chambers, films have been among the first and most widely used dosimeters. Their excellent spatial resolution and their ability to provide 2D dose maps makes their use very convenient for the determination of field profiles or when high dose gradients are present, especially if absolute dose measurements are not required.

Radiographic films consist on a thin plastic base (normally made of polyester) upon which a gelatinous solution of silver halide grains is laid. This solution can coat one or both sides of the base and is covered by a protective layer. When radiation passes through the film, ionization of the halide grains takes place, producing a latent image that needs to be developed in order to become visible and permanent.

Absorbed dose is a function of the change in optical density of the film due to irradiation. Optical density is defined as $OD = \log_{10}(I_0/I)$, where I_0 and I are the incident and transmitted light intensities, respectively. Unfortunately, the relation between optical density and absorbed dose, called *sensitometric curve*, is linear only in a limited range; therefore, it needs to be established prior to film usage. For this reason, and because it depends heavily on environmental conditions, absolute calibration of radiographic films is quite difficult. Other disadvantages are limited dose range, non tissue-equivalence, and long time needed for image processing.

As a partial solution to these drawbacks, radiochromic films have been developed. Their structure is similar to the radiographic ones (a polyester base on which an emulsion containing the radiation-sensitive crystals is laid), but their chemical composition is much more tissue-equivalent. Moreover, radiochromic films are self-developing and less dependent from ambient conditions, but are less sensitive than radiographic ones and lack spatial uniformity.

2.3.4 Luminescence dosimeters

The basic principle of luminescence dosimetry is the ability that some materials have to retain part of the energy they absorb, and then to re-emit it through time-delayed fluorescence or phosphorescence processes.

Due to the presence of impurities in the crystalline structure, electrons and holes generated by incident radiation can be excited to the so-called ‘storage traps’, metastable states

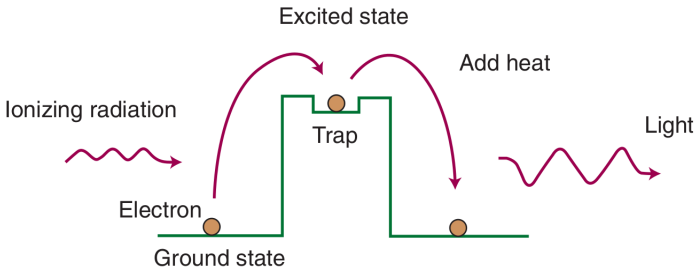

Figure 2.7: Illustration of the basic principle of thermoluminescence dosimetry. From [2].

between the conduction and valence bands. Decay from these states can be spontaneous, but for dosimetric purposes it is usually induced by heating or illuminating the crystal with a laser. In the first case, the process is known as *thermoluminescence*, in the second as *optically stimulated luminescence*. The amount of phosphorescence light emitted by the crystal can be collected by a phototube and is directly correlated with the absorbed dose.

Luminescent detectors can be made in various forms and from a variety of chemical compounds. Their dose response is linear in a wide range, and depending on their composition, they can be more or less tissue-equivalent and more or less sensitive. Before use, they have to be annealed in order to empty the traps and give a reproducible response; moreover, a careful calibration is mandatory.

2.3.5 Other kinds of dosimeters

Gel dosimetry

Gels are the only dosimeters that provide a 3D dose distribution, moreover, they are nearly tissue-equivalent and can be produced in a variety of shapes and forms. However, their response can be affected by inhomogeneities in their composition and by post-irradiation effects.

The first gel dosimeters to be developed were the Fricke dosimeters. Due to the effect of radiation, the Fe^{2+} ions dispersed in the gel are converted to Fe^{3+} ions, producing a change in the paramagnetic properties of the gel that can be measured through magnetic resonance. However, since they suffer from post-irradiation ion diffusion, they have gradually been substituted by the more stable polymer gels.

Scintillation detectors

The dose absorbed by a scintillation detector is proportional to the quantity of fluorescence light emitted when it is hit by incident charged particles. The material can be crystalline (usually NaI(Tl)) or plastic.

Plastic scintillators are especially useful for high-doses verifications, because of their stability and resistance to radiation damage. Moreover, they are tissue-equivalent, do not suffer from environmental conditions and can have excellent resolution, due to the malleability of plastic. Their major drawback is the high background noise due to Cherenkov

radiation in the light guides; to reduce this problem, the scintillator is usually coupled to two photomultipliers put in coincidence.

Diamond detectors

Diamond dosimeters are composed of a small ($1\,mm^3$) diamond crystal housed in a plastic phantom, to which a bias voltage is applied through golden electrodes. The absorbed dose is obtained from the change in resistivity due to irradiation.

Because of their small size, they have excellent spatial resolution. They are nearly tissue-equivalent and stable upon repeated irradiation. Their main disadvantages are lack of reproducibility due to pre-irradiation polarization and a temperature dependence which is not negligible.

Calorimeters

Calorimetry is of course the most fundamental way to measure the absorbed dose, since the ultimate product of all kind of particle interaction with matter is heat. The absorbed dose is obtained by measuring the temperature rise due to irradiation in a material of known mass and heat capacity. Since the change in temperature is usually very small, the use of very sensitive thermistors and accurate thermal insulation of the core are mandatory.

The use of calorimetry for dosimetric purposes is usually limited to primary standard laboratories, which employ high-sensitivity graphite or water calorimeters to obtain absolute estimations of dose used as reference for the calibration of other kind of dosimeters.

2.4 Treatment verification detectors

As it has been said in the Introduction, it is of vital importance to verify IMRT treatments plans before delivering them to the patient. Since the TPS is usually calibrated with reference fields and at 0° gantry angle, the calculation of the dose to be delivered can be inaccurate, especially in the complex case of small irregular field and large gantry angles.

Because of the intrinsic complexity of IMRT treatments, 2D field-by-field dose verification is not enough to detect clinically relevant dose errors [31], especially if it is performed only in the coronal plane and not in the axial plane, where the dose distribution depends more on the changes in anatomical structures. High-resolution dose measurements in all body planes are needed in order to obtain a 3D full-plan dose verification.

A wide variety of devices has been developed in order to address this need. Films (Sect. 2.3.3) have been widely used for 2D treatment verification, both in the coronal and axial plane [32]: their excellent spatial resolution makes them very useful for the high dose gradients of IMRT fields. However, they are not reusable, their calibration can differ from batch to batch, and most importantly, the dose distribution cannot be obtained in real time.

For these reasons, the use of films for diagnostic purposes has been nearly abandoned, and this has brought about difficulties also in their use for treatment verification purposes. They are still widely used when high-resolution dose measurements are required, however, digital solutions are generally preferred for routine QA measurements [33]. 2D arrays of high-precision ionization chambers or silicon diodes are available commercially; in addition

	MapCHECK 2 Sun Nuclear Corp.	**I'mRTMatriXX** IBA Group	**OCTAVIUS 729** PTW Freiburg GmbH
Detector type	silicon diodes	ion chamber	ion chamber
Number of detectors	1527	1020	729
Active area	$0.64\,mm^2$	$15.9\,mm^2$	$25\,mm^2$
Active volume	$0.019\,mm^3$	$79.5\,mm^3$	$125\,mm^3$
Inter-detector spacing	7.07 mm	7.62 mm	10.0 mm
Maximum field size	$32.0 \times 27.0\,cm^2$	$24.4 \times 24.4\,cm^2$	$27.0 \times 27.0\,cm^2$

Table 2.2: Technical characteristics of the most widely used commercial 2D arrays [38, 39, 40].

to field-by-field measurements, they can provide 3D dose maps by using reconstruction algorithms. However, due to the large spacing between detectors, they lack spatial resolution, and often present angular dependence. Some of these devices will be explained in more detail in Sect. 2.4.1.

The use of commercial Electronic Portal Imaging Devices (EPIDs) has also been reported as a possible way to perform pre-treatment full-plan verification [34, 35], even if complex dose reconstruction algorithms are required. EPIDs are pixelated imaging devices that are normally used to measure the exit fluence of the accelerator and the MLC positioning; they can be composed by a ionization chambers matrix, a flat panel of amorphous silicon photodiodes or a fluorescent phosphor screen imaged with a CCD camera [36]. They have a better spatial resolution than 2D detector arrays, and the additional advantage that most radiotherapy units already use them for field-by-field verification during the treatment and for patient positioning checks. However, major drawbacks are difficult calibration and the need for many different angular measurements in order to reconstruct the dose map in the patient. Further discussion on the use of EPIDs for full-plan verification can be found in [37].

2.4.1 Commercial 2D arrays

Commercial 2D arrays have been developed by private companies with the specific goal of providing both field-by-field and full plan dose verification in real time. They can be based on liquid-filled ionization chambers or silicon diodes, which can be considered point-like detectors. The response of each detector is integrated through an electrometer and then digitalized for instant readout. Interpolation and reconstruction algorithms are used in order to estimate the dose at points where no detector is present.

The most widely used commercial 2D arrays are the MapCHECK, and its successor MapCHECK 2 [38], by Sun Nuclear Corporation, I'mRT MatriXX [39] by IBA Dosimetry, and OCTAVIUS 729 [40] by PTW Freiburg GmbH. Some technical specification are summarized in Table 2.2.

Various studies [41, 42, 43, 44, 45, 46] have demonstrated that the response of these devices is linear with the dose, independent of dose rate, and highly reproducible in the short and long term. For the ionization chamber-based arrays, a relevant smoothing of dose gradients can be observed, due to the averaging of the dose in the chamber volume [42, 45]. Good agreement was found between 2D array measurements and TPS calculations both for field-by-field and composite 2D dose verification; however, periodical checks of their

performance is recommended [42]. Moreover, they are designed to obtain dose maps only in the coronal plane, and their spatial resolution is still not comparable to that of films.

2.4.2 Silicon monolithic detectors

In order to overcome the limitation of 2D commercial arrays, various prototype detectors are under development by academic institutions. Starting from the experience gained in high-energy physics, silicon detector technology has been applied to dosimetry in order to obtain a spatial resolution comparable to that of films.

Silicon has been chosen because of its high sensitivity to radiation, cheap manufacturing technology, and possibility of being operated at room temperature. Moreover, the ratio between dose in silicon and dose in water is constant in a wide range of energies. The enhanced absorption at low energies due to the photoelectric effect can be reduced by proper choice of shielding material [47].

The first monolithic 2D silicon detector was developed and tested in the framework of the European project MAESTRO (Methods and Advanced Equipment for Simulation and Treatment in Radio Oncology) [48, 49]. The first prototype was made of a $50\,\mu$m p-type epitaxial layer on which a matrix of 21×21 n-type pixels were implanted. The active area of each pixel is $2 \times 2\,$mm and the center-to-center distance is $3\,$mm. The pixels are surrounded by a common guard ring and connected to discrete readout electronics through metal strips. The detector is operated at null bias in order to minimize leakage current, and its total active area is $6.3 \times 6.3\,\mathrm{cm}^2$ [48].

Afterwards, a second prototype was built by assembling together 9 modules of the first prototype in a 3×3 matrix, thus covering an active area of $18.9 \times 18.9\,\mathrm{cm}^2$. The readout electronics for such a large number of channels is provided by ASICs chips (Application

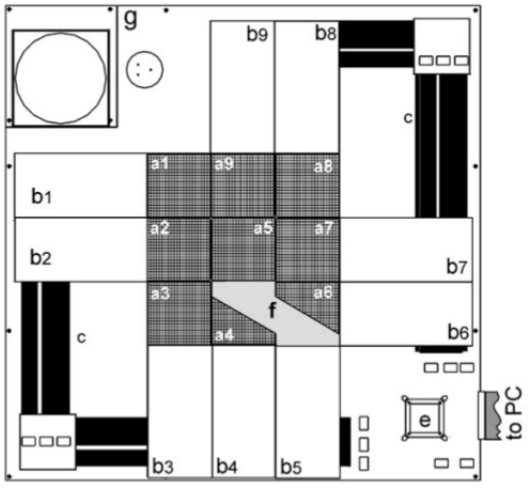

Figure 2.8: Schematic diagram of the second MAESTRO prototype (from Ref. [48]). The various building blocks can be distinguished: the silicon modules (a1–a9) to which the printed-circuit boards (b1–b9) are connected, the Kapton sheet (f) that connects the central module to its board, the common bus (c), data acquisition and electronic control system (e) and the mother board (g).

Specific Integration Circuits) built on a printed-circuit board, one for each module [48, 49]. A diagram is shown in Fig. 2.8.

Various features of these prototypes have been tested [49, 50]. Reproducibility, uniformity, linearity, and dose rate dependence were found to be below 1%. Depth dose measurements and output factor agreed with ionization chamber results, and negligible angular dependence was present.

The detector was also used to measure dose maps in the coronal plane. As expected, the spatial resolution was much higher than that of a commercial 2D array and comparable to that of films. Nevertheless, due to design decisions, dose maps cannot be measured in the axial plane.

Silicon detector technology was also applied to the development of linear arrays to be used for small field profile measurements with sub-millimetric spatial resolution. Examples are the DOSI and the Dose Magnifying Glass detectors; more details can be found in Ref. [51] and [52]. However, in many cases the integration of the detector and readout electronics on the same silicon substrate makes the density of the system very different from that of water, causing perturbations in the radiation field that make the calculation of dose-to-water quite difficult.

2.4.3 Detectors with cylindrical geometry

A first step towards dose reconstruction based on measurements not limited to the coronal plane comes from some commercial arrays in which the detectors are arranged in the volume of a cylinder. These devices have been developed with the aim of providing a rapid and effective verification of rotational IMRT plans, especially Volumetric-Modulated Arc Therapy (VMAT).

The ArcCHECK device [53] was developed by Sun Nuclear Corporation specifically for VMAT quality assurance. It consists of a hollow Polymethyl methacrylate cylinder on which 1386 diodes are arranged in a helical pattern with 1 cm pitch. Each detector has an active area of $0.8 \times 0.8\,\mathrm{mm}^3$ and is situated at a distance of 21 cm from the centre, at a depth of 2.9 cm. The helical pattern has been chosen so that the diodes do not overlap from a beam's eye view, and to increase detector density as well. An auxiliary phantom can be inserted in the 15 cm-wide central cavity in order to measure target dose.

Another device, the Delta^4 [54], was developed by the Swedish company Scandidos AB. 1069 p-type silicon diodes are arranged on two orthogonal planes in a Polymethyl methacrylate cylindrical phantom, which has a diameter of 22 cm and a length of 40 cm. Each diode is disc-shaped, with an active area of $0.78\,\mathrm{mm}^2$ and a thickness of $50\,\mu$m. The inter-detector spacing is 0.5 cm in the central $6 \times 6\,\mathrm{cm}^2$ wide square, and 1 cm in the rest of the $20 \times 20\,\mathrm{cm}^2$ total active area. The planes on which the diodes are arranged are inclined of 50° and 40° degrees with respect to the reference sagittal one. A trigger from the accelerator is used to acquire data on a pulse-by-pulse basis.

Finally, PTW Freiburg has developed a polystyrene cylindrical phantom to which the OCTAVIUS 729 ion chamber array can be coupled [55]. It has a diameter of 32 cm and can rotate synchronously to the gantry, so that the detector plane is always kept perpendicular to the beam. An inclinometer is placed on the gantry in order to preserve angular orientation. The detector is placed in the median plane of the phantom.

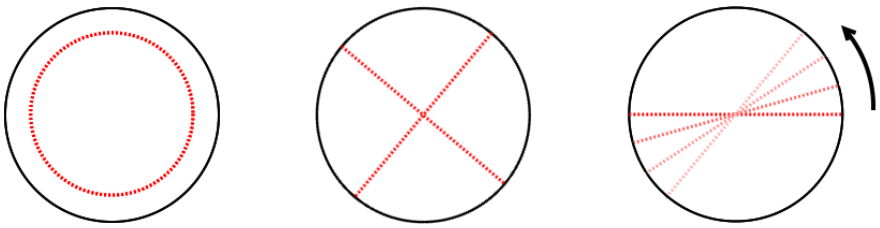

(a) ArcCHECK **(b)** Delta^4 **(c)** OCTAVIUS 4D

Figure 2.9: Diagram showing the arrangement of detectors in the ArcCHECK (a), Delta^4 (b) and OCTAVIUS 4D (c), as seen from an axial cut of the phantoms.

Basic characterization of these devices has been performed, and their suitability for quality assurance of both IMRT and VMAT plans has been established [56, 57, 58, 59]. Any significant angular or dose rate dependence has been detected and software corrections have been devised.

It can be argued if the dose maps obtained from these devices can indeed be compared [60], or if one of them performs better than the others when it comes to detect clinically relevant errors. However, it must be underlined that these devices do not measure a 3D dose distribution. The dose at points in which no detector is present is obtained through interpolation and applying the law of exponential attenuation, or, as in the case of Delta^4, by rescaling with TPS data [56]. They can certainly be considered a first attempt to measure outside of the coronal plane, but this is limited to only a few points and the reconstruction of dose maps still heavily relies on interpolation algorithms or external data.

Chapter 3

Materials and methods

As it has been said in the Introduction, the goal of the Radia2 project is to provide a complete, user-friendly tool able to perform online verification of a complex radiotherapy treatment. The materials used in the experimental setup have therefore been chosen in order to be as tissue-equivalent as possible (within the constraints of technical feasibility and cost-effectiveness), and the validation of the system follows closely the protocols for hospital quality assurance.

This chapter is divided in two parts. In the first one, the characteristics of the experimental setup are presented, discussing also the physical constraints that motivate design decisions. The measurements that have been performed in order to validate its response are also described. The second part presents the Monte Carlo simulations carried out to better understand the physical processes at play.

3.1 Detection system

The acquisition system consists of a detecting unit that can be housed in two different phantoms, coupled to discrete readout electronics controlled by a specifically developed data acquisition software.

At therapy energies, the cross-section of photons in tissue-equivalent materials is dominated by Compton scattering (see Sect. 2.1). Since the detector is quite thin, it can be assimilated to a Bragg-Gray cavity (a more detailed justification of this assertion will be given in Sect. 4.2); therefore, the dose it measures is mainly due to secondary electrons produced outside of the detecting volume. The electronic equilibrium conditions are ensured by the phantoms, which have to be thick enough to provide a secondary particle field as similar as possible to the one found in clinical conditions.

For the sensitive device, silicon monolithic detector technology was chosen, in order to obtain a high spatial resolution (see Sect. 2.4.2). Each of the segments, or strips, in which the detector is divided works as an independent diode (Sect. 2.3.2), and has its own front-end electronic chain. The spatial resolution of silicon detectors is in fact limited by the strip pitch [48, 49], and since the sensitivity of silicon is quite high (therefore, even a very small volume can produce a measurable signal), the strip pitch in turn is limited only by the maximum number of electronic channels that can be allocated, and by the increasing cost of the sensor.

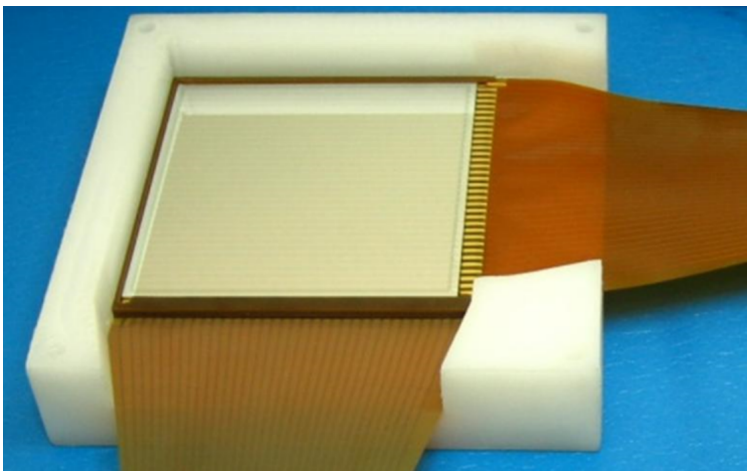

Figure 3.1: The DSSSSD placed in the protecting polyethylene box. The kapton frame, the cables and the connectors are also visible.

The first feasibility study [13] was carried out with a commercial Single-Sided Silicon Strip Detector, produced by Micron Semiconductor Ltd., with 16 strips of 3.1 mm pitch and an active area of $50 \times 50\,\mathrm{mm}^2$ (see Table 3.1). After the promising results it showed, a critical revision of the prototype was undertaken. The new setup has been designed in order to overcome the critical aspects that emerged in the first study, in particular concerning the uniformity of materials around the active area, the spatial resolution, and the response of the outer strips, which showed the need for a guard ring.

3.1.1 The detector

A photo of the Dual Single-Sided Silicon Strip Detector (DSSSSD) is shown in Fig. 3.1. It has been built by Micron Semiconductor Ltd. using two 500 μm-thick silicon wafers (serial nr. BB7-SS 2958-2 and BB7-SS 2958-6), mounted in a "back-to-back" configuration; i.e., with the ohmic sides facing each other and the junction sides facing outwards. Each wafer is made of an n-type silicon bulk, on top of which 32 p-type strips have been implanted, with 2 mm pitch. The active volume of each strip is $64 \times 2.0 \times 0.5\,\mathrm{mm}^3$, and the total active area is $64 \times 64\,\mathrm{mm}^2$ for each detector. A 0.3 μm-thick aluminium metallization allows for wire bonding. The wafers are DC-coupled; i.e., the metallization is directly laid on the p-type strips without Silicon Oxide in the middle. Around the active area, a 1.5 mm-wide guard ring is present in order to reduce edge effects and improve field uniformity in the active area.

The two detectors are mounted with the strip orientations orthogonal to one another. In the middle, a 500 μm-thin Kapton foil provides dielectric insulation (Arlon 85N polyimide laminate, developed by DuPont). This same material has been used also to build the frame of the detector, because of its scattering properties which are very similar to those of water. The frame has a thickness of 4.5 mm on the sides where the cables are connected and of 1.5 mm on the others. The thickness of the frame is 1200 μm on each side of the central Kapton layer, thus leaving a 0.7 mm air gap between each detector and the polyethylene box in which it is housed.

	W1(SS)-500	**Dual chip BB7-SS**
Number of strips	16	32 for each wafer
Strip length	49.5 mm	64 mm
Strip pitch	3.1 mm	2 mm
Wafer thickness	500 μm	500 μm
Active area	$50 \times 50\,\mathrm{mm}^2$	$64 \times 64\,\mathrm{mm}^2$
Strip active volume	$49.5 \times 3.0 \times 0.5\,\mathrm{mm}^3$	$64 \times 2.0 \times 0.5\,\mathrm{mm}^3$
Metallization	Aluminium 0.3 μm	Aluminium 0.3 μm
PCB material	FR4	Kapton
Guard ring	No	Yes

Table 3.1: Comparison between the technical characteristics of the first prototype (W1(SS)-500) and the new detection system (Dual BB7-SS).

Compared to the first prototype, the DSSSSD has a bigger active area, thus permitting the verification of larger IMRT sub-fields, and an improved tissue-equivalence of the materials surrounding it. Moreover, it has more strips and a smaller strip pitch; therefore, it can provide a better spatial resolution. A comparison between the old and the new detector can be found in Table 3.1.

The two detectors are reverse biased at a voltage $V = -50\,\mathrm{V}$, so that their active volumes are totally depleted. The bias voltage has been chosen to ensure fast charge collection without an excessive increase of leakage current. The connection to the readout electronics is provided by flat Kapton cables (50 μm-thick core made of DuPont AP8525R, with 18 μm of copper on each side), which are 20.0 cm long. In this way the copper pin connectors are kept away from the active area.

3.1.2 The phantoms

The detector has been placed in a polyethylene box measuring $108.4 \times 108.4 \times 46.1\,\mathrm{mm}^3$ in order to ensure protection from damage and an easier positioning in the two measurement setups.

Two polyethylene phantoms have been designed to house the detector and provide the necessary electronic equilibrium conditions: a slab phantom, where the detector has been placed orthogonally to the beam axis, and a cylindrical rotating phantom, where the active area of the DSSSSD is to be placed perpendicularly to the symmetry axis of the cylinder and therefore parallel to the beam axis (axial plane).

The slab phantom measures are $30.0 \times 30.0 \times 5.0\,\mathrm{cm}^3$, and it has been designed in order to characterize the dosimetric response of the DSSSSD. The active area of the detector has been centred in the phantom with millimetric precision along the x and y directions, while along the z direction the distance between the DSSSSD and the outer surfaces of the phantom are 1.5 cm and 3.2 cm. Therefore, the minimum solid water depth that can be achieved is 1.5 cm. This design decision is due to the fact that all measurements were carried out in the 6MV photon mode, and the maximum of the depth dose profile for this mode is located around a depth $d = 1.5$ cm.

The cylindrical phantom has been designed in order to simulate the body of a real patient. It is composed of three independent cylinders with a total length of 30.0 cm, and has a diameter of 20.0 cm. The central piece hosts the polyethylene box with the detector.

Figure 3.2: The slab phantom containing the DSSSSD, placed on the treatment couch at the Virgen Macarena Hospital.

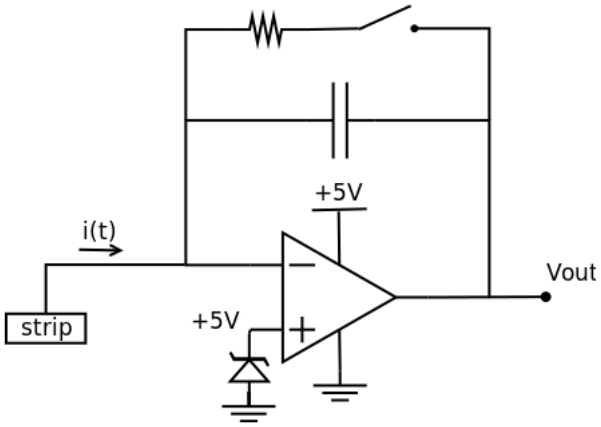

Figure 3.3: Simplified circuital diagram of the charge integrator implemented for each strip. The amplifier, the feedback capacitor, the MOSFET switch and the Zener diode are visible. The resistor in series to the switch has a low value and permits a rapid discharge of the capacitor.

The phantom can rotate around its symmetry axis by means of a software-controlled motor; the minimum rotation that can be performed is 1°. In addition, the phantom is equipped with an angular sensor in order to monitor its angular position during measurements.

3.1.3 Electronics and Data Acquisition System

The current generated in the strips by incident radiation has to be integrated in order to obtain the total induced charge, which is proportional to the absorbed dose. The front-end readout electronics has therefore been implemented as an integration circuit, composed by an operational amplifier with negative feedback through a capacitor, as can be seen in Fig. 3.3.

The capacitor can be short-circuited by means of a switch (provided by a MOSFET transistor in switch mode), thus resetting the accumulated charge. The positive pin of the amplifier is set at a reference voltage of +5 V, using a Zener diode. The output voltage $V_o(t)$ is therefore

$$V_o(t) = 5\,\mathrm{V} - V_c(t) = 5\,\mathrm{V} - \frac{1}{C}\int_0^t i_{\mathrm{in}}(t')\,\mathrm{d}t' = 5\,\mathrm{V} - \frac{q(t)}{C} \tag{3.1}$$

where $V_c(t)$ is the voltage drop across the capacitor at time t, $i_{\mathrm{in}}(t)$ is the instantaneous induced current and $q(t)$ is the total induced charge. The output voltage is therefore a linear function of the absorbed dose.

The voltage signal for each strip is then buffered to avoid charge losses and digitalized by means of 16-bit, eight-channel ADC converters (serial number ADS8568 by Texas Instruments). Since there are 64 strips, eight ADCs have been used, placed in four different boards. Each of them samples eight channels sequentially.

The data acquisition is managed by a software developed under the *LabVIEW* platform. It controls all the hardware components of the electronic chain, including the motor of the cylindrical phantom; it processes the information contained in each sample; and it is the interface which performs the acquisition-related operations like sending the trigger, resetting the capacitors and changing the sampling frequency. The measured digital values are plotted on a graph as a function of time to monitor data acquisition, and then stored in a file for offline analysis.

3.1.4 Measurements

All measurements have been carried out at the Virgen Macarena University Hospital of Seville, where two clinical accelerators are available: a Siemens PRIMUS linac, and a Siemens ONCOR one. Both have been used in the 6MV photon mode, and the fluence rate has been kept constant at 200 MU/min. Neither the gantry nor the accelerator head has been rotated in any measurement; therefore, the inplane direction (y axis) coincides with the one defined by the longitudinal axis of the treatment couch, the crossplane one (x axis) by its transversal axis. The z direction is defined by the propagation of the beam.

Some initial tests have been devised in order to study the linearity of the response of the DSSSSD, dose threshold, and the magnitude of leakage current. The reproducibility of the response has also been monitored over a three-month time period.

For the calibration, two configurations have been chosen. The first is the so-called standard configuration (source-to-surface distance of 100 cm, detector depth of 1.5 cm, square field of $10 \times 10\,\mathrm{cm}^2$): in this condition 1 MU corresponds to 1 cGy on the beam axis, by definition of Monitor Unit. The second is the so called uniformity configuration, i.e. the one in which the flattening filter of the linac is designed to produce the best profile in terms of flatness (deviations in the dose profile measured with a silicon diode are normally below 1%). For the PRIMUS linac of the Virgen Macarena University Hospital, this correspond to a source-to-surface distance of 90 cm, a depth in water of 10 cm and a $10 \times 10\,\mathrm{cm}^2$ square field.

Finally, the detector performance has been compared with the results of routine clinical tests for QA of the linac. In particular, the percent depth dose, the width of the penumbra region and the value of the output factor have been measured.

The percent depth dose (PDD) is defined as the percent ratio between the dose-to-water measured at a depth d and the one at a depth d_{ref} that corresponds to the maximum dose. It has been measured with the DSSSSD for the depths $d = 1.5$, 3.5, 5, 10 and 15 cm, and compared with data taken with a Farmer-type ionization chamber.

The penumbra is defined as the region in which the dose profile changes from 80% to 20% of the central value. Its width has been measured along the x and y directions using two rectangular fields of $5 \times 10\,\text{cm}^2$ for each detector, covering only the strips belonging to its left or right half. In this way, the penumbra profile is centered on the detector.

The output factor, defined as the dose deposited at the centre of the beam by a field of arbitrary size normalized to the one deposited by the $10 \times 10\,\text{cm}^2$ reference field, has also been measured for various square fields. This has been done in order to validate the calibration for fields much smaller than the detector active area, since in a real treatment many small field segments are present.

3.2 Monte Carlo simulations

During the first feasibility study carried out with the W1(SS)-500 detector, accurate Monte Carlo simulations were done with the GEANT4 toolkit [18, 19].

In a first phase, the entire accelerator head was simulated, including the X-ray target, the monitor chamber, the primary collimator containing the flattening filter, the two pairs of jaws that build up the secondary collimator, and the MLC, where each leaf was modelled with sub-millimetric precision. This was done both for the ONCOR and the PRIMUS linac available at Virgen Macarena University Hospital [17, 61]. The results of this simulations were stored in a set of phase spaces, one for each field size that has been computed. A *phase space* is a file that contains, for a collection of particles crossing a given plane, the particle type, position, energy, statistical weight and direction cosines of the linear momentum. The reference plane is known as *phase space plane*. A database of phase spaces of radiotherapy interest that have been experimentally validated is maintained by the International Atomic Energy Agency (IAEA, Austria) [62], with the aim of reducing the computational cost of the simulation of patient-specific treatments by eliminating the need for a detailed simulation of the radiation source (whose technical data are often protected by confidentiality).

In order to provide an interface between GEANT4 and the public methods of the IAEA phase space file format (IAEAphsp), two specific GEANT4 classes were developed [63], which are available online at [64]. One permits to write a phase space according to the IAEA format, and the other to use an IAEAphsp file as primary particle generator, thus eliminating the need for repeating the simulation of the accelerator head for every different configuration that needs to be analysed.

In the second phase, the detection system was simulated: the geometry included the detector with the 16 strips, the printed circuit board, the connector and the copper cables, placed inside the slab and the cylindrical phantoms. The phase spaces produced in the simulation of the accelerator were then used as primary particle source. The results were then compared to experimental data, showing a remarkable agreement [13, 16].

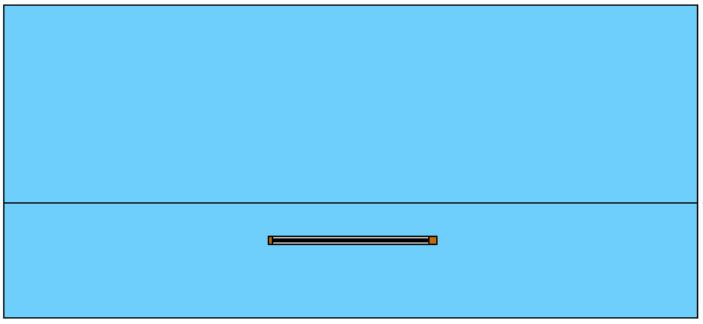

Figure 3.4: Geometrical setup defined in the GEANT4 simulation. The lower part corresponds to the slab phantom, which contains the detecting unit. The Kapton frame and the two gaps are visible. The upper rectangle represents the auxiliary solid water slabs used to achieve the desired depth; its height can be changed with a specific command in order to simulate different configurations.

3.2.1 Characteristics of the simulated setup

Fig. 3.4 shows the geometrical setup simulated for the Dual Chip BB7-SS detector[1]. It includes the slab phantom, the auxiliary solid water slabs used to obtain the necessary detector depth, and the DSSSSD with the two silicon detectors, the kapton foil in the middle, the kapton frame and the two gaps due to the different thickness of the frame compared with the detector. As primary particle source, a phase spaces was chosen corresponding to a $10 \times 10\,\mathrm{cm}^2$ field generated by a simulation of the 6MV photon mode of the Siemens ONCOR linac. It contains $4 \cdot 10^9$ independent histories, and each of them has been recycled 24 times in order to reduce the uncertainty in the final result below 1%.

The production cut has been set to $100\,\mu$m for all kinds of particles and in the whole geometry. This means that a secondary particle is explicitly followed in the simulation only if its expected range exceeds this value; if not, only the energy loss of the primary particle is considered. The physics list, which is the ensemble of physical models for the various particle interactions according to which the simulation is carried out, is based on the Standard Electromagnetic (option 4) class, which provides high accuracy electromagnetic models for relatively low energies. Models for elastic and inelastic hadronic interactions and radioactive decays are also included, although they are not relevant at these energies.

3.2.2 Analysis for different configurations

The aim of this simulation work has been to model the dose absorption in the DSSSSD, studying the influence of the different materials that surround the active area and comparing it with the dose-to-water case.

In order to do this, two different detection geometries have been considered. In the

[1] In all the figures representing the setup defined in the GEANT4 simulations, the colours are related to the different materials out of which the real detecting unit is made: water-equivalent materials (polyethylene, solid water) are shown in blue, Kapton in brown, silicon in green and air in light grey. The lighter shade of green corresponds to the sensitive volumes defined in the simulations.

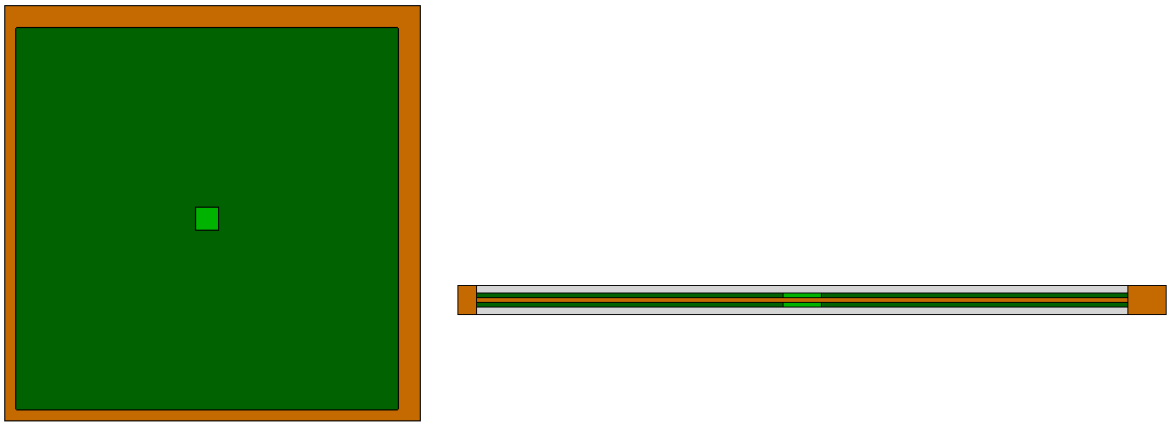

(a) xy plane **(b)** xz plane

Figure 3.5: First geometrical setup of the detecting unit implemented in the GEANT4 simulation, as seen from the positive z axis (a) and from the positive y axis (b). The sensitive volumes are the two central cavities.

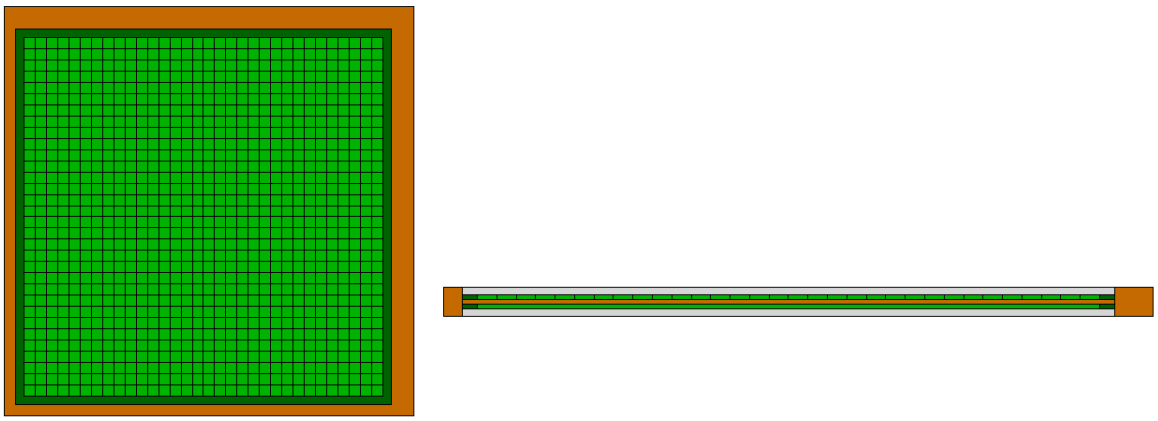

(a) xy plane **(b)** xz plane

Figure 3.6: Final geometrical setup of the detecting unit, as seen from the positive z axis (a) and from the positive y axis (b). In the latter, the width of the 32 strips of the upper detector are visible, while their length can be seen in the lower. The guard rings are also visible.

beginning, two central "pixels", or cavities, have been defined as sensitive volumes, one for each detector, measuring $4.0 \times 4.0 \times 0.5\,\mathrm{mm}^3$ (see Fig. 3.5). Several different simulations have been designed, with the aim of analysing separately the influence of the various surrounding materials (silicon, Kapton, air...) on the dose absorbed by each cavity. These simulations are described in more detail in Sect. 4.2.

Afterwards, the 64 strips have been defined as sensitive volumes (Fig. 3.6), and their

response has been studied firstly under flat-field reference conditions, and then at different solid water depths, in order to obtain a Percent Depth Dose curve. For each configuration, the two cases of dose-to-water and dose-in-silicon have been studied: in the former, the geometrical elements of the detection unit have been defined as made of water; in the latter, the real materials have been used. The results have then been compared with experimental data, both taken with the DSSSSD and with a Farmer type ionization chamber, commonly used for hospital routine checks and QA purposes.

Chapter 4

Results

As explained previously (Sect. 3.1.4), the results of measurements with the detector housed in the slab phantom are stored in a file and analysed offline. Each data file contains a matrix with n rows, one for each sample, and 66 columns: one with the sample number, one keeping track of the time passed from the trigger signal, and 64 which store the signal from each strip. The analysis has then been performed using the ROOT data analysis framework [65].

This chapter discusses the characterization of the response of the system and the results of both experimental measurements and GEANT4 simulations. In Sect. 4.1, the characterization of the response of the detector is presented, in terms of linearity, minimum dose threshold, and reproducibility over a three-month time period. The noise amplitude and the effect of leakage current are also discussed. In Sect. 4.2 the results of the GEANT4 simulations described in Sect. 3.2 are presented, while in Sect. 4.3 the calibration of the detection system is discussed. Finally, Sect. 4.4 presents the results of measurements in different configurations, and a comparison between the response of the DSSSSD and QA hospital measurements, with remarkable agreement.

4.1 Characterization of the response

For each acquisition, the output data of all 64 strips are first of all plotted against time in order to analyse their trend and compare it with the expected one. An example is shown in Fig. 4.1, where the detector is irradiated in standard conditions (SSD = 100 cm, depth $d = 1.5$ cm, field size $10 \times 10\,\mathrm{cm}^2$). In this configuration, the field size is bigger than the active area of the detector and the field profile in both the x and y directions is quite flat even if it cannot be considered strictly uniform.

Three different zones can be clearly distinguished in the spectrum:

a) the region before irradiation (time range 10 s – 35 s), where the number of counts is approximately constant;

b) the steep slope due to irradiation (time range 35 s – 95 s), where the collection of charge produces a decrease of the voltage drop across the capacitors;

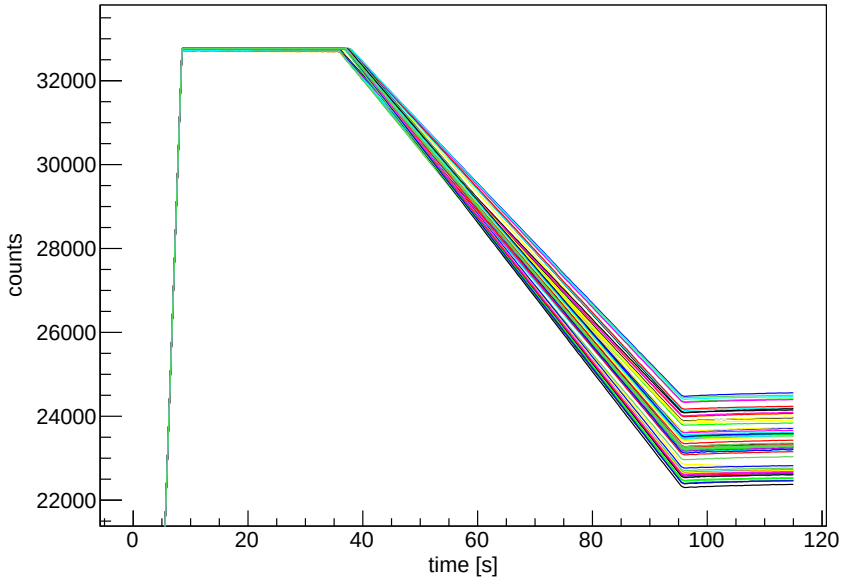

Figure 4.1: Plot of the acquired data (digital counts) against time. The irradiation conditions are the following: 200 MU, SSD = 100 cm, $d = 1.5$ cm, field size $10 \times 10\,\mathrm{cm}^2$, sampling time 500 ms.

c) the final region (time range 95 s – 115 s), where no more charge is generated and the voltage drop remains approximately constant.

However, a zoom on regions a) and c), shown in Fig. 4.2, reveals that before and after irradiation the voltage across the capacitors does not remain constant: in particular, it decreases before irradiation and increases after it, because of two different effects.

Before irradiation (Fig. 4.2a) the average number of counts remains approximately constant until $t = 15$ s, then decreases with time. The time range $9 - 15$ s corresponds therefore to the situation in which the capacitors are short-circuited, giving a constant output voltage of 5 V, while in the time range $15 - 35$ s the decrease in the number of counts due to leakage current is visible.

For each given configuration, the absorbed dose is proportional to the total fluence delivered by the accelerator. For this reason, the slope is expected to be constant during irradiation, since the fluence rate of the accelerator is kept constant at 200 MU/min and the output voltage is a linear function of the induced charge (see Eq. (3.1)), and therefore of the dose. The instants in which the irradiation begins and ends are very clearly defined in the spectrum, and are obviously the same for all the strips that are not saturated, as it can be seen in Fig. 4.2. Even in the case of a field which is uniform above the active area of the detector, the strips can have different slopes, due to the tolerances in the hardware components of the electronic chain.

Fig. 4.2a shows also that for only 14 strips out of 64 the reset value is lower than the maximum input voltage of the ADC, which is 5 V. For the others, again due to tolerances in the electronic components, the reset value exceeds the maximum 5 V and the ADC channel saturates, giving a constant output value of 32767 digital counts. A

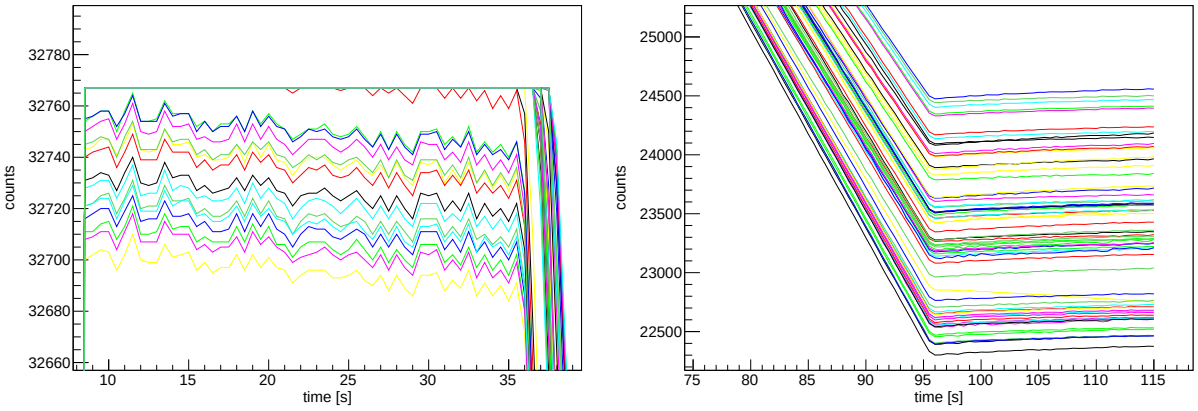

(a) Part a) **(b)** Part c)

Figure 4.2: Zoom on the initial (a) and final (b) part of the spectrum shown in Fig. 4.1, where the two effects of leakage current and dielectric absorption are visible.

board-by-board analysis shows that all the strips belonging to the T1, T3 and T4 boards are saturated, while the 14 unsaturated strips belong to T2. The remaining two strips of T2 are saturated, but their reset value is particularly close to the 5 V threshold, and a very small amount of leakage current is sufficient to desaturate them. Leakage current will be further discussed in Sect. 4.1.4.

After the irradiation (Fig. 4.2b), the voltage drop across the capacitor rises slowly. This can be explained by the dielectric absorption effect, which is quite strong in electrolytic capacitors: if the voltage drop is kept constant for a long time and then rapidly lowered, after the discharge the capacitor will reacquire a fraction of its original voltage drop, which can be as much as 15% in the case of electrolytic ones. This effect can be modelled by an exponential law and is due to the relaxation time needed by the dipoles of the dielectric medium to adapt to the new configuration, which generates a residual electric field that causes some charge to flow back on the plates.

4.1.1 Linearity

The response of each strip is expected to be linear with the absorbed dose, since it is a linear function of the collected charge, which is proportional to the dose $D(t)$:

$$V(t) = V_{\text{ref}} - \frac{q(t)}{C} = V_{\text{ref}} - \frac{1}{C}\frac{m}{W/e}D(t) \tag{4.1}$$

In this equation, which assumes the active volume of the detector to be homogeneous in density and electrical properties, m is the mass of the active volume of each strip and W/e the ionization potential of silicon. Moreover, as discussed above, for a given configuration the absorbed dose is linear with the irradiation time.

Linearity of the response of each strip has been studied for each acquisition on the raw data, before applying any calibration or correction factor. The voltage drop of each strip (in digital counts) has been fitted to a linear equation $y = mt + q$, and both the correlation

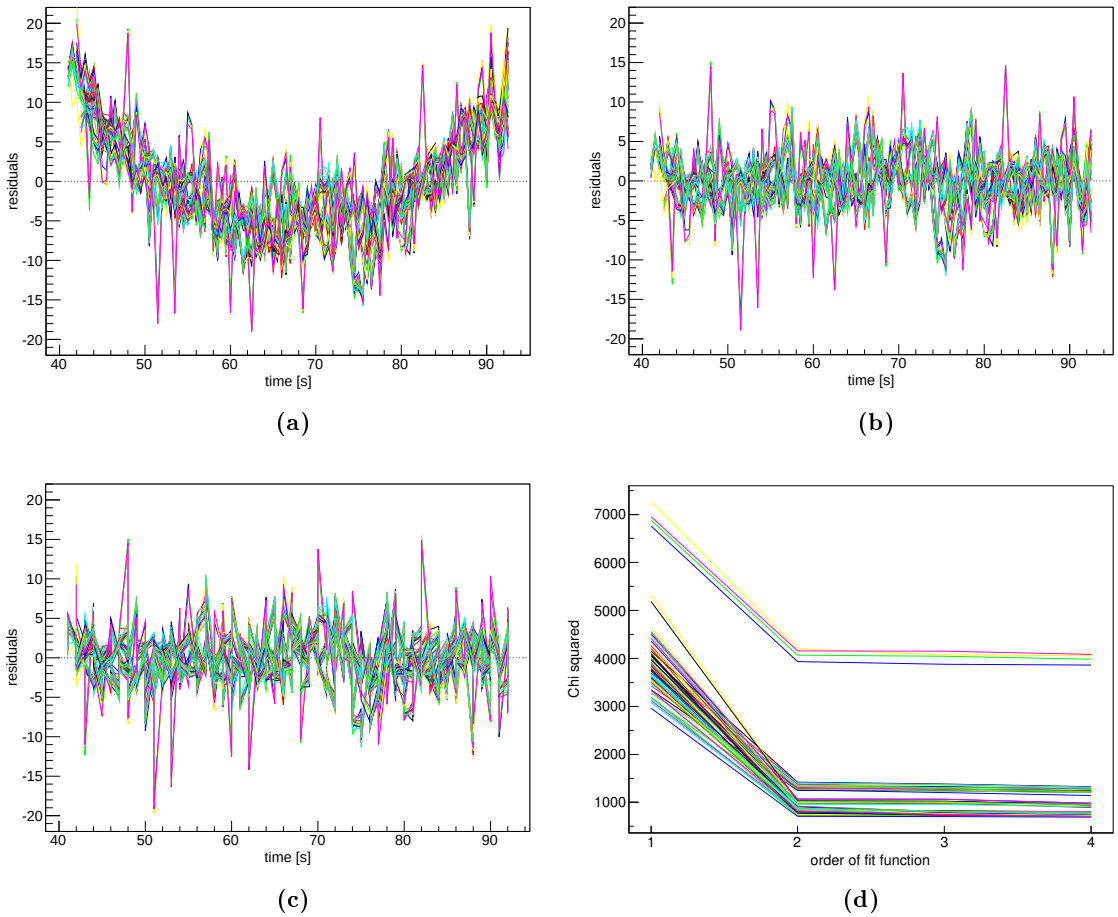

Figure 4.3: Residuals of the linear (a), quadratic (b) and cubic fit (c); values of χ^2 (d) as a function of the fit order. The irradiation conditions are the same as in Fig. 4.1: 200 MU, SSD = 100 cm, $d = 1.5$ cm, field size $10 \times 10\,\mathrm{cm}^2$, sampling time 500 ms.

coefficient and the value of χ^2 have been calculated. The residuals have also been plotted in order to study their trend: an example for one particular acquisition is shown in Fig. 4.3.

The values of the correlation coefficient show a very good linearity ($r^2 - 1 \simeq 10^{-5}$) for all strips in all measurements; however, in the residuals plot of the linear fit a parabolic trend is usually visible (Fig. 4.3a). It becomes more clear for the acquisitions that use a wider range of digital counts, while it is less visible in the ones employing a more limited range, depending strongly on the number of Monitor Units (see Table 4.1). This indicates clearly the presence of higher order terms in the transfer function of the electronic chain, due to the various non-idealities of the components, in particular of the ADC (gain and offset errors, integral non-linearity error).

For each acquisition, the data have then be fitted to a parabolic equation $y = at^2+bt+c$, whose residuals are pretty uniformly distributed around zero (Fig. 4.3b). The value of χ^2 for each strip has also been calculated: it is significantly smaller than in the linear fit case (Fig. 4.3d), showing that the addition of the second order term significantly improves

Irradiation conditions	Linear fit |m| [cts/s]	Linear fit q [cts]	Quadratic fit a [cts/s^2]	Quadratic fit |b| [cts/s]	Quadratic fit c [cts]
SSD = 100 cm d = 1.5 cm, 200 MU	143 – 178 $3 \cdot 10^{-4}$	37900 – 39300 $7 \cdot 10^{-5}$	0.02 – 0.03 $6 \cdot 10^{-2}$	146 – 182 $1.5 \cdot 10^{-3}$	38000 – 39400 $2 \cdot 10^{-4}$
SSD = 100 cm d = 1.5 cm, 100 MU	145 – 180 $6 \cdot 10^{-4}$	34000 – 34600 $7 \cdot 10^{-5}$	0.03 – 0.07 $2 \cdot 10^{-1}$	148 – 183 $4 \cdot 10^{-3}$	34000 – 34600 $2 \cdot 10^{-4}$
SSD = 100 cm d = 10 cm, 200 MU	95 – 120 $3 \cdot 10^{-4}$	36400 – 37600 $7 \cdot 10^{-5}$	0.01 – 0.03 $8 \cdot 10^{-2}$	97 – 122 $2 \cdot 10^{-3}$	36500 – 37700 $2 \cdot 10^{-4}$
SSD = 90 cm d = 10 cm, 100 MU	114 – 143 $6 \cdot 10^{-4}$	34100 – 34800 $7 \cdot 10^{-5}$	0.03 – 0.06 $3 \cdot 10^{-1}$	117 – 146 $6 \cdot 10^{-3}$	34200 – 34800 $3 \cdot 10^{-4}$

Table 4.1: Value of the parameters of the linear and quadratic fit (upper row) and their typical relative error (lower row) for different irradiation conditions. For the values, a range that takes into account the differences from strip to strip is given. For b and m, which are negative, absolute values are given.

the fit, particularly for measurements with a high number of Monitor Units. However, as reported in Table 4.1, the value of the a parameter is very small when compared b and c, and in turn b is very similar to m, thus showing that the second order term is only a small correction to the linear analysis.

As a cross-check, the data have also been fitted to a cubic equation $y = at^3+bt^2+ct+d$, with no significant changes in the residual plot (Fig. 4.3c). As expected, the obtained values of χ^2 are smaller, but quite similar to those obtained in the second order case. A cubic fit is therefore not necessary, and the second order equation approximates very well the transfer function.

It must be noted, however, that the linear and the quadratic fit provide exactly the same amount of information on the absorbed dose, which is proportional to $\Delta y = y_{\text{in}} - y_{\text{fin}}$. This assertion can be justified by applying the general expressions for the m parameter obtained with the least-square method to the particular case of experimental data which follow a parabolic curve.

By applying the least square method in the case of a linear fit, and using the bar to denote mathematical average, the m parameter is calculated as

$$m = \frac{\overline{yt} - \overline{y}\,\overline{t}}{\overline{t^2} - \overline{t}^2}$$

Then, defining $y(t) = at^2 + bt + c$, and using the linearity of the mathematical average, the following expression for m can be obtained:

$$m = \frac{\overline{yt} - \overline{y}\,\overline{t}}{\overline{t^2} - \overline{t}^2} = \frac{a\,\overline{t^3} + b\,\overline{t^2} + c\,\overline{t} - a\,\overline{t}\,\overline{t^2} - b\,\overline{t}^2 - c\,\overline{t}}{\overline{t^2} - \overline{t}^2} = b + a\left(\frac{\overline{t^3} - \overline{t}\,\overline{t^2}}{\overline{t^2} - \overline{t}^2}\right) \tag{4.2}$$

The term in brackets can be calculated by considering that the fit range is $[t_i, t_f]$:

$$\overline{t} = \frac{1}{t_f - t_i}\int_{t_i}^{t_f} t\,\mathrm{d}t = \frac{t_f^2 - t_i^2}{2(t_f - t_i)}$$

$$\overline{t^2} = \frac{1}{t_f - t_i}\int_{t_i}^{t_f} t^2\,\mathrm{d}t = \frac{t_f^3 - t_i^3}{3(t_f - t_i)}$$

$$\overline{t^3} = \frac{1}{t_f - t_i}\int_{t_i}^{t_f} t^3\,\mathrm{d}t = \frac{t_f^4 - t_i^4}{4(t_f - t_i)}$$

Substituting these expressions in Eq. (4.2) and simplifying the result the following equation for m is obtained:

$$m = b + a\,(t_i + t_f) \tag{4.3}$$

which shows that the value of $\Delta y = |m|\Delta t = \Delta t\,|b + a\,(t_i + t_f)|$ is exactly the same with the two models. As a cross-check, the linearity of the two functions $m(t_i)$ and $m(t_f)$ has been studied for the acquisition of Fig. 4.3: the correlation coefficient shows a very good linearity in both cases ($r^2 - 1 \simeq 10^{-5}$).

Therefore, in order to simplify the analysis, the absorbed dose is calculated using a linear model. The signal drop due to irradiation has been estimated as $\Delta y = |m|\Delta t$, where $\Delta t = t_f - t_i$ is the difference between the starting and ending instants of the irradiation, which can be seen clearly in the T2 board of the ADC. The uncertainty associated with the choice of t_i and t_f will be further discussed in Sect. 4.1.6.

A last remark must be made about the χ^2 values shown in Fig. 4.3d. Since the number of points in the fit is 120, the value of χ^2 is expected to be of the order 10^2, because of the characteristics of the χ^2 probability distribution. However, in Fig. 4.3d it can be seen that for all strips the values of χ^2 are ten times higher: this difference is probably due to an underestimation of the uncertainty by the fitting algorithm.

4.1.2 Reproducibility

In order to evaluate the stability in time of the acquisition system, uniformity measurements were repeated after three months. As discussed in Sect. 3.1.4, uniformity configuration is defined for the PRIMUS linac of the Virgen Macarena University Hospital as SSD = 90 cm, d = 10 cm, field size $10 \times 10\,\mathrm{cm}^2$; it has been chosen because of its particular importance for calibration purposes.

Reproducibility has been quantified as

$$\Lambda = \frac{|\Delta y_1 - \Delta y_2|}{\frac{1}{2}(\Delta y_1 + \Delta y_2)} \tag{4.4}$$

i.e., the ratio between the standard deviation of the set of measurements (calculated as the unbiased estimator $|m_1 - m_2|$) and its mean value. It has been found to be on average around 1% for all strips, with the exception of strip 12 for which it is 1.8%.

However, it must be noted that the reproducibility only quantifies the time stability of the response of the DSSSSD, therefore, it does not enter in the calculation of the uncertainty esteem for the single measurement.

4.1.3 Minimum dose threshold

As discussed previously, the reset value of the voltage for three boards out of four is higher than the nominal 5 V, which is the maximum input that can be processed by the ADCs. Therefore, at the beginning of each irradiation the strips are saturated, and a given amount of current is needed for the response to become measurable. This effect produces a threshold under which no information on the absorbed dose can be given, and which is, in

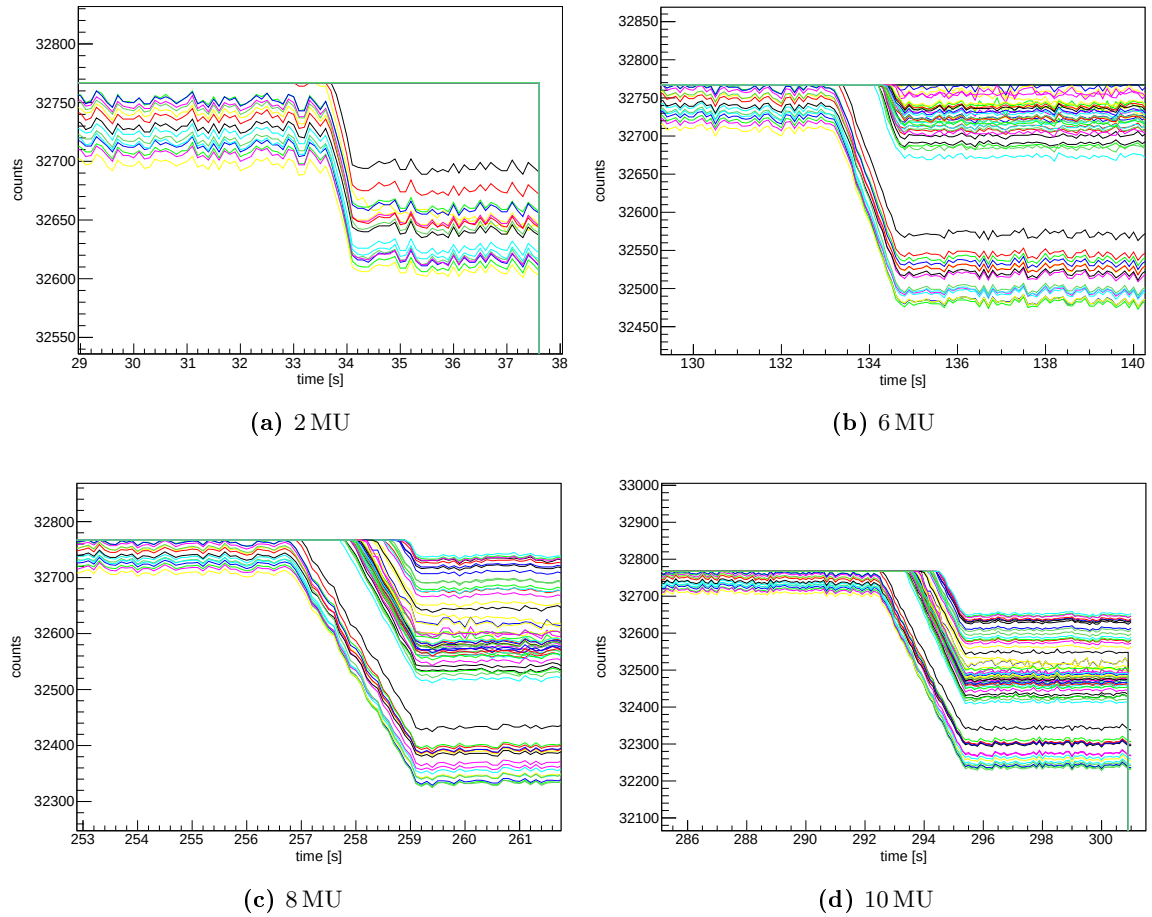

(a) 2 MU **(b)** 6 MU

(c) 8 MU **(d)** 10 MU

Figure 4.4: Spectra of some measurements with few MUs. The irradiation conditions are the following: SSD = 100 cm, $d = 1.5$ cm, field size $10 \times 10\,\mathrm{cm}^2$, sampling time 100 ms.

principle, different for each strip, although it can be seen that the strips belonging to the same board show similar behaviour. Moreover, in order to calculate correctly the absorbed dose, the strip has not only to be unsaturated, but the number of measured samples has to be high enough for the fitting algorithm to give a meaningful and reproducible result.

In order to investigate this dose threshold for each strip, measurements with few Monitor Units have been carried out. The irradiation conditions were the following: SSD = 100 cm, $d = 1.5$ cm, field size $10 \times 10\,\mathrm{cm}^2$, sampling time 100 ms; the number of MUs has been varied between 2 and 15. Some of the acquired spectra are plotted in Fig. 4.4, while Fig. 4.5 shows the response of each strip in each acquisition, calibrated with the factors of Sect. 4.3.1, where the calculation of the errors on the data is also discussed. At 2 MU, linearity in the dose delivery by the accelerator is around 2-2.5%, while it is guaranteed to be below 1% above 4 MU.

At a total fluence of 2 MU (Fig. 4.4a), only the strips belonging to T2 are unsaturated. They all measure a dose of 1.7 cGy, with a relative uncertainty of 11.3%. This comes primarily from the finite time resolution of the acquisition system: even if a 100 ms sampling

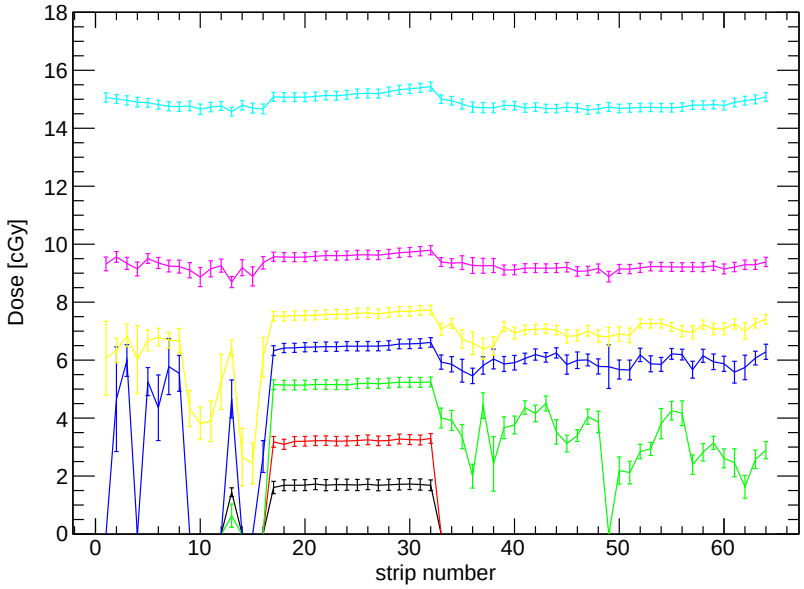

Figure 4.5: Dose measured by the strips in each acquisition with few MUs: 2 MU (black), 4 MU (red), 6 MU (green), 7 MU (blue), 8 MU (yellow), 10 MU (magenta), 15 MU (cyan). The error bars are also shown.

time has been used, the data set is composed by only five samples, and an uncertainty of one sample in both the starting and ending instants of the irradiation is relevant (see Sect. 4.1.6).

A fluence of 6 MU is enough for the strips belonging to T3 and T4 to become unsaturated (Fig. 4.4b). However, the number of samples in the fit is in most cases too little to ensure a reliable result, as can be seen in the strong fluctuation of the measured values for a field that should be considered nearly uniform. A fluence of 7 or 8 MU is therefore needed in order to obtain an acceptable result in the calculation of the dose. For the strips belonging to T1, which are still saturated at 6 MU, a fluence of 8 MU is needed in order to produce a response in all strips. However, although all the strips are unsaturated at 8 MU (Fig. 4.4c), the number of measured samples is not sufficient to produce a good result for T1. In standard conditions, the minimum fluence threshold which guarantees a reliable response for all strips is 10 MU, which corresponds to a dose threshold of (9.4 ± 0.2) cGy, as measured by the DSSSSD.

It must be noted, however, that the strips belonging to T2, which are unsaturated, give a reliable response even with a total fluence as low as 2 MU (dose threshold of 1.7 cGy), although the relative uncertainty is quite high. In order to fully exploit the measuring range of the detection system, the reset value of the voltage will be lowered for the strips belonging to T1, T3 and T4, so that it can be contained in the input range of the ADC.

Calculation of the dose threshold from the offset values

The dose threshold for the strips belonging to T1, T3 and T4 has also been calculated starting from the so-called offset values, i.e., the reset value that the ADC would output

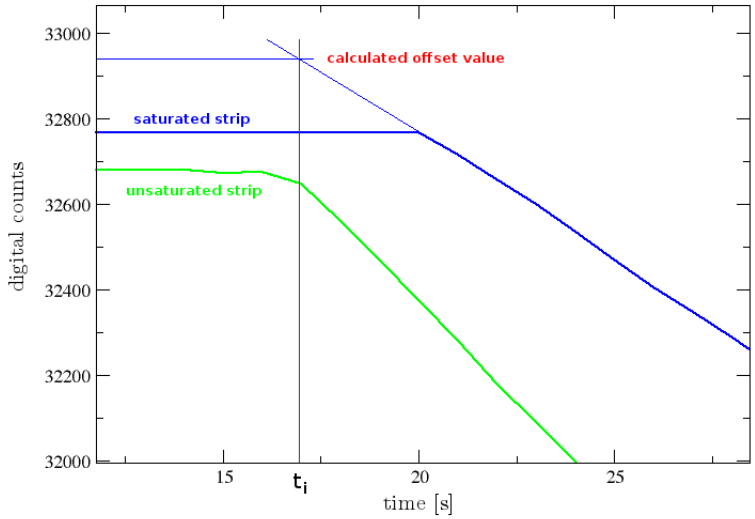

Figure 4.6: Method of calculation of the offset values for the strips of T1, T3 and T4: the starting instant t_i is shown, along with an unsaturated strip (green), a saturated one (thick blue line) and the best straight line obtained from the linear fit (superimposed thin blue line).

if it were able to digitalize a voltage greater than the maximum 5 V. These "theoretical" offset values have been calculated with the procedure exemplified in Fig. 4.6: firstly, the starting instant t_i of the irradiation is identified by analysing the change in slope of the unsaturated strips belonging to T2 (represented by the green one in the figure), then the offset value y_i^{theo} is calculated as $y_i^{\text{theo}} = mt_i + q$, where m and q are the parameters obtained from the linear fit of each saturated strip. This calculation has been repeated for 23 measurements taken in various configurations, and the resulting values have been averaged in order to obtain a more accurate estimation. The final values are reported in Table 4.2.

The dose which must be delivered in order to desaturate each strip can be calculated from the offset values by subtracting 32767 (the maximum output value of the ADC) and then expressing the result in dose by multiplying for the calibration factors defined in Sect. 4.3.1. The resulting values are reported in Table 4.2 and are consistent with what is shown in Fig. 4.5.

4.1.4 Leakage current

As it can be seen in Fig. 4.2, the effect of leakage current is clearly visible in the measured data, since the number of counts slowly decreases even before the proper irradiation begins. In order to monitor this effect, various measurements without irradiating the DSSSSD have been carried out. They all show that even if no radiation field is applied, the number of ADC counts decreases with time (fig. 4.7), with an approximate rate of 0.76 counts/s. An exception is strip 13, for which leakage current is particularly high (7.9 counts/s). This is consistent with the data provided by the manufacturer.

Leakage current introduces a systematic overestimation of the absorbed dose, independent of the particular irradiation conditions. It can be quantified in 0.02 cGy for every

Strip	Offset	Δy_i^{theo}	Dose thr.
33	32940	173	3.3 cGy
34	32930	163	3.4 cGy
35	32959	192	4.0 cGy
36	32984	217	4.5 cGy
37	32974	207	4.4 cGy
38	32988	221	4.3 cGy
39	32948	181	3.6 cGy
40	32937	170	3.5 cGy
41	32929	162	3.1 cGy
42	32927	160	3.4 cGy
43	32927	160	3.1 cGy
44	32950	183	3.6 cGy
45	32950	183	3.9 cGy
46	32966	199	3.8 cGy
47	32944	177	3.4 cGy
48	32929	162	3.4 cGy

(a) T3

Strip	Offset	Δy_i^{theo}	Dose thr.
49	32996	229	4.8 cGy
50	32974	207	4.0 cGy
51	32953	186	3.9 cGy
52	32938	171	3.6 cGy
53	32937	170	3.6 cGy
54	32937	170	3.3 cGy
55	32908	141	2.7 cGy
56	32921	154	2.9 cGy
57	32973	206	4.0 cGy
58	32961	194	3.8 cGy
59	32957	190	3.7 cGy
60	32972	205	3.9 cGy
61	32980	213	4.2 cGy
62	32991	224	4.4 cGy
63	32946	179	3.9 cGy
64	32943	176	3.7 cGy

(b) T4

Strip	Offset	Δy_i^{theo}	Dose thr.
1	33045	278	6.4 cGy
2	33033	266	5.7 cGy
3	33047	280	5.8 cGy
4	33039	272	6.5 cGy
5	32989	222	5.0 cGy
6	33015	248	5.4 cGy
7	33007	240	5.5 cGy
8	33010	243	5.8 cGy
9	33093	326	6.8 cGy
10	33060	293	6.7 cGy
11	33058	291	6.8 cGy
12	33063	296	6.3 cGy
13	32954	187	4.0 cGy
14	33047	280	6.5 cGy
15	33058	291	6.8 cGy
16	33046	279	6.0 cGy

(c) T1

Table 4.2: Offset values and calculated dose threshold for each strip.

second of irradiation, which means 0.5 cGy every 100 MU of fluence (the fluence rate of the accelerator is 200 MU/min). For strip 13, the overestimation is 4.8 cGy every 100 MU. The relative importance of leakage current decreases with increasing dose rate, therefore it can usually be neglected for measurements of percent depth dose and in standard and uniformity conditions, while it biases slightly the penumbra and output factor measurements.

The value of 0.02 cGy/s for the overestimation due to leakage current has been calculated using only data for the strips belonging to T2: for the other strips, which are saturated, a direct measurement of leakage current would require an excessive amount of time. The same value as for the strips of T2 has therefore be assumed: this assumption is justified by the data provided by the manufacturer, which measured a similar value of leakage current for all strips but strip 13.

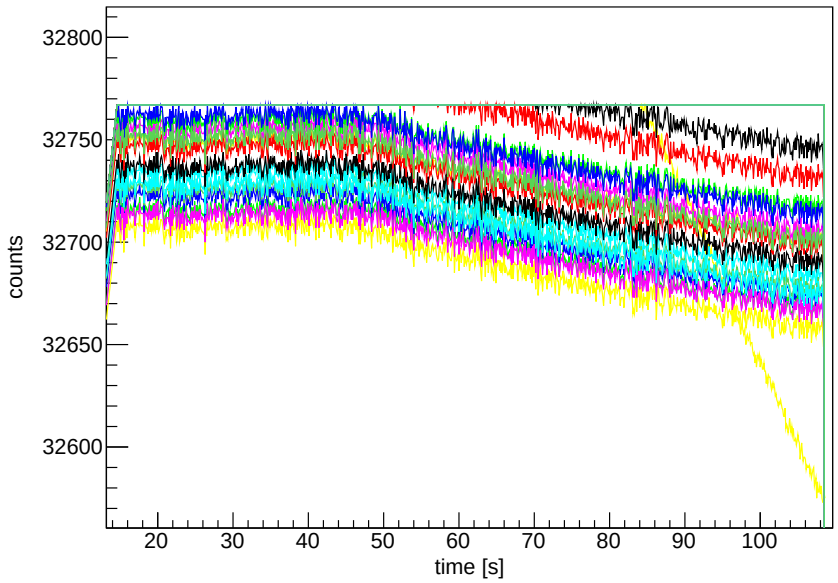

Figure 4.7: Spectrum of a no irradiation measurement, sampling time 100 ms. The capacitor was kept short-circuited more or less for the first 30 seconds; after this point, the decrease due to leakage current is clearly visible. Strip 13 is the yellow one with the steepest slope.

4.1.5 Noise

The amplitude of noise has also been studied for the DSSSSD. Each of the measured points is the sum of a contribution due to signal and a fluctuation due to noise: in order to study the amplitude of the latter, an accurate modelization of the former is mandatory. Then, once the signal has been subtracted, the remaining fluctuation is only due to noise.

The mathematical function used to describe the signal is of course different for each of the three regions of the spectrum described at the beginning of Sect. 4.1. Before irradiation, the variation in the number of counts is only due to leakage current, which can be assumed to be constant; therefore, the signal has been modelled as a linear function. As discussed in Sect. 4.1.1, the analysis of χ^2 shows that during irradiation the signal is accurately described by a polynomial of order 2; while after irradiation the effect of dielectric absorption has to be taken into account. The most accurate description of this effect would be obtained by means of an exponential function; however, in order to simplify the analysis, another function of order 2 has been used. The values of χ^2 obtained from the fit show that such a function can model dielectric absorption in a satisfactory way.

The noise amplitude has then been calculated as the standard deviation of the values obtained by subtracting the signal (modelized by the three functions just described) to the measured data. This has been repeated for 28 measurements taken with a sampling time of 500 ms, and for 5 measurements taken at 100 ms; an average value of noise for each strip has been calculated in both cases.

A plot of the noise amplitude for each sample is shown in Fig. 4.8, in which each colour represents one board of the ADC: the fluctuation trend is clearly very similar for the strips

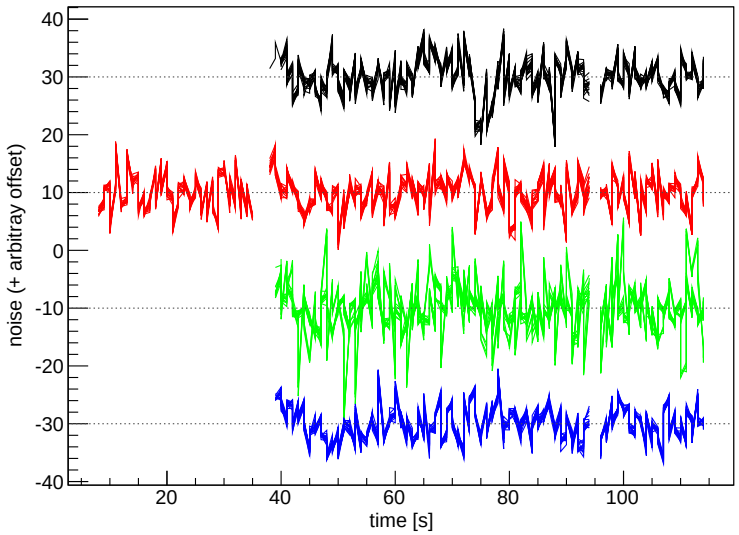

Figure 4.8: Noise contribution to the measured points, as resulting from the subtraction of signal to the measured data. The strips belonging to the same ADC board are plotted in the same colour, and an arbitrary offset, different for each board, is added. The sampling time is 500 ms.

Sampling time	T1	T2	T3	T3 (str 35 to 38)	T4
500 ms	2.6	3.4	2.7	6.3	2.6
100 ms	2.6	3.6	2.7	6.6	2.7

Table 4.3: Average values of the noise amplitude for each board at different sampling times.

belonging to the same board, hinting at the fact that in our system the main source of noise is the ADC converter. This is confirmed by the average offset values calculated for each strip, which are the same, within a 4%, for the strips belonging to the same board, with the exception of four consecutive strips of T3, which present a higher noise (but similar among the four of them).

The amplitude of noise is reported for each board in Table 4.3: T2 presents a particularly high value, both at 100 ms and at 500 ms, which could be explained by the fact that the reset value of the voltage is lower. At 100 ms some of the boards (T2, T4 and strips 35 to 38 of T3) present a higher noise than at 500 ms, but this behaviour is not common to all boards.

4.1.6 Uncertainty estimation

As explained in Sect. 4.1.1, the signal drop due to irradiation (which is proportional to the absorbed dose) has been calculated for each strip as $\Delta y = |m|\Delta t$, where m is the slope obtained from the linear fit of the data and $\Delta t = t_f - t_i$ is the time interval in which the irradiation takes place. The uncertainty on the number of counts Δy is therefore the sum in quadrature of two uncertainty contributions, one on the slope and one due to the

finite time resolution of the system. By applying the law of uncertainty propagation the following equation is obtained:

$$\sigma_{\Delta y} = \Delta y \sqrt{\left(\frac{\sigma_m}{m}\right)^2 + \left(\frac{\sigma_{\Delta t}}{\Delta t}\right)^2} \tag{4.5}$$

where the two contributions of m and Δt are visible.

The value of $\sigma_{\Delta t}$ is directly correlated with the sampling time δt of the digitalization process: a higher sampling rate permits a more accurate identification of the starting and ending instants of the irradiation, and therefore a better estimation of Δt. t_i and t_f are both chosen among the set of samples as the ones at which the slope of the data changes substantially, marking a variation of the physical conditions (presence or absence of the radiation field). However, the 'real' starting instant t_i^* can happen at any time between one sample and the next, and the same can be said for the ending one. t_i^* and t_f^* are therefore distributed with uniform probability in an interval of amplitude δt, where δt is the sampling time. The maximum uncertainty on t_i and t_f is $\delta t/2$, or half a sample, and the typical one can be calculated using the properties of the uniform probability distribution defined in the range $[-\delta t/2, \delta t/2]$, whose expected value $\mathrm{E}(t)$ (first moment) is 0. The variance $\mathrm{Var}(t)$ of the distribution is

$$\mathrm{Var}(t) = \mathrm{E}[(t - \mathrm{E}(t))^2] = \mathrm{E}(t^2) = \int_{-\delta t/2}^{\delta t/2} t^2 \, \frac{1}{\delta t} \, \mathrm{d}t \; = \; \frac{\delta t^2}{12}$$

and the typical statistical error can be calculated as $\mathrm{StDev}(t) = \sqrt{\mathrm{Var}(t)} = 0.29\,\delta t$. The value of $\sigma_{\Delta t}$ is therefore

$$\sigma_{\Delta t} = \sqrt{\sigma_{t_i}^2 + \sigma_{t_f}^2} = \sqrt{2} \cdot 0.29\,\delta t \tag{4.6}$$

The physical sources of uncertainty in the calculation of the irradiation slope are conceptually more difficult to identify. Because of the small amplitude of the fluctuation due to noise, the contribution to the uncertainty on m that arises from the dispersion of the measured data is small. The only exception are the measurements with few Monitor Units, for which the relative importance of noise is of course much higher (5% at 2 MU, between 0.4% and 1% at 15 MU). For measurements with 100 or 200 MU, the fitting algorithm always gives an estimation of the relative uncertainty on the slope below 0.1% (some typical values are reported in Table 4.4). However, if an acquisition in specific conditions is repeated many times and the standard deviation of the values of m is calculated, it can be seen that it is quite higher than the uncertainty calculated by the fitting algorithm, as shown in Table 4.4.

The uncertainty on the slope σ_m has therefore been calculated in a different way in the two cases of few or many Monitor Units:

- for measurements with few Monitor Units, the uncertainty due to noise has been assumed to be the most relevant contribution. Because of this, the value of σ_m is the one calculated by the fitting algorithm, which quantifies the dispersion of the measured data.

- for measurements with 100 or 200 MU, the uncertainty due to noise is negligible if compared with the standard deviation of repeated measurements. The latter has then been assumed as the average uncertainty on the slope.

Configuration	Nr of measurements	$\sigma_{\mathbf{m}}^{\mathrm{fit}}/\mathbf{m}$	StDev(m)/m
$90 + 10$, 100 MU	5	0.08%	0.22%
$100 + 1.5$, 100 MU	7	0.07%	0.37%
$100 + 1.5$, 200 MU	3	0.03%	0.15%
$100 + 10$, 200 MU	3	0.05%	0.31%

Table 4.4: Average relative uncertainty on m as calculated by the fitting algorithm and relative standard deviation in the values of m for repeated measurements, for different configurations. In the first column, the first number is the SSD, the second is the depth of solid water above the detector; both are expressed in centimeters. The field size is in all cases $10 \times 10\,\mathrm{cm}^2$.

Strip	$\sigma_{\mathbf{m}}$	Strip	$\sigma_{\mathbf{m}}$	Strip	$\sigma_{\mathbf{m}}$	Strip	$\sigma_{\mathbf{m}}$
1	0.4	17	0.6	33	0.7	49	0.6
2	0.5	18	0.6	34	0.6	50	0.7
3	0.5	19	0.6	35	0.6	51	0.6
4	0.5	20	0.6	36	0.6	52	0.6
5	0.5	21	0.6	37	0.6	53	0.6
6	0.5	22	0.7	38	0.7	54	0.6
7	0.5	23	0.7	39	0.7	55	0.6
8	0.5	24	0.7	40	0.7	56	0.6
9	0.6	25	0.7	41	0.7	57	0.6
10	0.5	26	0.6	42	0.7	58	0.6
11	0.5	27	0.6	43	0.7	59	0.6
12	0.5	28	0.6	44	0.6	60	0.6
13	0.6	29	0.6	45	0.6	61	0.6
14	0.6	30	0.6	46	0.6	62	0.6
15	0.5	31	0.6	47	0.6	63	0.6
16	0.6	32	0.6	48	0.6	64	0.6
(a) T1		**(b)** T2		**(c)** T3		**(d)** T4	

Table 4.5: Uncertainty on the slope (in counts/s) which is assumed for each strip for all measurements but the uniformity ones.

However, some measurements have only been taken once, and others were repeated a different number of times. In order to ensure that the estimation of the standard deviation from such small sets is reliable, different subsets of the set of 7 measurements with 100 MU, SSD = 100 cm and $d = 1.5$ cm have been analysed: a minimum number of five repetitions is needed to provide a reliable estimation. Therefore, for the measurements in configuration of uniformity, which have been repeated five times, σ_m has been calculated as the standard deviation of that same set of five measurements; for all the others the uncertainties reported in Table 4.5 are assumed, which are calculated for each strip from the set of seven measurements in standard conditions described above.

4.2 GEANT4 analysis

As discussed in Sect. 3.2.2, the aim of the Monte Carlo simulations that have been carried out is to analyse the influence of the different materials that surround the active area of the DSSSSD. The main issues under consideration were the effect on the absorbed dose of

Sim.	Upper det.	Upper cav.	Central layer	Lower det.	Lower cav.	Gaps	Frame
0A	water	water	water	water	water	water	water
0B	water	water	water	water	water	air	water
1A	silicon	silicon	water	water	water	air	water
1B	water	water	water	silicon	silicon	air	water
1C	silicon	silicon	water	silicon	silicon	air	water
1D	silicon	silicon	Kapton	silicon	silicon	air	water
1E	water	water	Kapton	silicon	silicon	air	water
1F	water	water	Kapton	water	water	air	water
2	silicon	silicon	Kapton	silicon	silicon	air	Kapton
Ext	water	silicon	water	water	silicon	water	water

Table 4.6: Description of the various simulation that have been designed in order to study the influence of the different materials on the absorbed dose.

	Upper cavity		Lower cavity	
Sim.	Dose [cGy/hist]	Rel. uncertainty	Dose [cGy/hist]	Rel. uncertainty
0A	$1.08 \cdot 10^{-14}$	0.8%	$1.08 \cdot 10^{-14}$	0.8%
0B	$1.08 \cdot 10^{-14}$	0.8%	$1.07 \cdot 10^{-14}$	0.8%
1A	$1.00 \cdot 10^{-14}$	0.7%	$1.06 \cdot 10^{-14}$	0.8%
1B	$1.14 \cdot 10^{-14}$	0.7%	$1.00 \cdot 10^{-14}$	0.7%
1C	$1.05 \cdot 10^{-14}$	0.7%	$0.98 \cdot 10^{-14}$	0.8%
1D	$1.04 \cdot 10^{-14}$	0.7%	$0.97 \cdot 10^{-14}$	0.8%
1E	$1.12 \cdot 10^{-14}$	0.8%	$1.01 \cdot 10^{-14}$	0.7%
1F	$1.08 \cdot 10^{-14}$	0.8%	$1.07 \cdot 10^{-14}$	0.8%
2	$1.03 \cdot 10^{-14}$	0.7%	$0.98 \cdot 10^{-14}$	0.8%
Ext	$1.01 \cdot 10^{-14}$	0.8%	$0.94 \cdot 10^{-14}$	0.8%

Table 4.7: Calculated absorbed dose in the simulations with two central cavities. The relative uncertainty (1σ) is also reported.

the two air gaps between the DSSSSD and the phantom, the validity of the assumption of water-equivalence for the scattering properties of Kapton and the assessment of the difference in the response of the two detectors due to the depth shift between them. The latter is particularly important for calibration purposes.

4.2.1 Dose deposition in two central "cavities"

In the first set of GEANT4 simulations two central pixels, called cavities in analogy to cavity theory, have been defined as sensitive volumes. Different materials have been assigned to the various geometrical elements of the simulated setup, and the dose deposition per history in each cavity has been calculated. The materials defined in each of the eight simulations carried out are summarized in Table 4.6, while the resulting dose per history and relative uncertainty are reported in Table 4.7. As expected, the statistics is high enough to reduce the relative uncertainty below 1%.

From the combined analysis of Table 4.6 and 4.7, much insight on the physical processes at play can be gained:

- **Effect of the air gaps (sim. 0A/0B):** the upper cavity measures the same amount

of dose in the two cases, showing that the upper air gap does not alter the particle field significantly. In the lower cavity a negligible (below 1σ) decrease in the amount of dose is seen.

- **Water-equivalence of Kapton (sim. 1F/0B and 1C/1D/2):** the presence of the Kapton frame does not alter the dose calculated by the cavities (sim. 1D/2), and neither does the central layer if no silicon is present (sim. 1F/0B). However, if the two layers of silicon are inserted (sim 1D/1C and 2/1C), differences of 1.6σ and 1.8σ can be seen in the dose obtained in the upper cavity. This could be due to a decrease of backscattered radiation at the interface between the central layer and the lower silicon one, since the difference in density between Kapton and silicon is lower than the one between silicon and water ($\rho_{\text{Kap}} = 1.6\,\text{g/cm}^3$, $\rho_{\text{Si}} = 2.3\,\text{g/cm}^3$). Nevertheless, despite its higher density, the water-equivalence of Kapton can be considered good.

- **Dose-in-silicon vs dose-in-water (sim. 1A/0B and 1B/0B):** in both cases, the dose obtained in silicon is lower than that in water. This is a general result that is valid both for small and large cavities, and it can be understood by considering the physical processes at play. For small cavities, the dose is proportional to the mass stopping power, which in turn is proportional to Z/A (where Z is the atomic number and A is the atomic mass), according to the Bethe-Bloch formula. For large cavities, the absorbed energy is proportional to the Compton cross-section of the material, which in first approximation depends linearly on Z: the absorbed dose depends therefore on the ratio Z/ρ. In both cases, the expected ratio $D_{\text{H}_2\text{O}}/D_{\text{Si}}$ is higher than 1.
  The presence of silicon in one of the two detecting layers also influences the dose calculated by the cavity belonging to the other: the dose deposited in water by the upper cavity is higher if silicon is present in the lower layer, due to an increase of backscattering; while the presence of silicon in the upper one modifies the charged particle field, producing a decrease in the dose absorbed by the lower cavity.

- **Difference in the depth of the two detectors (sim. 1A/1B):** the dose absorbed by the silicon-filled cavity is the same in the two cases, showing that the difference in depth of the two detecting layers can be neglected. For what concerns the other cavity, the same effects described before take place: the dose is increased in the upper cavity and decreased in the lower one by the presence of silicon in the other detecting layer.

- **"Shading effect" of the upper detector on the lower one (sim. 1B/1C, 1D/1E and 1C/0B, Ext/0A):** if silicon is present in the upper cavity, the dose-in-silicon calculated in the lower one does not remain the same, but significantly decreases. This is confirmed by the comparison of the simulations 1C/0B and Ext/0A: in both cases the decrease in the dose absorbed by the lower cavity is much higher than the one in the upper, and cannot be ascribed only to the different molecular properties of silicon and water. It is also independent from the materials surrounding the detecting cavities: a comparison between the simulations Ext and 1C shows a similar change in both cavities, due to a decrease of laterally scattered particles. Therefore, the presence of a silicon layer above the lower one significantly alters

the charged particle spectrum, giving rise to the so-called "shading effect", whose identification is essential for a correct calibration of the DSSSSD.

- **Effect of the lower detector on the upper one (sim. 1A/1C):** as discussed previously, the presence of silicon in the lower layer significantly increases the amount of backscattering at the interface between the central layer and the lower detecting one, giving rise to an increase of the dose absorbed by the upper cavity.

Because of what has been just discussed, it is clear that the interplay between the two silicon detecting layers of the DSSSSD is complex and that the response of each layer is strongly affected by the presence of the other. Moreover, the comparison between sim. 2 and 0A shows clearly that the difference in the dose absorbed by the two sensitive layers of the DSSSSD is due to a perturbation induced from the dosimeter on itself, and is not related to the process of dose deposition in water. Therefore a single reading for the two detectors has been given for all configurations, as it will be further discussed in the next section.

4.2.2 Dose deposition in each strip

In the second set of simulations the 64 strips have been defined as sensitive volumes, and the dose per history deposited in each one has been calculated. Uniformity and standard configuration have been studied. Moreover, the depth in water of the simulated DSSSSD has been changed while keeping constant the SSD at 100 cm and the field size at $10\times10\,\mathrm{cm}^2$, to reconstruct the Percent Depth Dose curve and compare it with real measurements, in order to validate the results of the simulations. A comparison between the simulated PDD curve and experimental ones, both taken with the DSSSSD and with a Farmer-type ionization chamber, is shown in Sect. 4.4.1. It must be noted that in this second set of simulations the relative uncertainty is lower than in the previous one, since the sensitive volumes defined in the geometry are bigger.

Fig. 4.9 shows the dose absorbed per history by each strip of both detectors in three different irradiation conditions: uniformity (SSD = 90 cm, depth d = 10 cm), standard (SSD = 100 cm, depth d = 1.5 cm) and SSD = 100 cm, depth d = 10 cm. A $10\times10\,\mathrm{cm}^2$ square radiation field was defined in all cases. They confirm what was deduced in the previous section from the simulations with two central cavities: a significant difference in the dose absorbed by the upper and lower silicon layers is present, which cannot be seen in the dose-in-water case. Its average value is of the order of 6%, and is reported in Table 4.8 for each of the simulations carried out; in first approximation it does not depend on the particular configuration which is considered.

Due to this shading effect, a single reading for the two detector must be given, because the difference in their response is caused by the perturbation produced within the measuring device, and is not a physical effect that takes place in the dose-to-water case.

4.3 Calibration

After the detailed analysis of the response of the DSSSSD and of the GEANT4 simulations described in the previous sections, each of the 64 strips has to be calibrated in order to

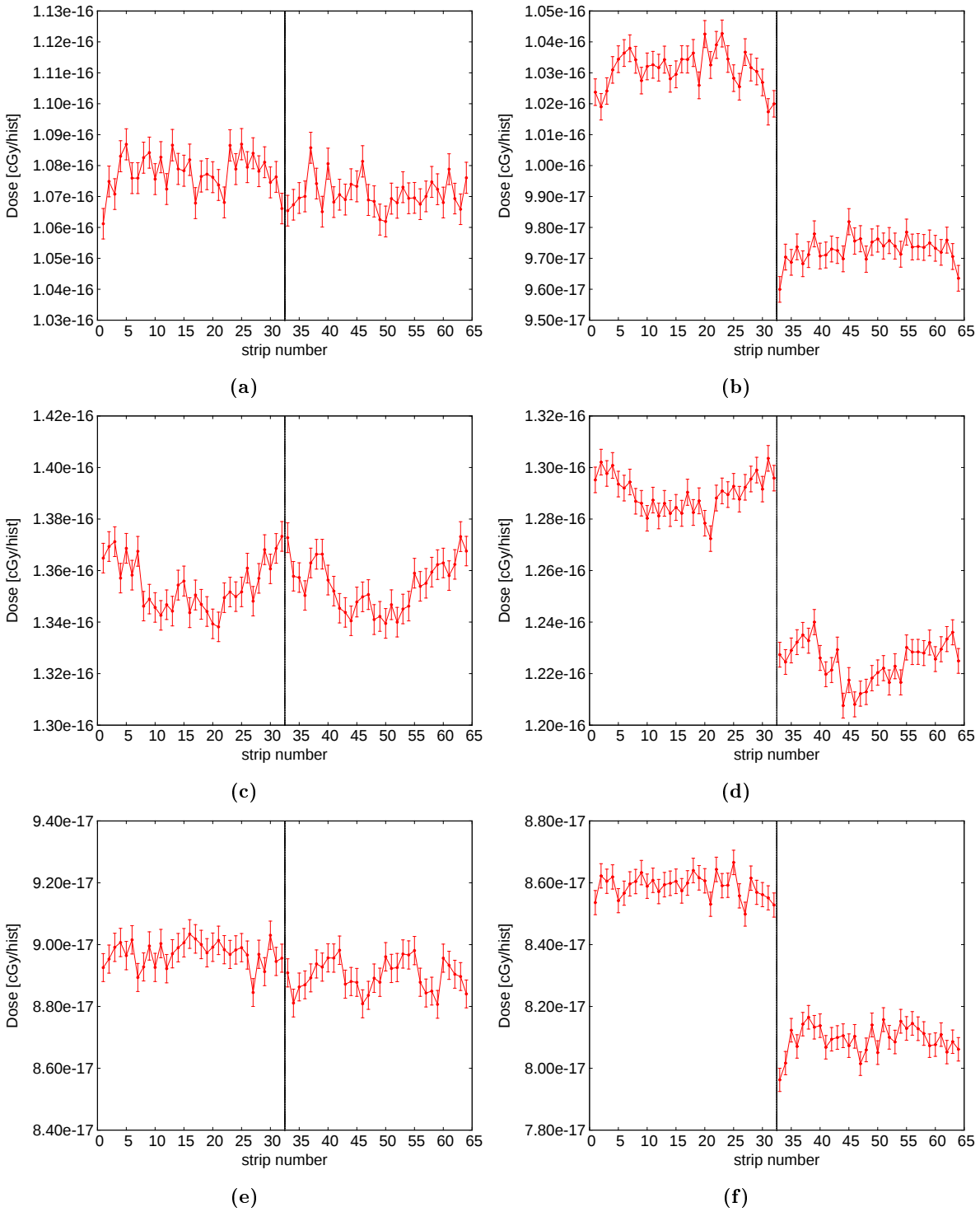

Figure 4.9: Dose per history calculated for each of the 64 strips in various configurations: uniformity conditions, dose in water (a) and in silicon (b); standard conditions, dose in water (c) and in silicon (d); SSD = 100 cm, $d = 10$ cm, field size $10 \times 10\,\mathrm{cm}^2$, dose in water (e) and in silicon (f).

Configuration	Upper detector Dose [cGy/hist]	Rel. unc.	Lower detector Dose [cGy/hist]	Rel. unc.	Diff.
Uniformity	$1.08 \cdot 10^{-16}$	0.5%	$1.07 \cdot 10^{-16}$	0.5%	0.63%
PDD 15 mm	$1.35 \cdot 10^{-16}$	0.4%	$1.35 \cdot 10^{-16}$	0.4%	0.02%
PDD 35 mm	$1.25 \cdot 10^{-16}$	0.4%	$1.25 \cdot 10^{-16}$	0.4%	0.44%
PDD 50 mm	$1.16 \cdot 10^{-16}$	0.5%	$1.16 \cdot 10^{-16}$	0.5%	0.46%
PDD 100 mm	$8.97 \cdot 10^{-17}$	0.5%	$8.90 \cdot 10^{-17}$	0.5%	0.80%
PDD 150 mm	$6.82 \cdot 10^{-17}$	0.6%	$6.78 \cdot 10^{-17}$	0.6%	0.52%

(a) Dose in water

Configuration	Upper detector Dose [cGy/hist]	Rel. unc.	Lower detector Dose [cGy/hist]	Rel. unc.	Diff.
Uniformity	$1.03 \cdot 10^{-16}$	0.4%	$9.73 \cdot 10^{-17}$	0.4%	5.8%
PDD 15 mm	$1.29 \cdot 10^{-16}$	0.4%	$1.22 \cdot 10^{-16}$	0.4%	5.2%
PDD 35 mm	$1.20 \cdot 10^{-16}$	0.4%	$1.13 \cdot 10^{-16}$	0.4%	5.7%
PDD 50 mm	$1.11 \cdot 10^{-16}$	0.4%	$1.05 \cdot 10^{-16}$	0.4%	5.6%
PDD 100 mm	$8.59 \cdot 10^{-17}$	0.5%	$8.09 \cdot 10^{-17}$	0.5%	5.9%
PDD 150 mm	$6.55 \cdot 10^{-17}$	0.5%	$6.18 \cdot 10^{-17}$	0.5%	5.7%

(b) Dose in silicon

Table 4.8: Average calculated dose per history in each of the two detectors, and statistical relative uncertainty (1σ), in each of the different configurations that have been simulated. The percent difference between the average values in the upper and lower detector is also given.

obtain the dose absorbed in each measurement. As discussed in Sect. 4.2, a single detection depth is assigned to the two silicon layers, and no distinction is made between the strips belonging to one or the other.

Calibration has been carried out in uniformity conditions, in which the radiation field produced by the accelerator can be considered uniform; the variations in the response of the strips are therefore due only to the tolerances in the hardware components of the electronic chain and not to real differences in the amount of absorbed dose. As a cross-check, the calibration factors have been calculated also from measurements in standard conditions, and a comparison between the two has been carried out. However, in this case the calibration procedure is more complex, and these calibration factors have not been used for actual estimations of absorbed dose.

4.3.1 Calibration in uniformity conditions

In uniformity conditions, which for the PRIMUS linac of the Virgen Macarena University Hospital correspond to a source-to-surface distance of 90 cm, a depth d in water of 10 cm and a field size of $10 \times 10\,\mathrm{cm}^2$, the field produced by the accelerator is flat. Each strip of the DSSSSD should therefore measure the same amount of dose D_{unif}, namely 0.81 cGy/UM, according to routine QA measurements carried out at the hospital.

All uniformity measurements have been done with a total fluence of 100 UM. The calibration factor has therefore been calculated for each strip as

$$F_i^{\mathrm{cal}} = \frac{D_{\mathrm{unif}}}{\Delta y_i^{\mathrm{unif}}} = \frac{81\,\mathrm{cGy}}{-(m_i - m_{\mathrm{leak}}, i)\,\Delta t} \tag{4.7}$$

Strip	F_{cal}[cGy/cts]	$\sigma_{F_{cal}}$[cGy/cts]
1	0.02319	$8 \cdot 10^{-5}$
2	0.02156	$7 \cdot 10^{-5}$
3	0.02081	$7 \cdot 10^{-5}$
4	0.02396	$8 \cdot 10^{-5}$
5	0.02274	$7 \cdot 10^{-5}$
6	0.02174	$7 \cdot 10^{-5}$
7	0.02303	$7 \cdot 10^{-5}$
8	0.02379	$8 \cdot 10^{-5}$
9	0.02072	$7 \cdot 10^{-5}$
10	0.02289	$7 \cdot 10^{-5}$
11	0.02334	$8 \cdot 10^{-5}$
12	0.02129	$7 \cdot 10^{-5}$
13	0.02126	$7 \cdot 10^{-5}$
14	0.02328	$8 \cdot 10^{-5}$
15	0.02348	$8 \cdot 10^{-5}$
16	0.02141	$7 \cdot 10^{-5}$

(a) T1

Strip	F_{cal}[cGy/cts]	$\sigma_{F_{cal}}$[cGy/cts]
17	0.02286	$7 \cdot 10^{-5}$
18	0.02140	$7 \cdot 10^{-5}$
19	0.02148	$7 \cdot 10^{-5}$
20	0.02133	$7 \cdot 10^{-5}$
21	0.02293	$7 \cdot 10^{-5}$
22	0.02131	$7 \cdot 10^{-5}$
23	0.02130	$7 \cdot 10^{-5}$
24	0.02095	$7 \cdot 10^{-5}$
25	0.02364	$7 \cdot 10^{-5}$
26	0.02343	$7 \cdot 10^{-5}$
27	0.02296	$7 \cdot 10^{-5}$
28	0.02259	$7 \cdot 10^{-5}$
29	0.02330	$7 \cdot 10^{-5}$
30	0.02384	$7 \cdot 10^{-5}$
31	0.02275	$7 \cdot 10^{-5}$
32	0.02085	$7 \cdot 10^{-5}$

(b) T2

Strip	F_{cal}[cGy/cts]	$\sigma_{F_{cal}}$[cGy/cts]
33	0.01928	$6 \cdot 10^{-5}$
34	0.02074	$7 \cdot 10^{-5}$
35	0.02088	$7 \cdot 10^{-5}$
36	0.02060	$7 \cdot 10^{-5}$
37	0.02121	$7 \cdot 10^{-5}$
38	0.01935	$6 \cdot 10^{-5}$
39	0.01963	$6 \cdot 10^{-5}$
40	0.02074	$7 \cdot 10^{-5}$
41	0.01906	$6 \cdot 10^{-5}$
42	0.02095	$7 \cdot 10^{-5}$
43	0.01918	$6 \cdot 10^{-5}$
44	0.01971	$6 \cdot 10^{-5}$
45	0.02151	$7 \cdot 10^{-5}$
46	0.01928	$6 \cdot 10^{-5}$
47	0.01941	$6 \cdot 10^{-5}$
48	0.02068	$7 \cdot 10^{-5}$

(c) T3

Strip	F_{cal}[cGy/cts]	$\sigma_{F_{cal}}$[cGy/cts]
49	0.02111	$7 \cdot 10^{-5}$
50	0.01942	$6 \cdot 10^{-5}$
51	0.02117	$7 \cdot 10^{-5}$
52	0.02126	$7 \cdot 10^{-5}$
53	0.02106	$7 \cdot 10^{-5}$
54	0.01946	$6 \cdot 10^{-5}$
55	0.01941	$6 \cdot 10^{-5}$
56	0.01913	$6 \cdot 10^{-5}$
57	0.01931	$6 \cdot 10^{-5}$
58	0.01944	$6 \cdot 10^{-5}$
59	0.01927	$6 \cdot 10^{-5}$
60	0.01914	$6 \cdot 10^{-5}$
61	0.01965	$6 \cdot 10^{-5}$
62	0.01959	$6 \cdot 10^{-5}$
63	0.02152	$7 \cdot 10^{-5}$
64	0.02114	$7 \cdot 10^{-5}$

(d) T4

Table 4.9: Values of the calibration factor F_{cal} calculated in uniformity condition for each strip, and corresponding uncertainty.

where $\Delta y = |m|\Delta t$ as discussed in Sect. 4.1.1, and the effect of leakage current has been corrected for. The uncertainty on its value follows from the propagation of the uncertainty on Δy, calculated as in Sect. 4.1.6: $\sigma_{F_{cal}} = F_{cal} \cdot (\sigma_{\Delta y}/\Delta y)$.

Since five uniformity measurements have been taken, the final value for F_{cal} is the result of a weighted average on the values obtained from each measurement. It is reported for each strip in Table 4.9 and plotted in Fig. 4.10, where the difference in the response of the two detectors due to the shading effect can also be seen clearly.

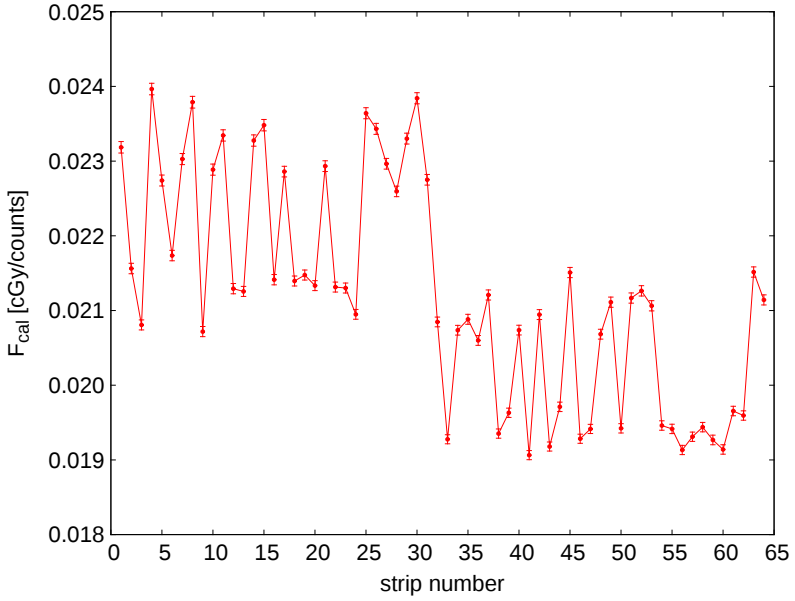

Figure 4.10: Plot of the calibration factors calculated for each strip in uniformity conditions: the values for strips 1 – 32, which belong to the lower detector, are on average higher than the ones of strips 33 – 64, which belong to the upper one ($F_{\mathrm{cal}} \propto (\Delta y_{\mathrm{unif}})^{-1}$). The error bars are also shown.

The absorbed dose is then calculated for each strip in each measurement as

$$D[\mathrm{cGy}] = F_{\mathrm{cal}} \cdot \Delta y = F_{\mathrm{cal}} \cdot |m| \Delta t \tag{4.8}$$

where the slope m has been corrected for leakage current. The uncertainty on this estimation is

$$\sigma_D = D \sqrt{\left(\frac{\sigma_{F_{\mathrm{cal}}}}{F_{\mathrm{cal}}}\right)^2 + \left(\frac{\sigma_m}{m}\right)^2 + \left(\frac{\sigma_{\Delta t}}{\Delta t}\right)^2} \tag{4.9}$$

where σ_m and $\sigma_{\Delta t}$ are calculated as in Sect. 4.1.6.

4.3.2 Calibration in standard conditions

In standard conditions (SSD = 100 cm, d = 1.5 cm, field size $10 \times 10\,\mathrm{cm}^2$) a fluence of 1 MU corresponds to a dose of 1 cGy at the centre of the beam. Another calibration procedure is therefore possible for the DSSSSD: the response of the four central strips (two in the upper and two in the lower detector) must be averaged in order to estimate the mean response at its centre, which is then proportional to the absorbed dose. However, the field in standard conditions cannot be considered flat (as shown by Fig. 4.9c): uniformity corrections have therefore to be applied to the response of each strip.

A set of seven measurements with 100 MU has been taken in standard conditions. The calibration procedure is in this case definitely more complex, and has been carried out according to the following steps:

1) For each measurement, the value of Δy for the four central strip (strip nr. 16, 17, 48, 49) has been calculated, along with its relative uncertainty. A weighted average

Strip	$(\mathbf{F}_{\mathrm{cal}})^{\mathrm{std}}$	$\sigma_{(\mathbf{F}_{\mathrm{cal}})^{\mathrm{std}}}$	Δ[std, unif]
1	0.02290	$9 \cdot 10^{-5}$	1.24%
2	0.02130	$8 \cdot 10^{-5}$	1.23%
3	0.02055	$8 \cdot 10^{-5}$	1.23%
4	0.02367	$9 \cdot 10^{-5}$	1.23%
5	0.02246	$9 \cdot 10^{-5}$	1.23%
6	0.02147	$8 \cdot 10^{-5}$	1.24%
7	0.02275	$9 \cdot 10^{-5}$	1.23%
8	0.02350	$9 \cdot 10^{-5}$	1.23%
9	0.02046	$8 \cdot 10^{-5}$	1.24%
10	0.02261	$9 \cdot 10^{-5}$	1.23%
11	0.02306	$9 \cdot 10^{-5}$	1.23%
12	0.02103	$8 \cdot 10^{-5}$	1.23%
13	0.02099	$8 \cdot 10^{-5}$	1.24%
14	0.02299	$9 \cdot 10^{-5}$	1.23%
15	0.02319	$9 \cdot 10^{-5}$	1.23%
16	0.02115	$8 \cdot 10^{-5}$	1.23%

(a) T1

Strip	$(\mathbf{F}_{\mathrm{cal}})^{\mathrm{std}}$	$\sigma_{(\mathbf{F}_{\mathrm{cal}})^{\mathrm{std}}}$	Δ[std, unif]
17	0.02258	$9 \cdot 10^{-5}$	1.23%
18	0.02113	$8 \cdot 10^{-5}$	1.23%
19	0.02121	$8 \cdot 10^{-5}$	1.23%
20	0.02107	$8 \cdot 10^{-5}$	1.23%
21	0.02265	$9 \cdot 10^{-5}$	1.23%
22	0.02105	$8 \cdot 10^{-5}$	1.23%
23	0.02104	$8 \cdot 10^{-5}$	1.23%
24	0.02069	$8 \cdot 10^{-5}$	1.23%
25	0.02335	$9 \cdot 10^{-5}$	1.23%
26	0.02314	$9 \cdot 10^{-5}$	1.23%
27	0.02268	$9 \cdot 10^{-5}$	1.23%
28	0.02232	$8 \cdot 10^{-5}$	1.23%
29	0.02302	$9 \cdot 10^{-5}$	1.23%
30	0.02355	$9 \cdot 10^{-5}$	1.24%
31	0.02247	$9 \cdot 10^{-5}$	1.23%
32	0.02059	$8 \cdot 10^{-5}$	1.23%

(b) T2

Strip	$(\mathbf{F}_{\mathrm{cal}})^{\mathrm{std}}$	$\sigma_{(\mathbf{F}_{\mathrm{cal}})^{\mathrm{std}}}$	Δ[std, unif]
33	0.01904	$7 \cdot 10^{-5}$	1.23%
34	0.02048	$8 \cdot 10^{-5}$	1.23%
35	0.02063	$8 \cdot 10^{-5}$	1.23%
36	0.02035	$8 \cdot 10^{-5}$	1.23%
37	0.02095	$8 \cdot 10^{-5}$	1.23%
38	0.01912	$7 \cdot 10^{-5}$	1.23%
39	0.01939	$7 \cdot 10^{-5}$	1.23%
40	0.02048	$8 \cdot 10^{-5}$	1.23%
41	0.01883	$7 \cdot 10^{-5}$	1.23%
42	0.02069	$8 \cdot 10^{-5}$	1.24%
43	0.01894	$7 \cdot 10^{-5}$	1.23%
44	0.01947	$8 \cdot 10^{-5}$	1.23%
45	0.02124	$8 \cdot 10^{-5}$	1.23%
46	0.01905	$7 \cdot 10^{-5}$	1.23%
47	0.01918	$7 \cdot 10^{-5}$	1.23%
48	0.02043	$8 \cdot 10^{-5}$	1.24%

(c) T3

Strip	$(\mathbf{F}_{\mathrm{cal}})^{\mathrm{std}}$	$\sigma_{(\mathbf{F}_{\mathrm{cal}})^{\mathrm{std}}}$	Δ[std, unif]
49	0.02085	$8 \cdot 10^{-5}$	1.23%
50	0.01918	$7 \cdot 10^{-5}$	1.23%
51	0.02091	$8 \cdot 10^{-5}$	1.23%
52	0.02100	$8 \cdot 10^{-5}$	1.23%
53	0.02080	$8 \cdot 10^{-5}$	1.23%
54	0.01922	$7 \cdot 10^{-5}$	1.24%
55	0.01918	$7 \cdot 10^{-5}$	1.23%
56	0.01890	$7 \cdot 10^{-5}$	1.23%
57	0.01907	$7 \cdot 10^{-5}$	1.23%
58	0.01920	$7 \cdot 10^{-5}$	1.23%
59	0.01903	$8 \cdot 10^{-5}$	1.24%
60	0.01890	$7 \cdot 10^{-5}$	1.23%
61	0.01941	$8 \cdot 10^{-5}$	1.23%
62	0.01935	$7 \cdot 10^{-5}$	1.23%
63	0.02125	$8 \cdot 10^{-5}$	1.23%
64	0.02088	$8 \cdot 10^{-5}$	1.23%

(d) T4

Table 4.10: Values of the calibration factor $(F_{\mathrm{cal}})^{\mathrm{std}}$ calculated in standard condition for each strip, corresponding uncertainty, and percent difference with the ones calculated in uniformity conditions.

of these values has then been calculated, in order to obtain the mean Δy^{std} for each of the central strips.

2) The four mean values of Δy^{std} have been corrected for uniformity by dividing by Δy^{unif}, and then averaged. The resulting factor $< F >$ is proportional to the relative difference in the response between standard and uniformity conditions.

3) The calibration factor has then been calculated for each strip i as

$$(F_{\mathrm{cal}})_i^{\mathrm{std}} = \frac{1}{(\Delta y^{\mathrm{unif}})_i} \frac{100\,\mathrm{cGy}}{< F >} \tag{4.10}$$

and its uncertainty follows from the propagation law:

$$\sigma_{(F_{\mathrm{cal}})^{\mathrm{std}}} = (F_{\mathrm{cal}})^{\mathrm{std}} \sqrt{\left(\frac{\sigma_{\Delta y^{\mathrm{unif}}}}{\Delta y^{\mathrm{unif}}}\right)^2 + \left(\frac{\sigma_{<F>}}{<F>}\right)^2}$$

where $\sigma_{<F>}$ is calculated as the uncertainty of the weighted average $< F >$.

The calibration factors calculated in this way are reported in Table 4.10, along with their uncertainty and percent difference with the ones calculated in uniformity conditions. It can be seen that this last parameter has a nearly constant value of 1.23%, with the calibration factors in uniformity conditions being higher than the corresponding ones in standard conditions. This effect could be due to the small difference in density between the solid water which is used to achieve the necessary DSSSSD depth and real liquid water used in quality assurance clinical measurements: the former is a little more dense, and therefore attenuates more the photon spectrum, producing the small discrepancy between the two calibration factors.

4.4 Comparison with clinical measurements

After its calibration, the DSSSSD has been used to reproduce routine QA hospital measurements, in order to analyse its response under different irradiation conditions and ensure its suitability for verifying all possible segments of a composite treatment plan. For this purpose, three different kinds of measurements have been carried out: Percent Depth Dose (PDD) ones, by varying the depth in solid water of the detector; penumbra ones, in order to estimate its width in both the inplane and crossplane directions; and Output Factor ones, with different field sizes. They are described in the following sections.

4.4.1 Percent depth dose curve

At a given source-to-surface distance and for a field of fixed size, the Percent Depth Dose is defined according to the following expression:

$$\mathrm{PDD}(d) = \frac{\mathrm{Dose}(d)}{\mathrm{Dose}(d_{\mathrm{ref}})} \cdot 100 \tag{4.11}$$

i.e., the percent ratio of the dose at a depth d to the one at a depth $d = d_{\mathrm{ref}}$, measured at the centre of the beam. The depth d_{ref} corresponds to the one at which the maximum of the curve is located: in the 6 MV photon mode, for a field size of $10 \times 10\,\mathrm{cm}^2$ and a SSD of 100 cm, $d_{\mathrm{ref}} = 1.5\,\mathrm{cm}$.

The depth dose has been measured with the DSSSSD at depths $d = 1.5$, 3.5, 5, 10 and 15 cm, by varying the amount of solid water placed above the slab phantom. The source-to-surface distance has been kept constant at 100 cm, and the field size at $10 \times 10\,\mathrm{cm}^2$. As for the calibration in standard conditions, a weighted average of the response of the strips 16, 17, 48 and 49 has been calculated in order to estimate the dose at the centre of the beam, which has then been normalized to the one measured at a depth $d_{\mathrm{ref}} = 1.5\,\mathrm{cm}$ according to the definition in Eq. (4.11).

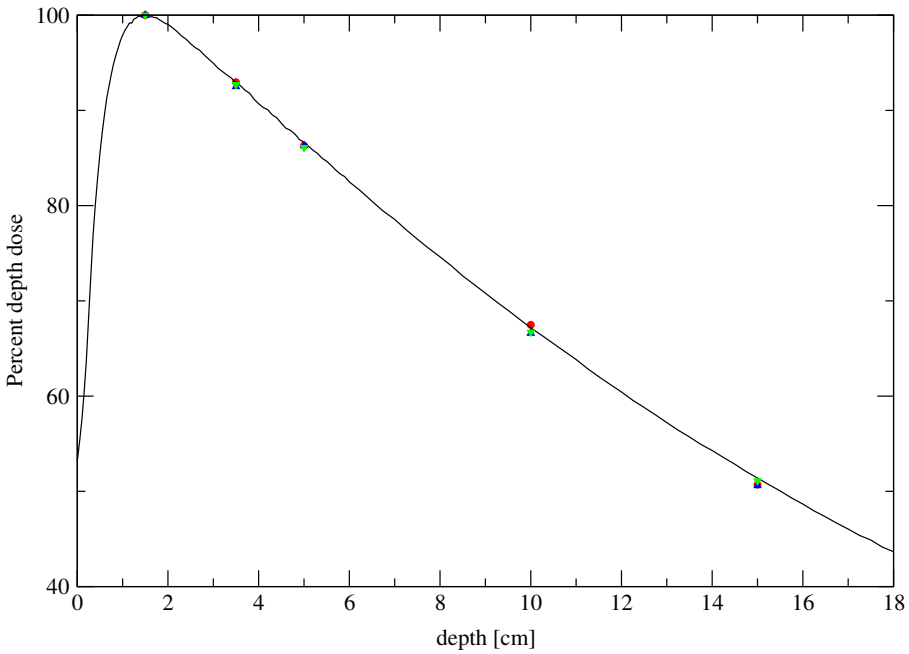

Figure 4.11: Percent depth dose measured by the DSSSSD (red circles) and calculated through GEANT4 simulations: dose in water (blue triangles), and dose-to-water measured by the simulated DSSSSD (green triangles), compared with data taken with a Farmer-type ionization chamber (black line). The size of the uncertainty bars is in all cases comparable to the size of the points.

Depth [cm]	DSSSSD exp.	G4 water	G4 DSSSSD	Ion chamber
1.5	100	100	100	100
3.5	93.0 ± 0.4	92.5 ± 0.4	92.7 ± 0.4	92.9
5	86.3 ± 0.4	86.3 ± 0.4	86.1 ± 0.4	86.7
10	67.5 ± 0.3	66.6 ± 0.3	66.7 ± 0.3	67.2
15	50.7 ± 0.3	50.6 ± 0.2	51.1 ± 0.2	51.4

Table 4.11: Percent depth dose measured by the DSSSSD and calculated through GEANT4 simulations: dose in water and dose measured by the simulated DSSSSD. Measurements taken with a Farmer-type ionization chamber are also shown for comparison.

As discussed in Sect. 4.2.2, the percent depth dose has also been calculated from GEANT4 simulations, in two different cases according to the materials used to model the constituent parts of the detector (sensitive volume, frame, etc.): (1) all volumes made out of water, and (2) using the actual material for each part. In order for these results to be comparable to experimental ones, a calibration factor was calculated for each strip i from the simulations in conditions of uniformity:

$$(F_{\mathrm{cal}})_i^{\mathrm{G4}} = \frac{81\,\mathrm{cGy}}{(\mathrm{Dose/hist})_i^{\mathrm{unif}}}$$

in an analogous way to what has been done for experimental data. The dose per history resulting for each strip in a given configuration has been calibrated by multiplying by this

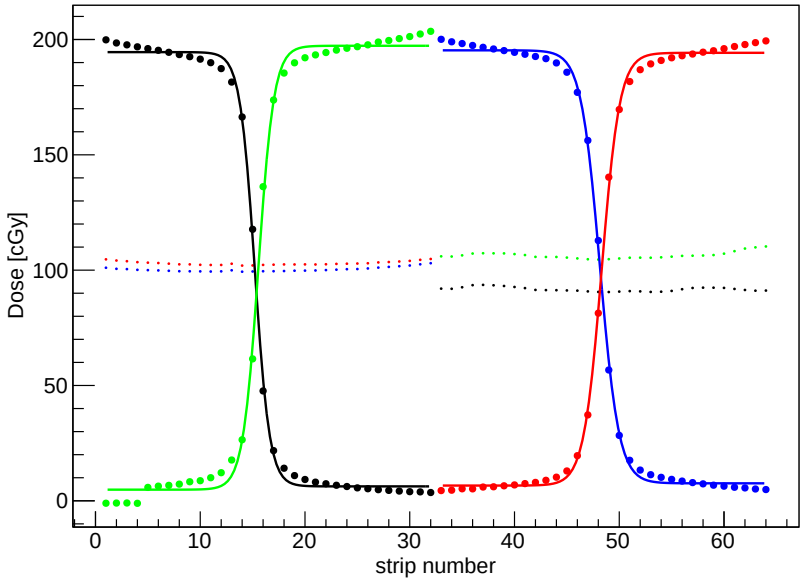

Figure 4.12: Penumbra profiles measured in the crossplane (left-right, strip 1 to 32) and inplane (up-down, strip 33 to 64) directions: left profile (black), right profile (green), up (red) and down (blue) ones. In each case, the data from the detector in which the penumbra profile is visible are plotted with filled circles, data from the other are shown as small dots of the same colour. The four continuous curves are a fit of the experimental data; the value of the uncertainty is comparable to the size of the points.

factor, and then the same procedure as in the case of experimental data has been used to calculated PDD values.

The resulting values are reported in Table 4.11, and plotted in Fig. 4.11. Hospital QA data taken with a Farmer-type ionization chamber are also reported for comparison: in all three cases an agreement below 1% can be seen. The only exception are the values at a depth of 15 cm, for which the agreement is worse (1.5%): this is probably due to the fact that these data are the ones in which the absorbed dose is lowest, and therefore more affected by uncertainties on the normalization point.

4.4.2 Penumbra

For a field of a given size, at a given solid water depth and source-to-surface distance, the penumbra region is defined as the distance between the 80% and 20% dose levels, being the reference dose the one measured at the central axis of the beam. To measure its width, asymmetric fields of $5 \times 10\,\mathrm{cm}^2$ have been used, which covered only the left or right half of each detector.

Four different acquisitions were carried out, two with the short size of the rectangle parallel to the x direction, and two parallel to the y one. In each of them, the geometrical projection of the radiation field on the detector plane completely covers only the strips belonging to one of the four boards of the ADC. The strips with the same orientation as the rectangular field (parallel to its 10 cm-side) measured therefore either a high or a very

Position	a [cGy]	b [cGy]	c $[(\text{str n})^{-1}]$	d [str n]	Δx_{pen}[mm]
L	6.25	194.5	1.41391	15.2	3.9
R	197.3	4.83	1.34358	15.5	4.1
LR	-12.41	171.2	-1.59753	2.9	3.5
			-1.6392	27.9	3.4
U	194.2	6.61	1.16653	48.3	4.8
D	7.58	195.3	1.10621	48.2	5.0
UD	-11.94	166.6	-1.32149	35.7	4.2
			-1.24484	60.8	4.5

Table 4.12: Parameters of the fits to the sigmoidal and double-sigmoidal curves; estimation of the width of the penumbra based on Eq. (4.13). The final estimation of the penumbra reported in the text is the average of the first two rows of each group.

small amount of dose, depending on whether they are illuminated by the radiation field or not, while those of the other detector, which are only half-covered, measure an amount of dose which should be half of the maximum value, if the detector is correctly centered in the geometrical centre of the beam.

These acquisitions have been labelled according to the position of the radiation field with respect of the treatment couch, as if the detector was a patient lying down on it and looking towards the accelerator: "up" (U) and "down" (D) along the y direction (defined by the longitudinal axis of the treatment couch; "up" corresponds to the side closer to the gantry), and "left" (L) and "right" (R) along the x one (defined by the transversal one). Since neither the gantry nor the accelerator head have been rotated, the x direction corresponds to crossplane, y to inplane. The fully irradiated strips are the ones belonging to T1 in the position L, to T2 in R, to T4 in U and to T3 in D. The irradiation conditions were SSD = 100 cm, $d = 1.5$ cm, asymmetric field of 5×10 or $10 \times 5\,\text{cm}^2$.

The spectra resulting from these acquisitions are plotted in Fig. 4.12, where the strips whose orientation is parallel to the radiation field are shown with filled circles, the others with small dots[1]. A continuous curve is also shown, which is a fit to the data of a sigmoidal function of the form

$$f(x) = a + \frac{b-a}{1+e^{c(x-d)}} \tag{4.12}$$

The parameters a and b are the upper and lower asymptotes, d is the inflection point of the curve (which corresponds to 50% of the variation in y) and c is related to the slope at the flex.

The width of the penumbra can be calculated from Eq. (4.12) as $\Delta x_{\text{pen}} = |x_1 - x_2|$, where $f(x_1) = 0.8(b-a)+a$ and $f(x_2) = 0.2(b-a)+a$. After inverting the equation and subtracting the two resulting values, the following expression is obtained:

$$\Delta x_{\text{pen}} = \frac{2}{c}\ln 4 \tag{4.13}$$

[1]The analysis of the response of the strips that are only half-irradiated is a good means to check if the detector is correctly centered at the centre of the beam: if it is, the amount of measured dose should not change when the irradiation position is changed from left to right (or up to down). In Fig. 4.12, it can be seen that the DSSSSD is correctly centered along the y direction, but a small error has been committed along the x one.

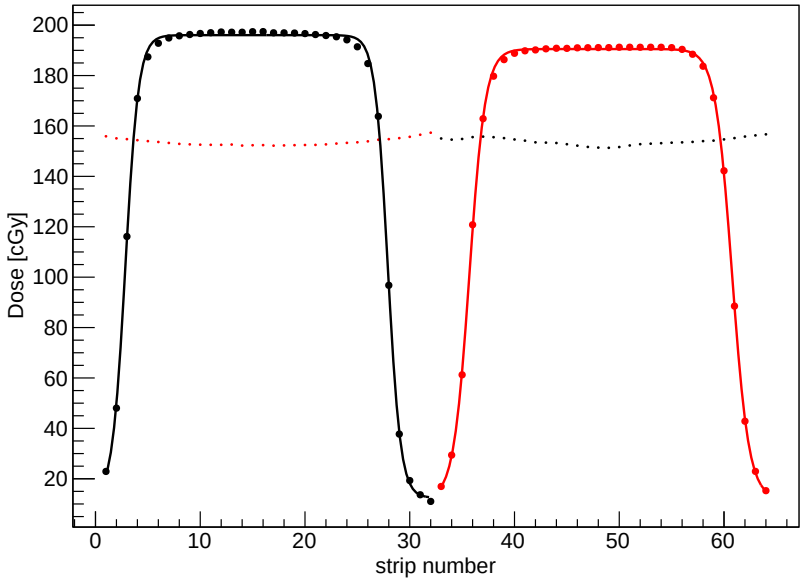

Figure 4.13: Centered penumbra profiles measured in the crossplane (black) and inplane (red) directions. As in Fig. 4.12, data from the detector in which the profile is visible are plotted with filled circles, data from the other are shown as small dots. The continuous curves are a fit of the data to a double sigmoidal function; the uncertainty on the dose is comparable to the size of the points.

This result has to be multiplied by the strip width (2 mm) in order to express it in millimeters. For each of the four acquisition just described, it is reported in Table 4.12 along with the set of parameter values resulting from the fit.

Two more acquisition have been carried out in order to analyse field profiles and estimate the width of the penumbra region: in these, the asymmetric field measuring $5 \times 10\,\mathrm{cm}^2$ or $10 \times 5\,\mathrm{cm}^2$ was centered on the active area, both along the x and y directions. The resulting spectra have been fitted to a double sigmoidal curve of the form

$$g(x) = a + (a + b)\left(\frac{1}{1 + e^{c_1(x-d_1)}} - \frac{1}{1 + e^{c_2(x-d_2)}}\right) \tag{4.14}$$

and are plotted in Fig. 4.13. From this function, two estimations of the width of the penumbra can be obtained in an analogous way to the previous case. However, the resulting values are lower than the ones obtained from non-centered fields: this discrepancy is probably due to a lack of data points in the low-dose region for the centered spectra.

The final estimation of the width of the penumbra region is therefore (4 ± 1) mm in the crossplane direction, and (5 ± 1) mm in the inplane one. The resolution is given by half of the strip pitch. These results are consistent with what can be inferred from the analysis of the geometry of the accelerator head: the crossplane direction corresponds to the direction of motion of the leaves of the Multi-Leaf Collimator, while the inplane one to the one of the collimator jaws, which are located closer to the source. The field variation is therefore less sharp in the crossplane direction.

Field size [cm]	DSSSSD 1.5 cm	DSSSSD 10 cm	ion chamber 10 cm	Diff.
1	0.744 ± 0.009	0.635 ± 0.012	0.652	2.6%
2	0.867 ± 0.007	0.813 ± 0.009	0.782	3.9%
5	0.935 ± 0.004	0.868 ± 0.005	0.885	1.9%
8	0.987 ± 0.004	0.963 ± 0.004	0.965	0.2%
10	1	1	1	—
15	1.037 ± 0.004	1.080 ± 0.005	1.065	1.4%
20	1.068 ± 0.004	1.115 ± 0.005	1.120	0.4%

Table 4.13: Results of output factor measurements taken with the DSSSSD at $d = 1.5\,\text{cm}$ and $d = 10\,\text{cm}$, with corresponding uncertainty. Measurements taken with an ionization chamber for QA purposes are also shown for comparison.

4.4.3 Output Factor measurements

The Output Factor is defined as the ratio of the dose deposited in the centre of the beam by a field of an arbitrary size to the one deposited by the $10 \times 10\,\text{cm}^2$ reference field, at a given source-to-surface distance and depth in water:

$$OF(A \times A) = \frac{\text{Dose}\,(A \times A)}{\text{Dose}\,(10 \times 10\,\text{cm}^2)} \tag{4.15}$$

It is an intrinsic parameter of the accelerator and is kept monitored for QA purposes. Since in order to obtain a reliable Output Factor measurement the dosimeter has to be small compared to the field size under analysis [66], high-precision ionization chambers or silicon diodes are employed.

It has been measured with the DSSSSD at two different depths of solid water: $d = 10\,\text{cm}$, which is the one which is considered for hospital QA measurements, and at $d = 1.5\,\text{cm}$. In both cases the source-to-surface distance was kept constant at 100 cm. The field sizes that have been considered are $1 \times 1\,\text{cm}^2$, $2 \times 2\,\text{cm}^2$, $5 \times 5\,\text{cm}^2$, $8 \times 8\,\text{cm}^2$, the reference $10 \times 10\,\text{cm}^2$, $15 \times 15\,\text{cm}^2$ and $20 \times 20\,\text{cm}^2$.

As for percent depth dose measurements, the dose response of the four central strips has been averaged in order to estimate the dose at the centre of the beam. The dose values for the $10 \times 10\,\text{cm}^2$ reference field and for the smallest $1 \times 1\,\text{cm}^2$ one are calculated from the average of two measurement, in order to provide higher precision. The Output Factor has then been calculated for each measurement according to Eq. (4.15). For the field sizes that are smaller than the active area of the detector ($6.4 \times 6.4\,\text{cm}^2$), a correction factor $6.4/A$ has been introduced to take into account the fact that the radiation field does not cover completely the active area of the strips (A is the size of the square field).

The resulting values are reported in Table 4.13 and plotted in Fig. 4.14. The difference with hospital values is significant in some cases (up to 4σ); this can be understood by considering the fact that the strip length is not negligible if compared to the field size, therefore, a significant amount of off-axis dose is measured and the Output Factor estimation is not completely reliable. However, the aim of these measurements is not to measure the Output Factor for itself, but to validate the detector calibration for different field sizes; these result can therefore be accepted since the percent difference is lower than 2% for all fields but the smallest ones. For field sizes below $2 \times 2\,\text{cm}^2$, the agreement is less reliable.

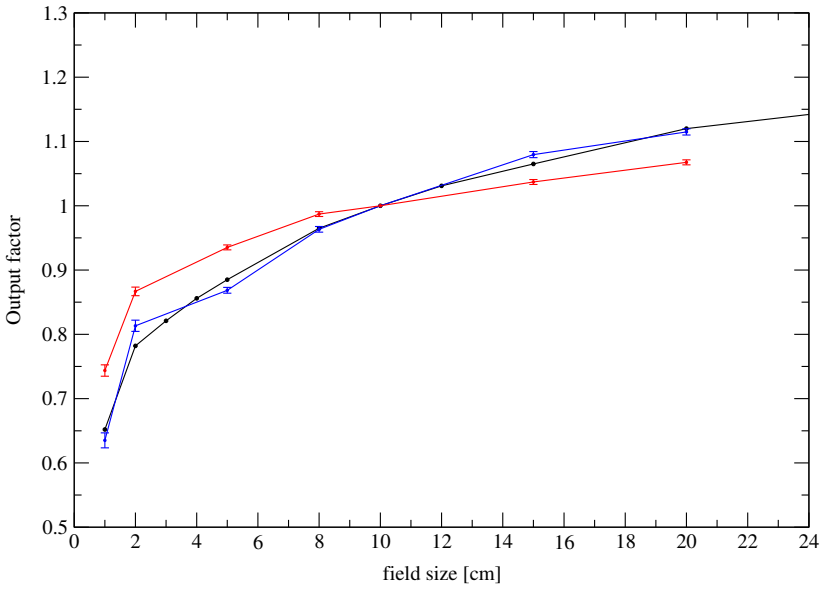

Figure 4.14: Output factor measured by the DSSSSD at $d = 1.5\,\text{cm}$ (red) and $d = 10\,\text{cm}$ (blue); hospital QA measurements taken with an ionization chamber at $d = 10\,\text{cm}$ (black). In the three cases the SSD is 100 cm.

This could be due to an imperfect centering of the detector, which affects in a stronger way measurements with small field sizes.

Chapter 5

Conclusions and future perspectives

Following a critical review of the results obtained in a first feasibility study performed with a commercial single-sided silicon strip detector, a new detection system for the verification of complex radiotherapy treatments has been designed and built in the framework of the RADIA collaboration. The new detector is composed by two single-sided silicon detectors, mounted on the same Kapton frame in a back-to-back configuration, and separated by a layer made of Kapton as well. Compared to the first prototype, the new one has more strips, a smaller strip pitch, a bigger active area, and an improved water-equivalence of the surrounding materials.

The aim of this work has been the first characterization of the detection system placed in the slab phantom, orthogonally to the beam axis. In particular, its response has been firstly analysed in terms of linearity, reproducibility, dose threshold and amount of leakage current:

- Linearity has been found to be very good ($r^2 - 1 \simeq 10^{-5}$) even if the presence of a second order term in the transfer function is visible in the residuals plots of the linear fits. However, it has been shown that the linear and quadratic model lead to an identical estimation of the absorbed dose, therefore, the analysis has been carried out with a linear model.

- Reproducibility over a three-month time period is on average within 1%, and lower than 2% for all strips.

- Due to the saturation of the T1, T3 and T4 boards of the ADC, the minimum dose threshold which ensures a reliable response has been found to be (9.4±0.2) cGy. However, the strips belonging to the unsaturated board (T2) provide a reliable response even at a dose of 1.7 cGy. It has therefore been decided to modify the electronic chain in order for all the strips to be unsaturated.

- The overestimation in the absorbed dose due to leakage current has been quantified in 0.02 cGy/s for all strips but strip 13, and corrected for. For strip 13, the overestimation is 0.16 cGy/s.

The detection system has also been simulated by means of the GEANT4 toolkit. As expected, this analysis has provided valuable insight on the influence of the different materials on the response of each of the two detecting layers of the DSSSSD. In particular,

the 'shading effect' of the upper silicon layer on the lower one has been put in evidence, justifying the single reading given for the two detectors. The water-equivalence of Kapton scattering properties with respect to water has also been assessed.

The calibration has been carried out both in standard and in uniformity conditions[1], in order to ensure its reliability. A difference of 1.2% has been found between the two cases, which has been attributed to the small difference in density between solid water which has been used to achieve the necessary DSSSSD depth and real liquid water used for clinical quality assurance.

For what concerns the comparison with hospital measurements, good agreement has been found in all cases. Percent Depth Dose measurements agree within 1% with both hospital measurements and GEANT4 simulations, confirming the validity of the calibration for different solid water depths. The only exception is the case of $d = 15\,\mathrm{cm}$, for which a difference of 1.6% has been found. This is probably due to the fact that these data are more affected by uncertainties in the normalization point, being the furthest away from it. The estimation of the width of the penumbra region in both the inplane and crossplane directions is compatible with hospital measurements. Even if the DSSSSD is not designed to perform Output Factor measurements, an agreement below 2% was found for field sizes of $5 \times 5\,\mathrm{cm}^2$ or bigger: this confirms the validity of the calibration for different field sizes.

Future perspectives

In order to improve the performance of the DSSSSD, the electronic chain is currently being modified so that the voltage reference value will be lower than 5 V for all strips. This will lead to a dose threshold comparable to the one measured with T2 (1.7 cGy) for the other strips as well. The measurement of leakage current in all boards will then be possible. A new analysis of the noise amplitude will also be needed. Finally, the standard deviation of repeated measurements should be monitored in different conditions, in order to obtain a better estimation of uncertainties in all cases.

The characterization of the DSSSSD with the plane phantom in the coronal plane is the first necessary step in order to understand the behaviour of the new dosimetry system. The detector will then be placed in the cylindrical phantom in order to study its angular response in the axial plane. The equivalence of phantom rotation of an angle θ and gantry rotation of an angle $-\theta$ will be experimentally studied, and new calibration factors will be obtained by comparison with TPS dose calculations.

The final benchmark for this novel technique will be the reconstruction of a dose map in the axial plane. In order to do so, a reconstruction algorithm based on the Radon transform formalism was developed for the first detecting prototype, and is currently being adapted to the DSSSSD [14]. The Radon transform of a function $D(x, y)$, which in this case can be identified with the absorbed dose, is defined in a frame of reference (x', y') which is rotated of an angle θ with respect to (x, y), and corresponds to the line integral of $D(x', y', \theta)$ over y', at $x' = \mathrm{cost}$.

The analogy with the DSSSSD is clear: the response of each strip corresponds to the line integral over the strip direction of the dose measured in the rotated frame. At a fixed

[1] *Standard conditions*: source-to-surface distance 100 cm, depth in water 1.5 cm, field size $10 \times 10\,\mathrm{cm}^2$. *Uniformity conditions*: source-to-surface distance 90 cm, depth in water 10 cm, field size $10 \times 10\,\mathrm{cm}^2$.

phantom rotation angle $\overline{\theta}$, each acquisition provides the function $D(x', \overline{\theta})$, and by repeating the measurements for different angles, the complete function $D(x', \theta)$ can be obtained. The function $D(x, y)$ can then in principle be calculated by inverting the Radon transform. In practice, this is done by using the projection-slice theorem, which states the equivalence of the Fourier transforms of the two functions $D(x, y)$ and $D(x', \theta)$. Since the DSSSSD is composed of discrete elements, the formalism has to be discretized, and the final dose map is reconstructed in 1024 pixels with area $2 \times 2\,\mathrm{mm}^2$ each. A background suppression filter and other frequency filtering are applied in order to improve the dose map quality.

Compared to the first prototype, the DSSSSD offers the opportunity to obtain two orthogonal angular measurements with a single data acquisition. Moreover, the smaller strip pitch provides a higher resolution, and the bigger active area permits the reconstruction of larger dose maps. The new prototype is therefore expected to be both faster and more precise than the previous one in the verification of an entire treatment plan.

Moreover, in order to reduce the time needed for data analysis and provide online dose reconstruction, a human machine interface is currently being developed by including in the data acquisition software routines for calibration, dose reconstruction and comparison with TPS data or other sets of measurements [67]. In this way, the complete verification process of an IMRT treatment could be done online in a simple and comprehensive way, reducing the incidence of relevant TPS errors and permitting to fully exploit the benefits of IMRT.

Bibliography

[1] Isselbacher K.J., Braunwald E., Wilson J.D., Martin J.B., Fauci A.S., Kasper D.L., ed., *Principles of Internal Medicine*, vol. 2, McGraw-Hill (1994)

[2] Gunderson L.L., Tepper J.E., ed., *Clinical Radiation Oncology*, Saunders, Elsevier (2012)

[3] Ezzell G.A., Galvin J.M., Low D., Palta J.R., Rosen I., Sharpe M.B., Xia P., Xiao Y., Xing L., Yu C.X., *Guidance document on delivery, treatment planning, and clinical implementation of IMRT: Report of the IMRT subcommittee of the AAPM radiation therapy committee*, Medical Physics 30(8), 2089 (2003)

[4] IARC website, http://www.iarc.fr/index.php

[5] Wilson R.R., *Radiological use of fast protons*, Radiology 47, 487 (1946)

[6] Chu W.T.T., *Overview of light-ion beam therapy*, in *Dose Reporting in Ion Beam Therapy* IAEATECDOC-1560, IAEA (2007)

[7] Amaldi U., Kraft G., *European developments in radiotherapy with beams of large radiobiological effectiveness*, Journal of Radiation Research 48(Suppl. A), A27 (2007)

[8] Schardt D., Elsässer T., Schulz-Ertner D., *Heavy-ion tumor therapy: Physical and radiobiological benefits*, Reviews of Modern Physics 82, 383 (2010)

[9] Podgorsak E.B., ed., *Radiation Oncology Physics: A Handbook for Teachers and Students*, IAEA (2005). Available online at http://www-pub.iaea.org/books/IAEABooks/7086/Radiation-Oncology-Physics-A-Handbook-for-Teachers-and-Students

[10] Turala M., *Silicon tracking detectors – historical overview*, Nuclear Instruments and Methods in Physics Research A 541, 1 (2005)

[11] Amendolia S.R., et al., *A multi-electrode silicon detector for high energy experiments*, Nuclear Instruments and Methods 176, 457 (1980)

[12] Shapiro S.L., Dunwoodie W.M., Arens J.F., Garrett Jernigan J., Gaalema S., *Silicon pin diode array hybrids for charged particle detection*, Nuclear Instruments and Methods in Physics Research A 275, 580 (1989)

[13] Bocci A., Cortés-Giraldo M.A, Gallardo M.I., Espino J.M., Arráns R., Alvarez M.A.G., Abou-Haïdar Z., Quesada J.M., Pérez Vega-Leal A., Pérez Nieto F.J., *Silicon strip detector for a novel 2D dosimetric method for radiotherapy treatment verification*, Nuclear Instruments and Methods in Physics Research A 673, 98 (2012)

[14] Patent Number ES 2409760 B1 (13/09/2011) at the OEMP – Oficina Española de Patentes y Marcas – Ministry of Industry & Commerce

[15] Alvarez M.A.G., Abou-Haïdar Z., Arráns R., Battaglia M.C., Cortés-Giraldo M.A., Espino J.M., Gallardo M.I., Ovejero M.C., Pérez Vega-Leal A., Selva A., Walsch S., *Novel dual single sided silicon strip detector chip for radiotherapy verification*, in X Latin American Symposium on Nuclear Physics and Application (X LASNPA), 1-6 December 2013, Montevideo, Uruguay (to be published in Proceedings of Science)

[16] Cortés-Giraldo M.A., Gallardo M.I., Arráns R., Quesada J.M., Bocci A., Espino J.M., Abou-Haïdar Z., Alvarez M.A.G., GEANT4 *simulation to study the sensitivity of a MICRON Silicon Strip Detector irradiated by a SIEMENS PRIMUS Linac*, Progress in Nuclear Science and Technology 2, 191 (2011)

[17] Cortés-Giraldo M.A., *Desarrollos y aplicaciones de* GEANT4 *para radioterapia y microdosimetría en detectores y circuitos integrados*, Ph.D. thesis, University of Seville (2011).

[18] Agostinelli S., et al., GEANT4 – *a simulation toolkit*, Nuclear Instruments and Methods in Physics Research A 506, 250 (2003)

[19] Allison J. et al., GEANT4 *developments and applications*, IEEE – Transactions on Nuclear Science 53(1), 270 (2006)

[20] Apostolakis J., et al., *Geometry and physics of the* GEANT4 *toolkit for high and medium energy applications*, Radiation Physics and Chemistry 78, 859 (2009)

[21] Ivanchenko V., et al., *Recent Improvements in* GEANT4 *Electromagnetic Physics Models and Interfaces*, Progress in Nuclear Science and Technology 2, 898 (2011)

[22] Cirrone G.A.P., Cuttone G., Di Rosa F., Pandola L., Romano F., Zhang Q., *Validation of the* GEANT4 *electromagnetic photon cross-sections for elements and compounds*, Nuclear Instruments and Methods in Physics Research A 618, 315 (2010)

[23] Amako K., et al., GEANT4 *and its validation*, Nuclear Physics B – Proceedings Supplements 150, 44 (2006)

[24] http://geant4-dna.org/

[25] Incerti S., et al., *Comparison of* GEANT4 *very low energy cross section models with experimental data in water*, Medical Physics 37(9), 4692 (2010)

[26] http://geant4.web.cern.ch/geant4/UserDocumentation/UsersGuides/ForApplicationDeveloper/html/in

[27] Johns H.E., Cunningham J.R., *The Physics of Radiology*, Charles C. Thomas Publisher Ltd. (1983)

[28] Knoll G.F., *Radiation detection and measurements*, John Wiley & Sons, (2000)

[29] Attix F.H., *Introduction to radiological physics and radiation dosimetry*, Wiley-Interscience Publications, John Wiley & Sons (1986)

[30] Shi J., Simon W.E., Zhu T.C. *Modeling the instantaneous dose rate dependence of radiation diode detectors*, Medical Physics 30(9), 2509 (2003)

[31] Nelms B.E., Zhen H., Tomé W.A., *Per-beam, planar IMRT QA passing rates do not predict clinically relevant patient dose errors*, Medical Physics 38(2) (2011)

[32] Bucciolini M., Banci Buonamici F., Casati M., *Verification of IMRT fields by film dosimetry*, Medical Physics 31(1), 161 (2004)

[33] Banci Buonamici F., Compagnucci A., Marrazzo L., Russo S., Bucciolini M., *An intercomparison between film dosimetry and diode matrix for IMRT quality assurance*, Medical Physics 34(4), 1372 (2007)

[34] Ansbacher W., *Three-dimensional portal image-based dose reconstruction in a virtual phantom for rapid evaluation of IMRT plans*, Medical Physics 33(9), 3369 (2006)

[35] McNutt T.R., Mackie T.R., Reckwerdt P., Paliwal B.R., *Modeling dose distributions from portal dose images using the convolution/superposition method*, Medical Physics 23(8), 1381 (1996)

[36] Antonuk L.E., *Electronic portal imaging devices: a review and historical perspective of contemporary technologies and research*, Physics in Medicine and Biology 47, R31 (2002)

[37] van Elmpt W., McDermottb L., Nijstena S., Wendling M., Lambina P., Mijnheer B., *A literature review of electronic portal imaging for radiotherapy dosimetry*, Radiotherapy and Oncology 88, 289 (2008)

[38] http://www.sunnuclear.com/medPhys/patientqa/mapcheck2/mapcheck2.asp

[39] http://www.iba-dosimetry.com/sites/default/files/RT-BR-E-I%E2%80%99mRT-MatriXX_Rev.2_0813_5.pdf

[40] http://www.ptw.de/1982.html?&cId=6620

[41] Jursinic P.A., Nelms B.E., *A 2-D diode array and analysis software for verification of intensity modulated radiation therapy delivery*, Medical Physics 30(5), 870 (2003)

[42] Li J.G., Yan G., Liu C., *Comparison of two commercial detector arrays for IMRT quality assurance*, Journal of Applied Clinical Medical Physics 10(2), 62 (2009)

[43] Saminathan S., Manickam R., Chandraraj V., Supe S., *Dosimetric study of 2D ion chamber array matrix for the modern radiotherapy treatment verification*, Journal of Applied Clinical Medical Physics 11(2), 116 (2010)

[44] Amerio S., et al., *Dosimetric characterization of a large-area pixel-segmented ionization chamber*, Medical Physics 31(2), 414 (2004)

[45] Poppe B., Blechschmidt A., Djouguela A., Kollhoff R., Rubach A., Willborn K.C., Harder D., *Two-dimensional ionization chamber arrays for IMRT plan verification*, Medical Physics 33(4), 1005 (2006)

[46] Spezi E., Angelini A.L., Romani F., Ferri A. *Characterization of a 2D ion chamber array for the verification of radiotherapy treatments*, Physics in Medicine and Biology 50(14), 3361 (2005)

[47] Griessbach I., Lapp M., Bohsung J., Gademann G., Harder D., *Dosimetric characteristics of a new unshielded silicon diode and its application in clinical photon and electron beams*, Medical Physics 32(12), 3750 (2005)

[48] Menichelli D., et al., *Design and development of a silicon-segmented detector for 2D dose measurements in radiotherapy*, Nuclear Instruments and Methods in Physics Research A 583, 109 (2007)

[49] Talamonti C., Bruzzi M., Marrazzo L., Menichelli D., Scaringella M., Bucciolini M., *Bidimensional silicon dosimeter: Development and characterization* Nuclear Instruments and Methods in Physics Research A 658, 84 (2011)

[50] Talamonti C., Bruzzi M., Bucciolini M., Marrazzo L., Menichelli D., *Preliminary dosimetric characterization of a silicon segmented detector for 2D dose verifications in radiotherapy*, Nuclear Instruments and Methods in Physics Research A 583, 114 (2007)

[51] Manolopoulos S., Wojnecki C., Hugtenburg R., Jaafar Sidek M.A., Chalmers G., Heyes G., Green S., *Small field measurements with a novel silicon position sensitive diode array*, Physics in Medicine and Biology 54, 485 (2009)

[52] Wong J.H.D., Carolan M., Lerch M.L.F., Petasecca M., Khanna S., Perevertaylo V.L., Metcalfe P., Rosenfeld A.B., *A silicon strip detector dose magnifying glass for IMRT dosimetry*, Medical Physics 37(2), 427 (2010)

[53] http://www.sunnuclear.com/medPhys/patientqa/arccheck/arccheck.asp

[54] http://scandidos.com/upload/Documents/Brochures/Scandidos_Delta4PT%20True%20volumetric.pdf

[55] http://www.ptw.de/2403.html

[56] Sadagopan R., Bencomo J.A., Martin R.L., Nilsson G., Matzen T., Balter P.A., *Characterization and clinical evaluation of a novel IMRT quality assurance system*, Journal of Applied Clinical Medical Physics 10, 104 (2009)

[57] Lin M.H., Koren S., Veltchev I., Li J., Wang L., Price R.A., and Ma C.M., *Measurement comparison and Monte Carlo analysis for volumetric-modulated arc therapy (VMAT) delivery verification using the ArcCHECK dosimetry system*, Journal of Applied Clinical Medical Physics 14(4), (2013)

[58] Stathakis S., Myers P., Esquivel C., Mavroidis P., Papanikolaou N., *Characterization of a novel 2D array dosimeter for patient-specific quality assurance with volumetric arc therapy*, Medical Physics 40(7), 071731 (2013)

[59] Bedford J.L., Lee Y.K., Wai P., South C.P., Warrington A.P., *Evaluation of the Delta^4 phantom for IMRT and VMAT verification*, Physics in Medicine and Biology 54(9), N167 (2009)

[60] Feygelman V., Zhang G., Stevens C., Nelms B.E., *Evaluation of a new VMAT QA device, or the "X" and "O" array geometries*, Journal of Applied Clinical Medical Physics 12(2), 3346 (2011)

[61] Cortés-Giraldo M.A., Quesada J.M., Gallardo M.I., GEANT4 *application for the simulation of the head of a Siemens Primus linac*, AIP Conference Proceedings 1231(1), 209 (2010)

[62] https://www-nds.iaea.org/phsp/phsp.htmlx

[63] Cortés-Giraldo M.A., Quesada J.M., Gallardo M.I., Capote R., *An implementation to read and write IAEA phase-space files in* GEANT4*-based simulations*, International Journal of Radiation Biology 88(1-2), 200 (2012)

[64] https://www-nds.iaea.org/phsp/Geant4/

[65] http://root.cern.ch/

[66] Sauer O.A., Wilbert J., *Measurement of output factors for small photon beams*, Medical Physics 34(6), 1983 (2007)

[67] Ovejero Mayoral M.C., *Sistema de Verificación de Tratamientos Complejos de Radioterapia*, Ph.D. thesis, University of Seville (in preparation).